UNIVERSIDAD DE INVESTIGACIÓN DE TECNOLOGÍA EXPERIMENTAL YACHAY

Escuela de Ciencias Físicas y Nanotecnología

TÍTULO: *Ab initio* **study of the structural and electronic properties of Niobium Sulfide (NbS$_2$) and Lithium Niobium Sulfide (LiNbS$_2$) bulk and (001) surfaces**

Trabajo de integración curricular presentado como requisito para la obtención del título de Físico

Autor:

Vega Bazantes Jorge David

Tutor:

Ph. D. Pinto Esparza Henry Paúl

Urcuquí, Octubre 2020

SECRETARÍA GENERAL
(Vicerrectorado Académico/Cancillería)
ESCUELA DE CIENCIAS FÍSICAS Y NANOTECNOLOGÍA
CARRERA DE FÍSICA
ACTA DE DEFENSA No. UITEY-PHY-2020-00016-AD

A los 6 días del mes de noviembre de 2020, a las 09:00 horas, de manera virtual mediante videoconferencia, y ante el Tribunal Calificador, integrado por los docentes:

Presidente Tribunal de Defensa	Dr. VACACELA GOMEZ, CRISTIAN ISAAC , Ph.D.
Miembro No Tutor	Dra. PERALTA ARCIA, MAYRA ALEJANDRA DE JESUS , Ph.D.
Tutor	Dr. PINTO ESPARZA, HENRY PAUL , Ph.D.

El(la) señor(ita) estudiante **VEGA BAZANTES, JORGE DAVID**, con cédula de identidad No. **1004139653**, de la **ESCUELA DE CIENCIAS FÍSICAS Y NANOTECNOLOGÍA**, de la Carrera de **FÍSICA**, aprobada por el Consejo de Educación Superior (CES), mediante Resolución **RPC-SO-39-No.456-2014**, realiza a través de videoconferencia, la sustentación de su trabajo de titulación denominado: **AB INITIO STUDY OF THE STRUCTURAL AND ELECTRONIC PROPERTIES OF NIOBIUM SULFIDE (NbS2) AND LITHIUM NIOBIUM SULFIDE (LiNbS2) BULK AND (001) SURFACES**, previa a la obtención del título de **FÍSICO/A**.

El citado trabajo de titulación, fue debidamente aprobado por el(los) docente(s):

Tutor	Dr. PINTO ESPARZA, HENRY PAUL , Ph.D.

Y recibió las observaciones de los otros miembros del Tribunal Calificador, las mismas que han sido incorporadas por el(la) estudiante.

Previamente cumplidos los requisitos legales y reglamentarios, el trabajo de titulación fue sustentado por el(la) estudiante y examinado por los miembros del Tribunal Calificador. Escuchada la sustentación del trabajo de titulación a través de videoconferencia, que integró la exposición de el(la) estudiante sobre el contenido de la misma y las preguntas formuladas por los miembros del Tribunal, se califica la sustentación del trabajo de titulación con las siguientes calificaciones:

Tipo	Docente	Calificación
Tutor	Dr. PINTO ESPARZA, HENRY PAUL , Ph.D.	10,0
Miembro Tribunal De Defensa	Dra. PERALTA ARCIA, MAYRA ALEJANDRA DE JESUS , Ph.D.	10,0
Presidente Tribunal De Defensa	Dr. VACACELA GOMEZ, CRISTIAN ISAAC , Ph.D.	10,0

Lo que da un promedio de: **10 (Diez punto Cero)**, sobre 10 (diez), equivalente a: **APROBADO**

Para constancia de lo actuado, firman los miembros del Tribunal Calificador, el/la estudiante y el/la secretario ad-hoc.

Certifico que *en cumplimiento del Decreto Ejecutivo 1017 de 16 de marzo de 2020, la defensa de trabajo de titulación (o examen de grado modalidad teórico práctica) se realizó vía virtual, por lo que las firmas de los miembros del Tribunal de Defensa de Grado, constan en forma digital.*

VEGA BAZANTES, JORGE DAVID
Estudiante

Firmado electrónicamente por:
CRISTIAN ISAAC
VACACELA GOMEZ

Dr. VACACELA GOMEZ, CRISTIAN ISAAC , Ph.D.
Presidente Tribunal de Defensa

Dr. PINTO ESPARZA, HENRY PAUL , Ph.D.
Tutor

Dra. PERALTA ARCIA, MAYRA ALEJANDRA DE JESUS , Ph.D.
Miembro No Tutor

ALARCON FELIX, KARLA ESTEFANIA
Secretario Ad-hoc

Autoría

Yo, Jorge David Vega Bazantes, con cédula de identidad 1004139653, declaro que las ideas, juicios, valoraciones, interpretaciones, consultas bibliográficas, definiciones y conceptualizaciones expuestas en el presente trabajo, así como los procedimientos y herramientas utilizadas en la investigación, son de absoluta responsabilidad del autor del trabajo de integración curricular. Así mismo, me acojo a los reglamentos internos de la Universidad de Investigación de Tecnología Experimental Yachay.

Urcuquí, octubre 2020.

Jorge David Vega Bazantes
C.I. 1004139653

Autorización de publicación

Yo, Jorge David Vega Bazantes, con cédula de identidad 1004139653, cedo a la Universidad de Tecnología Experimental Yachay, los derechos de publicación de la presente obra, sin que deba haber un reconocimiento económico por este concepto. Declaro además que el texto del presente trabajo de titulación no podrá ser cedido a ninguna empresa editorial para su publicación u otros fines, sin contar previamente con la autorización escrita de la Universidad.

Asimismo, autorizo a la Universidad para que realice la digitalización y publicación de este trabajo de integración curricular en el repositorio virtual, de conformidad a lo dispuesto en el Art. 144 de la Ley Orgánica de Educación Superior.

Urcuquí, octubre 2020.

Jorge David Vega Bazantes
C.I. 1004139653

Acknowledgements

Resumen

En el contexto del descubrimiento de nuevos materiales, es posible llevar a cabo la intercalación de átomos de litio (Li) entre capas de NbS_2, sin embargo, solo unos pocos trabajos experimentales y teóricos tratan acerca de este material [1–3]. Recientemente, Damien Voiry del Institut Européen des Membranes en Francia, desarrolló algunos experimentos con $LiNbS_2$ brindando información interesante al respecto. Por tanto, hemos realizado la descripción del $LiNbS_2$ con los funcionales más avanzados de la teoría del funcional de la densidad (DFT). En este trabajo damos a conocer cálculos detallados con la DFT acerca del *bulk* y varias superficies de $LiNbS_2$. Además, describimos varias simulaciones de la estructura electrónica y atómica, parámetros de red, imágenes de microscopía de efecto túnel (STM), fonones, y más. Los cálculos fueron realizados con el funcional meta-GGA SCAN, y algunas variaciones del funcional híbrido HSE, ambos implementados en VASP. En nuestro estudio encontramos que el funcional SCAN+rVV10 describe muy bien algunas propiedades de $LiNbS_2$ y NbS_2. Por otro lado, empleamos los híbridos HSE12 y HSE12s, y los comparamos con el funcional ampliamente usado HSE06. El rendimiento de los funcionales híbridos es tratado también. Sorprendentemente, encontramos que la intercalación de litio en NbS_2 produce un band-gap considerable, convirtiendo al material en semiconductor y por ende dando lugar a aplicaciones tecnológicas prometedoras.

Palabras clave: Teoría del funcional de la densidad, materiales en capas, intercalación, di-calcogenuros, estructura electrónica.

Abstract

In the context of the discovery of new materials, an intercalation of Lithium (Li) atoms among layers of NbS_2 can be performed. However, there are just a few experimental works and references that deal with this material[1–3]. Recently, Damien Voiry from Institut Européen des Membranes in France, has performed some experiments with $LiNbS_2$ providing some insights about it. Therefore we have worked on describing this material with the state of the art *non-empirical* density functionals of DFT. In this work we present detailed density functional theory calculations of the bulk and several surfaces of $LiNbS_2$. We describe various insights regarding the electronic and atomic structure, lattice parameters, scanning tunneling microscopy images, phonons, and so on. The computations were performed with the meta-GGA SCAN functional and some variations of the hybrid HSE as implemented in VASP. We found out that SCAN+rVV10 performs very well in the description of certain properties of $LiNbS_2$ and NbS_2. Besides, we tested the hybrids HSE12 and HSE12s and compared them with the customary HSE06. The performance of the hybrids is discussed too. Surprisingly, we find that the intercalation of Li on NbS_2 produces a considerable band gap, making the material a semiconductor and providing promising technological applications.

Keywords: Density-functional theory, layered materials, intercalation, di-chalcogenides, electronic-structure.

Contents

List of Figures

List of Tables

Chapter 1

Introduction

Research at the atomic level is very important as it implies from solving complex theoretical problems, to develop techniques that allow reproducibility in the experiments. Furthermore, the investigation at the atomic scale has an impact on several fields which include the environment, health, agriculture, technology, economy, and so on, being in itself an important matter for academia and industry [4,5]. For instance, various benefits are coming from various fields such as photovoltaics [6,7], pharmaceutics, electronics, auto-parts, etc. Thanks to the increasing of computational power and the refinement of both, theoretical and experimental techniques, studying materials provides reliability and constitutes a key aspect for making intellectual advances in science and crucial contributions to the development of the society.

At the beginning of the XXI century, a great breakthrough emerged via the discovery of graphene, a class of layered material with a honeycomb lattice structure. Since then, a myriad of studies have been published, nevertheless, other 2D layered materials were not part of that research trend and hence were not considered for thorough studies [8].

Recently, the interest in other layered materials apart from graphene had a revival. One class of these materials is known as transition metal dichalcogenides (TMD). There have been several publications [9,10] which indicate the potential applications of TMDs such as optoelectronics [11], photovoltaics, ultrathin field effect transistors [12], light-emitting diodes [13] and quantum computing. Specifically, TMDs present interesting physical effects such as the dominance of d-electron orbitals in the valence and conduction bands, and van der Waals interactions. Besides, phenomena related to spin orbit-coupling [12], charge density wave (CDW) order and superconductivity can arise [14]. Moreover, effects such as the shift of the bandgap value depending on the number of layers of a TMD have been predicted [9,11].

The previous considerations constitute interesting physical effects which have not been explored in all the existing TMDs. Also, there are several of aspects that have not been studied [6]. For instance, the behaviour of TMDs systems in the presence of defects and various possible atomic arrangements of TMDs that could be stable. Furthermore, in the framework of non-empirical DFT methods for describing the electronic structure of TMDs, there are no studies that use the most recent density functionals such as SCAN or modifications of the customary hybrid functionals as HSE.

Niobium Sulfide (NbS_2) is a class of TMD layered material which presents interesting electronic properties and is a promising material to be used in quantum computing. Some experiments on bulk and thin films of NbS_2 have shown remarkable features such as superconductivity and metallic transport properties[11,15]. Besides, it has been shown that this material has applications in quantum engineering, i.e. miniaturized neuromorphic computing[15].

As NbS_2 has a layered structure, we can think about intercalating some compound among the layers. The experimental realization of this idea has been performed by intercalating atoms of lithium in NbS_2 to obtain $LiNbS_2$[1–3,16]. There are some approximations to understand its behaviour via automated DFT calculations[17–19], however, this system has been explored thoroughly neither experimentally nor theoretically. In this context, we aim to study the electronic structure of $LiNbS_2$ assiduously, employing the state-of-the-art methods of density-functional theory.

1.1 Problem Statement

The structure of $LiNbS_2$ presents various interesting challenges. First of all, we have niobium in the structure, this implies that we are going to deal with d orbitals. In general, trying to perform simulations of structures with d or f orbitals is difficult. Furthermore, if we use DFT for simulating structures with transition metals there are some drawbacks which may be minimized by choosing appropriate exchange-correlation functionals and corrections. Besides, as we have a 2D layered material, we have to consider van der Waals interactions. Also, there are scarce publications that give insight about $LiNbS_2$. Hence, with the presence of d orbitals plus van der Waals effects, a theoretical challenge of a completely unknown structure appears.

1.2 General and Specific Objectives

The main objective of this thesis is to compute with density-functional theory (DFT) the electronic structure of $LiNbS_2$. Specifically, we aim to:

- Explain the theoretical foundations of DFT with a focus on the SCAN and HSE functionals (Chapter 2).

- Explain the methodology for studying $LiNbS_2$ (Chapter 3).

- Study the bulk NbS_2 (Chapter 4.1).

- Study the system of bulk $LiNbS_2$ for several symmetries and analyze its stability (Chapter 4.2).

- Study the surfaces of $LiNbS_2$ considering pristine structures and defects (Chapter 4.2.4 to 4.2.6).

- Compute STM images (Chapter 4.2.7).

- Compute phonons (Chapter 4.2.8).

- State some conclusions and remarks about all the research (Chapter 5).

Chapter 2

Theoretical Background

2.1 Many-body Schrödinger equation

As a starting point we have to consider the interactions in the atomic systems in the non-relativistic regime. If there are N electrons we can label their positions as $\mathbf{r}_1, \mathbf{r}_2, \ldots, \mathbf{r}_N$. If there are M nuclei the labels can be set as $\mathbf{R}_1, \mathbf{R}_2, \ldots, \mathbf{R}_M$. We have electrostatic or Coulombic interactions that contribute to the total potential energy V as follows[20,21]:

1. electron-electron $(e - e)$ interaction, i.e. two electrons repel one another:

$$V_{(e-e)} = \frac{1}{2} \sum_{i \neq j} C \frac{1}{|\mathbf{r}_i - \mathbf{r}_j|} \, , \tag{2.1}$$

2. nucleus-nucleus $(n - n)$ interaction, i.e. two nucleus repel each other:

$$V_{(n-n)} = \frac{1}{2} \sum_{I \neq J} C \frac{Z_I Z_J}{|\mathbf{R}_I - \mathbf{R}_J|} \, , \tag{2.2}$$

3. electron-nucleus $(e - n)$ interaction, i.e. an electron and a nucleus attract each other:

$$V_{(e-n)} = - \sum_{i \neq I} C \frac{Z_I}{|\mathbf{r}_i - \mathbf{R}_I|} \, , \tag{2.3}$$

where the sub-indexes' sums for the nuclei are capitalized, and the ones for the electrons are lowercase. In addition, the constant C is given by

$$C = \frac{e^2}{4\pi\epsilon_0} \, . \tag{2.4}$$

Remember that e is the charge of the electron, and ϵ_0 is the vacuum permittivity.

Setting N the number of electrons of our system and M the number of nuclei, i runs from 1 to N and I from 1 to M[21].

Now, consider the contributions for kinetic energy K, we have

$$K = \sum_{i=1}^{N} \frac{p_i^2}{2m_e} + \sum_{I=1}^{M} \frac{P_I^2}{2M_I} , \qquad (2.5)$$

where m_e is the mass of the electron and M_I represents the mass of the I-th nucleus.

To establish the general equation to be used in quantum mechanics, we have to take into account the position and momentum operators, where the last has the form:

$$\hat{p} = -i\hbar^2 \nabla^2 , \qquad (2.6)$$

where $\hbar$ is the reduced Planck's constant (i.e. $\hbar = h/2\pi$). ∇^2 acts with respect to each particle, for instance if we have i particles the operator is given by

$$\nabla_i^2 = \frac{\partial^2}{\partial x_i^2} + \frac{\partial^2}{\partial y_i^2} + \frac{\partial^2}{\partial z_i^2} . \qquad (2.7)$$

Till here almost all the ingredients we need are ready. Now, take into account the many-body wavefunction Ψ. It will have all the information of the electrons' and nuclei's positions. It can be written as

$$\Psi = \Psi(\mathbf{r}_1, \mathbf{r}_2, \ldots, \mathbf{r}_N; \mathbf{R}_1, \mathbf{R}_2, \ldots, \mathbf{R}_M) . \qquad (2.8)$$

Then, we can build a Hamiltonian using the kinetic and potential operators. Applying it to the wavefunction we obtain

$$(\hat{K} + \hat{V})\Psi = E_{tot}\Psi , \qquad (2.9)$$

where E_{tot} is the total energy of the system. Then, using equations (2.1) to (2.9) we can write the full many-body Schrödinger equation,

$$\left(-\sum_{i=1}^{N} \frac{\hbar^2}{2m_e}\nabla_i^2 - \sum_{I=1}^{M} \frac{\hbar^2}{2M_I}\nabla_I^2 + \frac{1}{2}\sum_{i \neq j} C\frac{1}{|\mathbf{r}_i - \mathbf{r}_j|} + \frac{1}{2}\sum_{I \neq J} C\frac{Z_I Z_J}{|\mathbf{R}_I - \mathbf{R}_J|} - \sum_{i \neq I} C\frac{Z_I}{|\mathbf{r}_i - \mathbf{R}_I|} \right)\Psi = E_{tot}\Psi . \qquad (2.10)$$

Notice that the equation (2.10) does not have experimental values as inputs and just takes into account the fundamental constants of equation (2.16). A theory with this type of equations is known as having a first-principles approach, otherwise it would be a phenomenological approach.

Also, consider the probability of simultaneously find electrons (labeled with sub-index i) at positions $\mathbf{r}_i$ respectively[21], given as

$$|\Psi|^2 = |\Psi(\mathbf{r}_1, \ldots, \mathbf{r}_N; \mathbf{R}_1, \ldots, \mathbf{R}_M)|^2 . \qquad (2.11)$$

The electron density, which is the probability of finding any electron at position $\mathbf{r}$ is given by[21]

$$n(\mathbf{r}) = N \int |\Psi|^2 d\mathbf{r}_2 \ldots d\mathbf{r}_N d\mathbf{R}_1 \ldots d\mathbf{R}_M \, . \tag{2.12}$$

If Ψ is normalized to 1 we have:

$$\int |\Psi|^2 d\mathbf{r}_2 \ldots d\mathbf{r}_N d\mathbf{R}_1 \ldots d\mathbf{R}_M = 1 \, . \tag{2.13}$$

Therefore, the integral of the electronic charge density is the number of electrons, this is

$$\int n(\mathbf{r}) d\mathbf{r} = N \, . \tag{2.14}$$

One remarkable feature of equation (2.10) is that if we are aiming to solve it in a computer, its complexity increases exponentially with the size of the system[21]. This means that the matrix operations we would have to deal with will be really huge, and hence not solvable. We will see in the next sections how we can handle this problem.

2.2   The Born-Oppenheimer (BO) approximation

In general, the BO approximation states that the total wave function can be expressed as the product of the electronic wave function (depending on electronic coordinates with the nuclei at fixed positions) Ψ_R, and the wave function of the nucleus (as a function of nuclear coordinates with the electrons on some fixed state)[22] χ, so that

$$\Psi(\mathbf{r}_1, \ldots, \mathbf{r}_N; \mathbf{R}_1, \ldots, \mathbf{R}_M) = \Psi_{\mathbf{R}}(\mathbf{r}_1, \ldots, \mathbf{r}_N)\chi(\mathbf{R}_1, \ldots, \mathbf{R}_M) \, . \tag{2.15}$$

The BO approximation is also called adiabatic approximation. In general, atoms are of masses that are 10^4 to 10^5 times larger than the electron's mass. Hence, the electrons are 10^2 to 10^3 times faster than the nuclei (which will be expressed in the kinetic energy). Therefore, it is possible to assume that the electrons follow the nuclei's motion instantaneously[23].

Then, we have a framework in which the electrons contribute with potential energy for the motion of the nuclei. On the other hand, the moving nuclei continuously deform the wave function of the electrons and do not cause abrupt changes[22]. Remember that this approximation holds only for materials in their equilibrium configuration[21]. Then, based on BO approximation we can start to simplify the original many-body Schrödinger equation (2.10). First, let me rewrite equation (2.10) considering **atomic units**.

2.2.1   Atomic units

It is known that fundamental physical constants are independent of the system we are dealing with. They are given by:

$$\hbar = 1.05457163 \cdot 10^{-34} J \cdot s \, ,$$
$$m_e = 9.10938291 \cdot 10^{-31} kg \, ,$$
$$m_p = 1.67262164 \cdot 10^{-27} kg \, , \tag{2.16}$$
$$e = 1.60217649 \cdot 10^{-19} C \, ,$$
$$\epsilon_0 = 8.85418782 \cdot 10^{-12} F/m \, .$$

We can also consider the Bohr radius a_0, which is the average distance between the nucleus and the electron of Hydrogen in its ground state,

$$a_0 = 0.529 \text{Å} \, . \tag{2.17}$$

We notice that the potential energies of equation (2.10) are given by Hartrees Ha, then

$$E_{Ha} = \frac{e^2}{4\pi\epsilon_0 a_0} \, . \tag{2.18}$$

Besides, it is possible to handle the kinetic energies of equation (2.10) considering

$$\hbar = m_e v a_0 \, , \tag{2.19}$$

which is the angular momentum in the ground state of Hydrogen in the Bohr model. Also, take into account

$$\frac{1}{2} m_e v^2 = \frac{1}{2} E_{Ha} \, , \tag{2.20}$$

which is the kinetic energy expressed in orders of E_{Ha}. The previous equation came from equating the centrifugal force and the nuclear attraction.

Therefore, with equations (2.16) to (2.20) we have the set of equations:

$$\frac{\hbar^2}{2m_e} = \frac{m_e v^2 a_0^2}{2} = \frac{1}{2} E_{Ha} a_0^2 \, , \tag{2.21}$$

$$\frac{\hbar^2}{2M_I} = \frac{m_e v^2 a_0^2}{2(M_I/m_e)} = \frac{1}{2} \frac{E_{Ha} a_0^2}{M_I/m_e} \, , \tag{2.22}$$

and

$$C = \frac{e^2}{4\pi\epsilon_0} = a_0 E_{Ha} \, . \tag{2.23}$$

Replacing the three previous equations into equation (2.10) we have:

$$\left(-\sum_{i=1}^{N} \frac{1}{2} E_{Ha} a_0^2 \nabla_i^2 - \sum_{I=1}^{M} \frac{1}{2} \frac{E_{Ha} a_0^2}{M_I/m_e} \nabla_I^2 + \frac{1}{2} \sum_{i \neq j} a_0 E_{Ha} \frac{1}{|\mathbf{r}_i - \mathbf{r}_j|} + \frac{1}{2} \sum_{I \neq J} a_0 E_{Ha} \frac{Z_I Z_J}{|\mathbf{R}_I - \mathbf{R}_J|} - \sum_{i \neq I} a_0 E_{Ha} \frac{Z_I}{|\mathbf{r}_i - \mathbf{R}_I|} \right) \Psi = E_{tot} \Psi \, . \tag{2.24}$$

Finally, dividing the last equation by E_{Ha} we get:

$$\left(-\sum_{i=1}^{N}\frac{1}{2}a_0^2\nabla_i^2 - \sum_{I=1}^{M}\frac{1}{2}\frac{a_0^2}{M_I/m_e}\nabla_I^2 + \frac{1}{2}\sum_{i\neq j}a_0\frac{1}{|\mathbf{r}_i - \mathbf{r}_j|} + \frac{1}{2}\sum_{I\neq J}a_0\frac{Z_I Z_J}{|\mathbf{R}_I - \mathbf{R}_J|} - \sum_{i\neq I}a_0\frac{Z_I}{|\mathbf{r}_i - \mathbf{R}_I|}\right)\Psi = \frac{E_{tot}}{E_{Ha}}\Psi. \quad (2.25)$$

Notice that we have simplified the initial many-body Schödinger equation. We can even go further by setting this equation in units of Hartrees (Ha), bohrs (a_0), and atomic units (a.u.). Also, setting $e = 1$ we get:

$$\left(-\sum_{i=1}^{N}\frac{1}{2}\nabla_i^2 - \sum_{I=1}^{M}\frac{1}{2}\frac{\nabla_I^2}{M_I} + \frac{1}{2}\sum_{i\neq j}\frac{1}{|\mathbf{r}_i - \mathbf{r}_j|} + \frac{1}{2}\sum_{I\neq J}\frac{Z_I Z_J}{|\mathbf{R}_I - \mathbf{R}_J|} - \sum_{i\neq I}\frac{Z_I}{|\mathbf{r}_i - \mathbf{R}_I|}\right)\Psi = E_{tot}\Psi, \quad (2.26)$$

where 1 Ha = $27.211 eV$, $1a_0 = 0.529$Å, 1 a.u. of mass = $m_e = 9.109 \cdot 10^{-31}$ kg.

Equation (2.26) is a more compact version of the many-body Schrödinger equation, nevertheless remember that it yields a very high complexity when trying to solve it. If we consider equation (2.26) and the BO approximation, we can now have more simplifications. First, if the nuclei are fixed, we have that $M_I = \infty$, then

$$\sum_{I=1}^{M}\frac{1}{2}\frac{\nabla_I^2}{M_I} \approx 0. \quad (2.27)$$

Also, as proposed in ref.[21], we can define

$$E = E_{tot} - \frac{1}{2}\sum_{I\neq J}\frac{Z_I Z_J}{|\mathbf{R}_I - \mathbf{R}_J|}, \quad (2.28)$$

and

$$\sum_{i}V_n(\mathbf{r}_i; \mathbf{R}) = -\sum_{i\neq I}\frac{Z_I}{|\mathbf{r}_i - \mathbf{R}_I|}. \quad (2.29)$$

Hence, equation (2.26) can be written as

$$\left(-\sum_{i=1}^{N}\frac{1}{2}\nabla_i^2 + \sum_{i}V_n(\mathbf{r}_i; \mathbf{R}) + \frac{1}{2}\sum_{i\neq j}\frac{1}{|\mathbf{r}_i - \mathbf{r}_j|}\right)\Psi_{\mathbf{R}} = E_{\mathbf{R}}\Psi_{\mathbf{R}}, \quad (2.30)$$

where the subscript $\mathbf{R}$ is to denote the fixed nuclear coordinates. It is important to note that $\mathbf{R}$ does not act as a variable but as parameter. In the previous equation it follows $E = E_{\mathbf{R}}$.

From here, we can compute a many-body Schrödinger equation as a function of just the nuclei. Replacing equations (2.15) and (2.30) into (2.10) we get

$$\left(-\sum_{i=1}^{N}\frac{1}{2}\frac{\nabla_i^2}{M_I} + \frac{1}{2}\sum_{I\neq J}\frac{Z_I Z_J}{|\mathbf{R}_I - \mathbf{R}_J|} + E_{\mathbf{R}}\right)\chi = E_{tot}\chi. \quad (2.31)$$

The effect of the electrons is contained in $E_{\mathbf{R}} = E(\mathbf{R}_1, \ldots, \mathbf{R}_M)$. $E_{\mathbf{R}}$ acts as an 'effective potential' for the nuclei[21]. In summary, the most remarkable result that we have obtained for the BO approximation is the decoupling of equation (2.10) into (2.30) and (2.31). For a more formal treatment and some historical insights it is advised to review ref.[22].

2.3   Hartree-Fock (HF) theory

Let me consider the equation (2.30) again:

$$\left(-\sum_{i=1}^{N}\frac{1}{2}\nabla_i^2 + \sum_i V_n(\mathbf{r}_i;\mathbf{R}) + \frac{1}{2}\sum_{i\neq j}\frac{1}{|\mathbf{r}_i - \mathbf{r}_j|}\right)\Psi_{\mathbf{R}} = E_{\mathbf{R}}\Psi_{\mathbf{R}}.$$

Then, let us define the many-electron Hamiltonian

$$\hat{H}(\mathbf{r}_1,\ldots,\mathbf{r}_N) = -\sum_{i=1}^{N}\frac{1}{2}\nabla_i^2 + \sum_i V_n(\mathbf{r}_i;\mathbf{R}) + \frac{1}{2}\sum_{i\neq j}\frac{1}{|\mathbf{r}_i - \mathbf{r}_j|}. \tag{2.32}$$

Hence, we can express equation (2.30) as

$$\hat{H}\Psi = E\Psi. \tag{2.33}$$

Also, we can define the single-electron Hamiltonian as

$$\hat{H}_0(\mathbf{r}) = -\frac{1}{2}\nabla^2 + V_n(\mathbf{r}). \tag{2.34}$$

Notice that equation (2.34) does not take into account the electron-electron interaction and consequently it is a considerable simplification. (2.34) is a second order partial differential equation that could be solved by customary methods, nevertheless if there are N number of electrons, then we will have a partial differential equation in $3N$ unknowns. Hence, trying to solve that kind of system would be impossible[23].

To handle this problem, we can re-write (2.34) as a set of algebraic equations in matrix form. Notice that if we use a basis set, we will just find an approximate solution to the true many-body Schröndiger equation. It is possible to check the accuracy of our solution and its convergence. Let us consider the ground state energy E_0 so that we can define the **Rayleigh-Ritz variational principle**: "The expectation value of the Hamiltonian in any state $|\Psi\rangle$ is always larger than or equal to the ground state energy E_0"[23], this can be expressed as

$$E_0 \leq \frac{\langle\Psi|\hat{H}|\Psi\rangle}{\langle\Psi|\Psi\rangle}. \tag{2.35}$$

Then, if we consider an initial guess for $|\Psi\rangle$, $\langle\Psi|\hat{H}|\Psi\rangle/\langle\Psi|\Psi\rangle$ will be an upper bound for E_0[23]. So, let us consider the Hamiltonian (2.34). We can write

$$\sum_i \hat{H}_0(\mathbf{r}_i)\Psi_H = E\Psi_H, \tag{2.36}$$

where the subscript H is to denote that we are working in the Hartree scheme. So, if the electrons are not interacting, we can write Ψ_H as

$$\Psi_H(\mathbf{r}_1,\ldots,\mathbf{r}_N) = \phi_1(\mathbf{r}_1)\ldots\phi_N(\mathbf{r}_N), \tag{2.37}$$

where we are assuming that each particle state is occupied once, and the probability of finding an electron i at $\mathbf{r}_i$ is given by the product of individual probabilities $|\phi(\mathbf{r}_i)|^2$.

Then, we have:

$$\hat{H}_0(\mathbf{r})\phi_i(\mathbf{r}) = \varepsilon_i^0\phi_i(\mathbf{r}), \tag{2.38}$$

and expanding the previous equation we obtain

$$\left(-\frac{1}{2}\nabla^2 + V_n(\mathbf{r})\right)\phi_i(\mathbf{r}) = \varepsilon_i^0\phi_i(\mathbf{r})\,. \tag{2.39}$$

Then, let us find the expectation value of the Hamiltonian (2.32) with

$$\langle\Psi_H|\hat{H}|\Psi_H\rangle = \sum_{i=1}^{N}\int d^3r\phi_i^*(\mathbf{r})\left(-\frac{1}{2}\nabla^2 + V_n(\mathbf{r})\right)\phi_i(\mathbf{r}) + \frac{1}{2}\sum_{i,j=1}^{N}\int d^3rd^3r'\frac{1}{|\mathbf{r}-\mathbf{r}'|}|\phi_i(\mathbf{r})|^2|\phi_j(\mathbf{r}')|^2\,. \tag{2.40}$$

The energy E_H of this system is a functional of the wave functions ϕ. As this function is complex we can write E_H in terms of both real and imaginary parts of ϕ[23]:

$$\langle\Psi_H|\hat{H}|\Psi_H\rangle = E_H[\phi_i^*, \phi_i]\,. \tag{2.41}$$

Then, we can minimize (through the Lagrange multipliers method) the previous result with respect to $\phi_i^*(\mathbf{r})$. We consider as a constraint the normalization condition $\langle\phi_i|\phi_i\rangle = 1$ of the wave functions given as

$$\frac{\delta}{\delta\phi_i^*}\left(\langle\Psi_H|\hat{H}|\Psi_H\rangle - \sum_{i=1}^{N}\{\varepsilon_i(1 - \langle\phi_i|\phi_i\rangle)\}\right) = 0\,, \tag{2.42}$$

where every ε_i act as the Lagrange multiplier. Then, by this minimization we obtain the **Hartree equations**[23,24]:

$$\left(-\frac{1}{2}\nabla^2 + V_n(\mathbf{r}) + \sum_{j=1}^{N}\int d^3r'\frac{|\phi_j(\mathbf{r}')|^2}{|\mathbf{r}-\mathbf{r}'|}\right)\phi_i(\mathbf{r}) = \varepsilon_i\phi_i(\mathbf{r})\,. \tag{2.43}$$

The previous result can also be obtained through a **mean field approximation**. This is, in the framework of classical electrostatics, let us consider the distribution of electronic charge $n(\mathbf{r})$, which will produce an electrostatic potential $\Phi(\mathbf{r})$, then

$$\nabla^2\Phi(\mathbf{r}) = 4\pi n(\mathbf{r})\,, \tag{2.44}$$

where the electrons in this system will have the potential energy $V_H(\mathbf{r}) = -\Phi(\mathbf{r})$. Hence, replacing this result in the previous equation we get

$$\nabla^2 V_H(\mathbf{r}) = -4\pi n(\mathbf{r})\,. \tag{2.45}$$

The solution for equation (2.45) is

$$V_H(\mathbf{r}) = \int d\mathbf{r}'\frac{n(\mathbf{r}')}{|\mathbf{r}-\mathbf{r}'|}\,, \tag{2.46}$$

which is named the Hartree potential.

Then, remember that we have defined the single-electron Hamiltonian H_0 in equation (2.34). We neglected the term of electron-electron interaction, nevertheless now we have the Hartree potential experienced by electrons, so that we just add this potential to H_0. Hence, we can write a more compact form of the Hartree equations as

$$\left(-\frac{\nabla^2}{2} + V_n(\mathbf{r}) + V_H(\mathbf{r})\right)\phi_i(\mathbf{r}) = \varepsilon_i\phi_i(\mathbf{r})\,, \tag{2.47}$$

where we have defined:

$$n(\mathbf{r}) = \sum_i |\phi_i(\mathbf{r})|^2 \, . \tag{2.48}$$

Notice that the Hartree equations have the form of the one-particle Schrödinger equation. To find the solution of this system we can apply a self-consistency cycle, which means that we use an initial guess of the solution, and make various iterations that yield a new density and a new effective potential. This is performed till the difference of the new result and the previous one is in terms of a certain reasonable tolerance[23]. Finally, in this mathematical framework we write the Hartree energy E_H as

$$\langle \Psi_H | \hat{H} | \Psi_H \rangle = E_H = \sum_{i=1}^N \varepsilon_i - V_H \, . \tag{2.49}$$

Note that V_H is subtracted as it is already counted twice in the Hartree eigenvalue[23].

One important aspect of quantum mechanics that we have not considered yet is the Pauli exclusion principle. This means that the sign of a quantum state $|\phi\rangle$ changes when there is the exchange of two electrons. Therefore, instead of using the solution for Ψ proposed in equation (2.37) given by the product of ϕ_is, we have to use a Slater determinant so that we account for the Pauli principle[23], so that

$$\Psi_{HF} = \Psi_{HF}(\mathbf{r}_1 \sigma_1, \ldots, \mathbf{r}_N \sigma_N) = \frac{1}{\sqrt{N!}} \begin{vmatrix} \phi_1(\mathbf{r}_1 \sigma_1) & \phi_1(\mathbf{r}_2 \sigma_2) & \cdots & \phi_1(\mathbf{r}_N \sigma_N) \\ \phi_2(\mathbf{r}_1 \sigma_1) & \phi_2(\mathbf{r}_2 \sigma_2) & \cdots & \phi_2(\mathbf{r}_N \sigma_N) \\ \vdots & \vdots & \ddots & \vdots \\ \phi_N(\mathbf{r}_1 \sigma_1) & \phi_N(\mathbf{r}_2 \sigma_2) & \cdots & \phi_N(\mathbf{r}_N \sigma_N) \end{vmatrix}, \tag{2.50}$$

where we have introduced information about spin via σ, and N is the number of electrons. Then, as done before with the Hartree approach

$$\langle \Psi_{HF} | H | \Psi_{HF} \rangle = \sum_{i=1}^N \int d^3 r \phi_i^*(\mathbf{r}) \left(-\frac{1}{2} \nabla^2 + V_n(\mathbf{r}) \right) \phi_i(\mathbf{r}) + \frac{1}{2} \sum_{i,j=1}^N \int d^3 r d^3 r' \frac{1}{|\mathbf{r} - \mathbf{r}'|} |\phi_i(\mathbf{r})|^2 |\phi_j(\mathbf{r}')|^2$$
$$- \frac{1}{2} \sum_{i,j=1}^N \int d^3 r d^3 r' \frac{1}{|\mathbf{r} - \mathbf{r}'|} \delta_{\sigma_i \sigma_j} \phi_i^*(\mathbf{r}) \phi_i(\mathbf{r}') \phi_j^*(\mathbf{r}') \phi_j(\mathbf{r}) \tag{2.51}$$

so, we get

$$\langle \Psi_{HF} | H | \Psi_{HF} \rangle = E_{HF}[\phi_i^*, \phi_i] \, . \tag{2.52}$$

Notice that we have an additional term accounting the electrons with same spin. This term is known as the exchange potential V_X. Then, minimizing the previous expression with respect to ϕ_i^* we can obtain the **Hartree-Fock equations**[23]:

$$\left(-\frac{\nabla^2}{2} + V_n(\mathbf{r}) + V_H(\mathbf{r}) \right) \phi_i(\mathbf{r}) - \sum_{j=1}^N \int d^3 r' \frac{1}{|\mathbf{r} - \mathbf{r}'|} \phi_j^*(\mathbf{r}') \phi_i(\mathbf{r}') \phi_j(\mathbf{r}) \delta_{\sigma_i \sigma_j} = \epsilon_i \phi_i(\mathbf{r}) \, . \tag{2.53}$$

Sometimes the exchange term is written as[21]

$$-\sum_{j=1}^{N} \int d^3 r' \frac{1}{|\mathbf{r} - \mathbf{r}'|} \phi_j^*(\mathbf{r}')\phi_i(\mathbf{r}')\phi_j(\mathbf{r})\delta_{\sigma_i\sigma_j} = \int V_X(\mathbf{r}, \mathbf{r}')\phi(\mathbf{r}')d^3 r',$$ (2.54)

with

$$V_X(\mathbf{r}, \mathbf{r}') = -\frac{1}{|\mathbf{r} - \mathbf{r}'|}\phi_j^*(\mathbf{r}')\phi_j(\mathbf{r}).$$ (2.55)

Then, to summarize the main result we have that[23]:

$$\langle \Psi_{HF}|H|\Psi_{HF}\rangle = E_{HF} = \sum_{i=1}^{N} \epsilon_i - E_H - E_X,$$ (2.56)

where we have defined both the Hartree energy E_H and the exchange Energy E_X. These energies have to be subtracted since they are already twice in the Hartree-Fock eigenvalues[23]. To end this section, it is advisable to review ref.[24] for a good explanation about minimizing functionals and a detailed and formal derivation of the results of the Hartree-Fock theory.

2.4 Density Functional Theory (DFT)

DFT is a useful framework that allows to study various many-body electronic systems and obtain results regarding the properties and defects of metals, metal and semiconductor surface physics, relativistic effects, magnetism, electron-hole droplets in semiconductors, excited states, and more interesting physics[25]. The foundation of DFT was based on the seminal paper of P. Hohenberg and W. Kohn in 1964[26]. Hence, I start with the study of two fundamental theorems that are the basis of DFT.

2.4.1 Hohenberg-Kohn (HK) Theorems

2.4.1.1 First HK Theorem

Based on the original paper of Hohenberg and Kohn[26], let us consider the following[25]:

1. A system of N_e electrons enclosed in a large box and moving under the influence of some external potential $V(\mathbf{r}) = V_{ext}$ and of their mutual Coulomb repulsion.

2. The Hamiltonian operator (in atomic units) with the same form as equation (2.30):

$$\hat{H} = -\sum_{i=1}^{N} \frac{1}{2}\nabla_i^2 + \sum_i V(\mathbf{r}_i) + \frac{1}{2}\sum_{i\neq j} \frac{1}{|\mathbf{r}_i - \mathbf{r}_j|},$$ (2.57)

so that, we can simplify the notation as

$$\hat{H} = \hat{T} + V_{ext} + V_{ee} = (\hat{T} + V_{ee}) + V_{ext} = \hat{H}_0 + \sum_i V(\mathbf{r}_i),$$ (2.58)

where

$$\hat{T} = -\sum_i \frac{1}{2}\nabla_i^2, \quad V_{ee} = \frac{1}{2}\sum_{i\neq j}\frac{1}{|\mathbf{r}_i - \mathbf{r}_j|}, \quad V_{ext} = V(\mathbf{r}_i) = -\sum_{i\neq I}\frac{Z_I}{|\mathbf{r}_i - \mathbf{R}_I|} + \text{adittional fields}. \qquad (2.59)$$

Hence, V_{ee} is the potential energy between electrons, $\hat{T}$ is the kinetic energy operator, and V_{ext} is a one-particle potential produced by the nuclei and felt by the electrons. It is remarkable to mention that V_{ext} could also include some additional (to the electron-nuclei interaction term) fields [24]. Also, in this case $\hat{H}_0 = \hat{T} + V_{ee}$.

3. The ground state of the system Ψ is non-degenerate.

Therefore, "if the total number N_e of the electrons is fixed, the potential $V(\mathbf{r}_i) = V_{ext}$ results in a unique wave function Ψ for the ground state which, in turn, gives rise to the unique electron density $n(\mathbf{r})$" [24]. This is

$$V(\mathbf{r}_i) = V_{ext} \rightarrow \Psi \rightarrow n(r). \qquad (2.60)$$

In other words, we have stated that the electronic density $n(\mathbf{r})$ in the ground state Ψ is a functional of $V(\mathbf{r}_i)$ [26]. Now, we have to prove the opposite, i.e. " the potential $V(r_i)$ and the wave function Ψ of the ground state are uniquely determined by the density $n(\mathbf{r})$" [24]. Or, as stated by Hohenberg and Kohn [26]: we have to show that $V(r_i)$ is a unique functional of $n(\mathbf{r})$.

Now, let us consider the expression for the total energy E:

$$E = \left\langle \Psi \left| \sum_{i=1}^{N_e} V(\mathbf{r}_i) \right| \Psi \right\rangle + \langle \Psi | \hat{T} + V_{ee} | \Psi \rangle, \qquad (2.61)$$

where

$$\left\langle \Psi \left| \sum_{i=1}^{N_e} V(\mathbf{r}_i) \right| \Psi \right\rangle = \int V(\mathbf{r}) n(\mathbf{r}) d\mathbf{r}. \qquad (2.62)$$

Therefore, let us assume there are two different potentials $V(\mathbf{r})$ and $V'(\mathbf{r})$ corresponding to the wave functions Ψ and Ψ' that result in the same density $n(\mathbf{r})$ [24]. The expressions for the energy are

$$E = \langle \Psi | \hat{H} | \Psi \rangle \qquad (2.63)$$

and

$$E' = \langle \Psi' | \hat{H}' | \Psi' \rangle, \qquad (2.64)$$

where $\hat{H}' = \hat{H}_0 + V'_{ext}$.

Then, as we have stated that Ψ is the ground state for the potential $V(\mathbf{r})$, we have:

$$E = \langle \Psi | \hat{H} | \Psi \rangle < \langle \Psi' | \hat{H} | \Psi' \rangle = \langle \Psi' | \hat{H}' | \Psi' \rangle + \langle \Psi' | V_{ext} - V'_{ext} | \Psi' \rangle, \qquad (2.65)$$

where we have used the fact that: $\hat{H}' + [V_{ext} - V'_{ext}] = (\hat{H}_0 + V'_{ext}) + [V_{ext} - V'_{ext}] = \hat{H}_0 + V_{ext} = \hat{H}$. Hence, replacing the expression for E' based on equation (2.64) we obtain

$$E < E' + \langle \Psi' | V_{ext} - V'_{ext} | \Psi' \rangle. \qquad (2.66)$$

Following equations (2.62) and (2.59) we can replace the brackets by integrals of $V(\mathbf{r})$ and the density $n(\mathbf{r})$ to get

$$E < E' + \left[\int V(\mathbf{r})n(\mathbf{r})d\mathbf{r} - \int V'(\mathbf{r})n(\mathbf{r})d\mathbf{r} \right], \tag{2.67}$$

so that

$$E < E' + \int n(\mathbf{r})[V(\mathbf{r}) - V'(\mathbf{r})]d\mathbf{r}. \tag{2.68}$$

In the same manner, we can follow the previous reasoning but starting with Ψ' as the ground state, then

$$E' < \langle \Psi | \hat{H}' | \Psi \rangle = E + \langle \Psi | V'_{ext} - V_{ext} | \Psi \rangle, \tag{2.69}$$

so that

$$E' < E - \int n(\mathbf{r})[V(\mathbf{r}) - V'(\mathbf{r})]d\mathbf{r}. \tag{2.70}$$

Adding (2.68) and (2.70) we get:

$$E - E' + E' - E < 0, \tag{2.71}$$

implying

$$0 < 0, \tag{2.72}$$

which is not true. This approach is known as *reductio ad absurdum*, and we can conclude that assuming that the same density $n(\mathbf{r})$ corresponds to two different potentials is not true. Consequently, there must exist a unique density for an external potential. Finally, we can state that the total energy can be expressed as the "sum of a unique functional of the density, and the interaction energy of the electrons with the external potential"[24]. So we can write

$$E \equiv E[n(\mathbf{r})] = F_{HK}[n(\mathbf{r})] + \int n(\mathbf{r})V(\mathbf{r})d\mathbf{r}, \tag{2.73}$$

where

$$\langle \Psi | \hat{H}_0 | \Psi \rangle = \langle \Psi | \hat{T} + V_{ee} | \Psi \rangle \equiv F_{HK}[n(\mathbf{r})]. \tag{2.74}$$

In summary, we have proved the existence of the energy representation through a universal functional[24].

2.4.1.2 Second HK Theorem

First, let us consider a density $n'(\mathbf{r}) \neq n(\mathbf{r})$. $n'(\mathbf{r})$ corresponds to Ψ' and the Hamiltonian $\hat{H}$ is the same in both cases. We have stated that Ψ' is not the true ground state function[24], therefore

$$E[n(\mathbf{r})] = \langle \Psi | \hat{H} | \Psi \rangle < \langle \Psi' | \hat{H} | \Psi' \rangle, \tag{2.75}$$

which implies that

$$E[n(\mathbf{r})] < F_{HK}[n'(\mathbf{r})] + \int n'(\mathbf{r})V(\mathbf{r})d\mathbf{r} \equiv E[n'(\mathbf{r})]. \tag{2.76}$$

So, in summary we have arrived at

$$E[n(\mathbf{r})] < E[n'(\mathbf{r})]. \tag{2.77}$$

Then, we know that the energy is a unique functional of the density. Furthermore, we can affirm that the true density has the lowest energy. Hence, we can find the correct density by means of the variational principle of the energy functional with respect to the density[24], that is

$$\delta \left\{ E[n(\mathbf{r})] - \mu \left(\int n(\mathbf{r}) d\mathbf{r} - N_e \right) \right\} , \tag{2.78}$$

where we have assumed differentiability of $E[n(\mathbf{r})]$ and that the ground-state density satisfy the stationary principle[27]. Then, we obtain the Euler-Lagrange equation

$$\mu = \frac{\delta E[n(\mathbf{r})]}{\delta n(\mathbf{r})} = V(\mathbf{r}) + \frac{\delta F_{HK}[n]}{\delta n(\mathbf{r})} , \tag{2.79}$$

where μ is the chemical potential. Notice that F_{HK} is a universal functional of the density $n(\mathbf{r})$ as it does not depend on the external potential V_{ext}. This implies that if we know some (approximate or accurate) form of F_{HK} we can use this method in any system. Finding F_{HK} in an explicit form is a challenging task[27].

2.4.2 Levy constrained-search method

It is also possible to prove the Hohenberg-Kohn theorems in a more general manner via the method proposed by M. Levy[24,27]. Here I will not show the mathematical details but rather the main remarks provided by Levy. First, we say that a density $n(\mathbf{r})$ is V-representable if "it can be constructed from the antisymmetrised ground state wave function Ψ of a Hamiltonian with some $V(\mathbf{r})$"[24].

The universal functional for any V-representable density is defined as

$$F_{HK}[n_0] = Min_{\Psi \to n_0} \langle \Psi | \hat{T} + V_{ee} | \Psi \rangle , \tag{2.80}$$

which acts as a constrained-search for the density functional $F_{HK}[n_0]$. The subscript 0 is to refer to the ground state. If we perform the search over all the antisymmetric wave functions that output n_0, $F_{HK}[n_0]$ yields the minimum expectation value of $\langle \hat{T} + V_{ee} \rangle$. Then, the definition $F_{HK}[n_0]$ is useful for deriving the first Hohenberg-Kohn (HK) theorem, and even more allows us to get rid of the assumption that there should be no degeneracy in the ground state. In this framework, it is also possible to derive the second (HK) theorem and also the condition of N_e-representability can be introduced. This condition requires " the density to be derivable from some antisymmetric N_e-electron wave function"[24].

Then, we have a mathematical framework that allows to search for the true density that minimizes the energy in the set of trial densities constrained by normalization and N_e-representability[24].

2.5 Kohn-Sham theory

It is remarkable to mention that the Kohn-Sham (KS) method is " a practical tool for rigorous calculations" as it provides a practical way to deal with the kinetic energy functional $\hat{T}[n(\mathbf{r})]$[27]. Here I present the main result provided by Kohn and Sham, for more formal approaches we can refer to refs.[23,24,27].

Let us consider equation (2.73)

$$E \equiv E[n(\mathbf{r})] = F_{HK}[n(\mathbf{r})] + \int n(\mathbf{r})V(\mathbf{r})d\mathbf{r},$$

where we have defined:

$$F_{HK}[n(\mathbf{r})] \equiv \langle \Psi | \hat{H}_0 | \Psi \rangle = \langle \Psi | \hat{T} + V_{ee} | \Psi \rangle. \tag{2.81}$$

The dependence of F_{HK} on $n(\mathbf{r})$ is only implicit. Hence, Kohn and Sham proposed to "split these implicit terms into the kinetic and Coulomb energy of independent electrons" as we have done before in the Hartree approach (eqn. (2.47)), but adding an extra term that takes into account the difference[21]. Therefore, we can write

$$E = \int d\mathbf{r} n(\mathbf{r})V_n(\mathbf{r}) - \sum_i \int d\mathbf{r} \phi_i^*(\mathbf{r})\frac{\nabla^2}{2}\phi_i(\mathbf{r}) + \frac{1}{2}\int\int d\mathbf{r}d\mathbf{r}'\frac{n(\mathbf{r})n(\mathbf{r}')}{|\mathbf{r}-\mathbf{r}'|} + E_{xc}[n]. \tag{2.82}$$

Notice that the first three terms in the previous equation correspond to the total energy $E_{V_{ee}=0}$ in the independent electrons approximation (or just what we obtain setting $V_{ee} = 0$), this is

$$E_{V_{ee}=0} = \int d\mathbf{r} n(\mathbf{r})V_n(\mathbf{r}) - \sum_i \int d\mathbf{r} \phi_i^*(\mathbf{r})\frac{\nabla^2}{2}\phi_i(\mathbf{r}) + \frac{1}{2}\int\int d\mathbf{r}d\mathbf{r}'\frac{n(\mathbf{r})n(\mathbf{r}')}{|\mathbf{r}-\mathbf{r}'|}. \tag{2.83}$$

Remember that the first term with V_n corresponds to the external potential, the second one $\frac{-\nabla^2}{2}$ is the kinetic energy, and the third one is the Hartree term. E_{xc} is called the exchange and correlation (or exchange-correlation (xc)) energy, and contains "everything that is left out"[21]. In general what we have expressed in equation (2.82) is an splitting of $E[n]$ based on the already studied and known contributions of the non-interacting (or independent) electrons approximation and an unknown contribution expressed in E_{xc}.

Then, if we follow the minimization of the functional $E[n]$ as we did when deriving the Hartree-Fock equations, we get

$$\frac{\delta E[n]}{\delta n}\bigg|_{n_0} = 0. \tag{2.84}$$

Remember that with the previous minimization we will obtain an expression for the wave functions $\phi_i(\mathbf{r})$, which follows

$$n(\mathbf{r}) = \sum_i |\phi_i|^2,$$

i.e. if we know ϕ_i we can build the density. Also we impose orthonormality,

$$\int d\mathbf{r} \phi_i^*(\mathbf{r})\phi_j(\mathbf{r}) = \delta_{ij}. \tag{2.85}$$

And hence we obtain the Kohn-Sham equations:

$$\left(-\frac{\nabla^2}{2} + V_n(\mathbf{r}) + V_H(\mathbf{r}) + V_{xc}(\mathbf{r})\right)\phi_i(\mathbf{r}) = \varepsilon_i\phi_i(\mathbf{r}), \tag{2.86}$$

where V_n is the external potential, V_H is the Hartree potential, and V_{xc} is the exchange and correlation potential which given by

$$V_{xc}(\mathbf{r}) = \frac{\delta E_{xc}[n]}{\delta n}\bigg|_{n(\mathbf{r})}. \tag{2.87}$$

Notice that the exact form of E_{xc} is not known and therefore a challenging task will be to find approximations to this functional[21]. Also, as we have been doing previously we can write the energy in the compact form[23]

$$E = \sum_i^N \varepsilon_i + E_{xc}[n] - \int V_{xc}(\mathbf{r})n(\mathbf{r})d^3r - V_H . \tag{2.88}$$

The exchange and correlation functional for the energy can be expressed as[23]

$$E_{xc}[n] = \int d^3rn(\mathbf{r})\epsilon_{xc}([n],(\mathbf{r})), \tag{2.89}$$

where ϵ_{xc} is the exchange and correlation energy per particle at the point $\mathbf{r}$, but dependent on the whole electron density $n(\mathbf{r})$.

Finally, as mentioned when deriving the Hartree-Fock equations, the Kohn-Sham equations can be solved via a self-consistency cycle. This process is summarized in figure (2.1).

2.6 DFT functionals

In this section I will refer to the main results provided in DFT theory to understand better the basis of the approximations for exchange-correlation energy functionals. Therefore, I follow a more formal approach [*].

Remember we already considered the total energy E given by equation (2.82) in the Kohn-Sham theory. This energy can be written more generally as

$$E = T_s[n_\uparrow, n_\downarrow] + \int d^3r \, n(\mathbf{r})v(\mathbf{r}) + U[n] + E_{xc}[n_\uparrow, n_\downarrow], \tag{2.90}$$

where:

- $n_\uparrow(\mathbf{r})$ and $n_\downarrow(\mathbf{r})$ are spin densities. Then, T_s is the non-interacting kinetic energy functional of the spin densities, $v(\mathbf{r})$ is the external potential (due to the nuclei).

- $U[n]$ is the Hartree electrostatic self-repulsion of the electron density:

$$U[n] = \frac{1}{2} \int d^3r \int d^3r' \frac{n(\mathbf{r})n(\mathbf{r}')}{|\mathbf{r} - \mathbf{r}'|} . \tag{2.91}$$

- Finally, E_{xc} is the exchange-correlation energy. Its functional derivative yields the exchange-correlation functional:

$$v_{xc}^\sigma([n_\uparrow, n_\downarrow]; \mathbf{r}) = \frac{\delta E_{xc}}{\delta n_{\sigma(\mathbf{r})}} . \tag{2.92}$$

Notice we already derived this equation but here is expressed more formally including even the spin indexes σ. E_{xc} includes all the information that is not considered in the first three terms of equation (2.90). If we were able to know the exact form of E_{xc} on $n_\uparrow$ and $n_\downarrow$, it would be possible to know "the exact ground-state energy and spin-densities of a many-electron system"[20]. Furthermore, the forces on the nuclei would be found by $-\partial E/\partial \mathbf{R}$[20].

---

[*]If one is really interested on a more detailed theoretical framework about DFT functionals, I strongly recommend to look at the chapter by John P. Perdew and Stefan Kurthin in the book *A Primer in Density Functional Theory*[20].

2.6.1 Exchange-correlation functional E_{xc}

Let us consider the exchange-correlation energy functional E_{xc}, it can be split as [20]

$$E_{xc}[n] = E_x[n] + E_c[n],\tag{2.93}$$

where $E_x[n]$ is the exchange energy contribution, and is given as [20]

$$E_x[n] = \langle \phi_n^{min}|\hat{V}_{ee}|\phi_n^{min}\rangle - U[n],\tag{2.94}$$

where ϕ_n^{min} is a single Slater determinant. Besides [20],

$$\langle \phi_n^{min}|\hat{T} + \hat{V}_{ee}|\phi_n^{min}\rangle = T_s[n] + U[n] + E_x[n].\tag{2.95}$$

If the interaction between electrons is switched-off $\hat{V}_{ee} = 0$. In other words, we consider the one-electron limit, hence we have [20]:

$$E_x[n] = -U[n].\tag{2.96}$$

On the other hand, the correlation energy E_c is given as [20]:

$$E_c[n] = F[n] - \{T_s[n] + U[n] + E_x[n]\} = \langle \Psi_n^{min}|\hat{T} + \hat{V}_{ee}|\Psi_n^{min}\rangle - \langle \phi_n^{min}|\hat{T} + \hat{V}_{ee}|\phi_n^{min}\rangle.\tag{2.97}$$

Notice that $F[n]$ was already defined in equation (2.74) [as $F_{HK}[n]$], and more generally in equation (2.80), however to be consistent with the formalism of this section we have [20]

$$F[n] = min_{\Psi \rightarrow n}\langle \Psi|\hat{T} + \hat{V}_{ee}|\Psi\rangle = \langle \Psi_n^{min}|\hat{T} + \hat{V}_{ee}|\Psi_n^{min}\rangle.\tag{2.98}$$

Here Ψ_n^{min} is the wave function that yields the density n and minimizes $\langle \hat{T} + \hat{V}_{ee}\rangle$ [20].

2.6.2 Coupling-Constant Integration

We have seen the exact expressions for E_x, in equation (2.94), and E_c in (2.97), though they do not provide a physical insight to construct an approximated functional. To overcome this problem, as is customary done by physicists, we can insert a coupling constant $\lambda > 0$. The idea is then to perform a coupling constant integration, or also known as the adiabatic connection [33].

We consider a normalized antisymmetric wave function $\Psi_n^{min,\lambda}$, that yields a density $n(\mathbf{r})$ and minimizes the expectation value of the expression $\hat{T} + \lambda\hat{V}_{ee}$ [20,33], this is

$$\Psi_n^{min,\lambda} = \begin{cases} \Psi_n^{min} & \text{if } \lambda = 1 \\ \phi_n^{min} & \text{if } \lambda = 0 \end{cases},\tag{2.99}$$

where Ψ_n^{min} is the interacting ground-state wave function for density n, and ϕ_n^{min} is the non-interacting or Kohn-Sham wave function for density n [20]. The change of λ at fixed $n(\mathbf{r})$ represents a change in the external potential $v_\lambda(\mathbf{r})$ that is given as

$$v_\lambda(\mathbf{r}) = \begin{cases} \text{the true external potential} & \text{if } \lambda = 1 \\ \text{the Kohn-Sham effective potential} & \text{if } \lambda = 0 \end{cases}.\tag{2.100}$$

Then, after some steps of mathematical treatment, we can consider the average density of electrons $n_2(\mathbf{r}, \mathbf{r}')$ [†] at $\mathbf{r}'$, given that there is one electron at $\mathbf{r}$ [33]. Then, it follows that

$$\int d^3r' n_2(\mathbf{r}, \mathbf{r}') = N - 1 . \tag{2.101}$$

Also, we can define

$$n_2(\mathbf{r}, \mathbf{r}') = n(\mathbf{r}') + n_{xc}^\lambda(\mathbf{r}, \mathbf{r}') , \tag{2.102}$$

where $n_{xc}^\lambda(\mathbf{r}, \mathbf{r}')$ is the density at $\mathbf{r}'$ of the exchange-correlation hole about one electron in $\mathbf{r}$ [20]. Then, we have:

$$\int d^3r' n_{xc}^\lambda(\mathbf{r}, \mathbf{r}') = -1 . \tag{2.103}$$

The interpretation of the previous equation is that if an electron is at $\mathbf{r}$, hence it is missing in the rest of the system [20]. Then, we can arrive at another expression of the exchange-correlation energy:

$$E_{xc}[n] = \frac{1}{2} \int d^3r \int d^3r' \frac{n(\mathbf{r})\bar{n}_{xc}(\mathbf{r}, \mathbf{r}')}{|\mathbf{r} - \mathbf{r}'|} , \tag{2.104}$$

where

$$\bar{n}_{xc}(\mathbf{r}, \mathbf{r}') = \int_0^1 d\lambda n_{xc}^\lambda(\mathbf{r}, \mathbf{r}') \tag{2.105}$$

is the coupling-constant averaged hole density [20].

Therefore, with the previous framework in mind, it is possible to have a clearer physical insight about E_{xc}, which is "just the electrostatic interaction between each electron and the coupling-constant-averaged exchange-correlation hole which surrounds it" [20]. Now, we can move on our analysis of functionals.

2.6.3   Hierarchy of E_{xc} DFT functionals

As it is difficult to find the functional $E_{xc}[n]$ and consequently the exchange correlation energy $\epsilon_{xc}([n], \mathbf{r})$ there has been an extensive work on approximations for $E_{xc}[n]$. From around the 60's the efforts for understanding and constructing accurate and efficient functionals have arisen. There are two types of functionals: non-empirical and empirical. The first are constructed only with mathematical parameters and fundamental physical constants, whereas the latter depend on experimental parameters. This thesis is devoted only to the non-empirical functionals.

Jianwei Sun [‡], describes a systematic way to produce non-empirical functionals. I summarize this process along with historical insights in Table 2.1.

Now, remember that we already stated in equation (2.89) the expression for the exchange-correlation energy:

$$E_{xc}[n] = \int d^3r n(\mathbf{r})\epsilon_{xc}([n], (\mathbf{r})) .$$

[†] The sub-script 2 is used just to follow the notation that is used in refs. [20,33]

[‡] Jianwei Sun along with Adrienn Ruzsinszky and John P. Perdew (one of the most cited scientists in history [34]) created the SCAN functional [35], one of the main tools that was used in this thesis. Sun et al. wrote a chapter book [33] to explain the basics of DFT and how SCAN works, hence I follow his work. As an interesting fact, I met Ruzsinszky and Perdew in a series of conferences at San Francisco University in Quito in 2019.

Table 2.1: Adapted from the work by Jianwei Sun et al.[33]: The systematic, nonempirical way to improve approxima-
tions to the exact density functional for the exchange-correlation energy E_{xc}. Notice that the first appropriate norm
for step (v) was the uniform electron gas in 1965. The most recent functional that fulfills all steps from (i) to (v) is
the strongly constrained and appropriately normed (SCAN)[35] density functional.

Steps	Historical context
(i) Prove the existence of the exact functional and derive exact formal expressions for it.	1965-79
(ii) Discover mathematical properties of the exact functional (exact constraints), which include limits, scaling relations, equalities, and bounds.	1980's
(iii) Develop approximate but computationally tractable forms for the approximations at various levels of flexibility.	1965-98
(iv) Impose the "exact constraints" from step (ii) on each form, as appropriate	1970-present*
(v) If a form still retains some flexibility, fit it to energies/densities of appropriate norms, systems for which the form can be expected to be highly accurate.	1965, 2015

*The book was published on 2018.

2.6.3.1 The Local Spin Density Approximation

We can start considering $\epsilon_{xc}([n], \mathbf{r})$ for the homogeneous (or uniform) electron gas, a system with constant $n(\mathbf{r})$. This
framework is known as the Local Spin Density Approximation (LSDA) or just Local Density Approximation (LDA),
which is also used in non-homogeneous situations[23]. Hence, we will have an expression of the form:

$$E_{xc}^{LSDA}[n_\uparrow, n_\downarrow] = \int d^3r\, n(\mathbf{r})\epsilon_{xc}^{unif}(n_\uparrow, n_\downarrow),\tag{2.106}$$

where $\epsilon_{xc}^{unif}(n_\uparrow, n_\downarrow)$ is the exchange-correlation energy per electron for the uniform electron gas.

This expression has been useful for certain problems of bulk and surface structures, nevertheless it has some
drawbacks at obtaining accurate cohesive energies, lattice constants and bond lengths[23].

2.6.3.2 The General Gradient Approximation GGA

An improved version of the LSDA approach is the Generalized Gradient Approximation (GGA). Here, we consider
the second-order gradient expansion of the density $n(\mathbf{r})$ to LSDA for the exchange-correlation energy. One challenge
that arises, is that the exchange-correlation hole in the GGA approach $\bar{n}_{xc}(\mathbf{r}, \mathbf{r}+\mathbf{u})$ is not realistic as LSDA is at large
$\mathbf{u}$. To overcome this problematic behavior, Perdew and Wang came up with a solution and proposed the so called
PW91 functional[36]. However, some years later a more updated version of this class of GGAs emerged thanks to the
work by Perdew, Burke, and Ernzerhof[37]. This GGA is widely known and abbreviated as PBE. The general form of
a GGA functional is as follows:

$$E_{xc}^{GGA}[n_\uparrow, n_\downarrow] = \int d^3r\, n(\mathbf{r})\epsilon_{xc}^{unif}(n)F_{xc}(n_\uparrow, n_\downarrow, \nabla n_\uparrow, \nabla n_\downarrow),\tag{2.107}$$

where F_{xc} is the enhancement factor.

GGA functionals achieve chemical accuracy (with an error up to $\leq 0.1 eV$) for various chemical reactions. Thanks to this improvement Walter Kohn was awarded with the Nobel Prize in chemistry in 1998 for his development of the density-functional theory[23]. As the GGA approximation seems promising there are still some drawbacks. In general, we can mention:

- No proper description of van der Waals forces.

- Underestimation of band gaps (both in GGA and LDA).

- Wrong prediction of the magnetization of strongly correlated systems. For instance, Nickel Oxide (NiO) is predicted as metal instead of an antiferromagnetic insulator.

As pointed out by Groß[23], "there is no systematic way of improving the functionals since there is no expansion in some controllable parameter". Furthermore, Sun et al.[33] state that there is a dilemma about GGAs, i.e. they can be accurate for structures or energies, but not both. This aspect is due to a formal limitation, this is that a GGA functional "cannot satisfy all the known exact constraints appropriate to a semilocal functional"[33].

2.6.3.3 Meta-GGA

One step forward in the exchange-correlation functional is the meta-GGA's. This approximation consider additional semilocal information[33] such as the Laplacian of the density $\nabla^2_{n_\sigma}$ or the kinetic energy density τ_σ, or both. It can be expressed as[33]:

$$E_{xc}^{MGGA}[n_\uparrow, n_\downarrow] = \int d^3r \, n(\mathbf{r}) \epsilon_{xc}^{unif}(n) F_{xc}(n_\uparrow, n_\downarrow, \nabla n_\uparrow, \nabla n_\downarrow, \nabla^2 n_\uparrow, \nabla^2 n_\downarrow, \tau_\uparrow, \tau_\downarrow).$$

(2.108)

The Kohn-Sham orbital kinetic energy density for electrons of spin σ is defined as[20]

$$\tau_\sigma(\mathbf{r}) = \frac{1}{2} \sum_\alpha \theta(\mu - \epsilon_{\alpha\sigma}) |\nabla \psi_{\alpha\sigma}(\mathbf{r})|^2,$$

(2.109)

where μ is the chemical potential. α represents the set of remaining one-electron quantum numbers (apart from the z-component of the spin $\sigma = \uparrow, \downarrow$). $\theta(\mu - \epsilon_{\alpha\sigma})$ is a step function which ensures that when $\epsilon_{\alpha\sigma} < \mu$ all Kohn-Sham spin orbitals are singly occupied, whereas if $\epsilon_{\alpha\sigma} > \mu$ these orbitals are empty.

The kinetic energy density contributes to overcome the GGA's dilemma mentioned before because meta-GGAs satisfy more exact constraints[33]. In this framework, we can use a dimensionless variable α[33]:

$$\alpha = \frac{\tau - \tau^w}{\tau^{unif}},$$

(2.110)

where

$$\tau^{unif} = \frac{3}{10} \cdot (3\pi^2)^{2/3} n^{5/3}$$

(2.111)

is the kinetic energy density of the uniform electron gas[33]. Also,

$$\tau^w = \frac{|\nabla n|^2}{8n} \tag{2.112}$$

is the von Weizsäcker kinetic energy density. It is exact for single-orbital systems[33].

With the previous definitions in mind, it is remarkable that meta-GGAs are able to recognize the accurate α for various cases[33]:

- Slowly varying densities, when $\alpha \approx 1$. Then, simulating metallic bonds.

- Single-orbital systems, when $\alpha = 0$, simulating covalent single bonds.

- Single-orbital systems, when $\alpha \gg 1$, for non-covalent bonds between closed shells.

Meta-GGAs are in principle intrinsically non-local functionals, due to the fact that they are determined by Kohn-Sham orbitals (which are non-local functionals of the electron density)[33]. With this consideration, in 2011 Nazarov and Vignale[38] showed that (as pointed by Sun et al.[33]) "the exchange-correlation kernel derived from meta-GGAs within the adiabatic TDDFT[§] can provide a nonlocality"[33][¶].

2.6.3.4 Meta-GGA example: Strongly Constrained and Appropriately Normed Semilocal (SCAN) Density Functional

From the previous discoveries, the non-empirical SCAN meta-GGA emerged in 2015[33]. SCAN is one remarkable state-of-the-art functional up to date. It was published by Jianwei Sun, Adrienn Ruzsinszky and John P. Perdew, the last being one of the creators of the PBE (GGA) functional[‖]. SCAN is "the first meta-generalized-gradient approximation (meta-GGA) that is fully constrained, obeying all 17 known exact constraints that a meta-GGA can. It is also exact or nearly exact for a set of "appropriate norms", including rare-gas atoms and nonbonded interactions[35]."

SCAN is able to recognize several chemical bonds via the parameter α we defined earlier. Therefore, SCAN predicts accurate geometries and energies of various systems such as covalent, metallic, ionic, hydrogen, and van der Waals bonds. Furthermore, SCAN represents a significant and systematic improvement over the GGAs[33,39]. In 2016 (one year later of the original publication), it was shown that "SCAN matches or improves on the accuracy of a computationally expensive hybrid functional, at almost-GGA cost" in some cases[39].

To understand SCAN remember what was mentioned in Table (2.1). More specifically, the 17 SCAN constraints are distributed as[33]:

- 6 for exchange

[§]TDDFT holds for Time Dependent DFT.

[¶]More technically, what Nazarov and Vignale showed is that the exchange-correlation kernel of meta-GGA supports a singularity of the form α/q^2, where q is the wave vector. This singularity is important for a theory to describe the excitonic effect in crystals. Notice that the definition of the kernel f_{xc}, appears in the TDDFT framework, for more details about f_{xc} see the publication by Nazarov and Vignale[38].

[‖]Notice that PBE was published in 1996[37], and it took almost 20 years to have a very improved version of a functional. This is a milestone in the history of simulations and solid state physics; also it shows the complexity of describing the many-body effects at quantum level.

- 6 for correlation

- 5 for both exchange and correlation

Also, SCAN considers the next appropriate norms[33]:

- uniform and slowly varying densities

- the jellium surface energy

- the H atom

- the He atom and the limit of large atomic number for the rare-gas atoms, including Ar_2

- the $Z \rightarrow \infty$ limit of the two-electron ion

SCAN has shown a very good performance predicting various effects of the so called intermediate-range van der Waals interactions. There are various examples that show an advantage in relation to the PBE functional such as the description of defects in semiconductors, seven phases of ice, liquid silicon, liquid water, some metal oxides and more[33]. For more details about some advantages of SCAN see refs.[33,39,40].

As we have seen with other functionals, SCAN also presents a drawback in some systems. For instance, when we have long-range van der Waals (vdW) interactions (which are non local), SCAN (which is semi-local) cannot properly describe the system. To overcome this challenge, we could account for other methods such as Quantum Montecarlo (QMC) simulations, or the random-phase approximation RPA, nevertheless they are suitable for not very big systems as it could represent high computational cost. Then, to solve this problem we can combine the SCAN approach with the rVV10[41] density functional. rVV10 is first principles (or non-empirical), and in combination with SCAN, we can afford for the SCAN+rVV10[42] functional in order to describe van der Waals interactions that SCAN alone cannot[33].

2.6.3.5   Hyper-GGA

The class of hyper-GGAs functionals add the exact exchange energy density ϵ_{xc}^{exact} to the previous meta-GGA. ϵ_{xc}^{exact} is a fully nonlocal functional of the occupied Kohn-Sham orbitals[33]. Then, hyper-GGAs have the form:

$$E_{xc}^{MGGA}[n_\uparrow, n_\downarrow] = \int d^3r \, n(\mathbf{r}) \epsilon_{xc}^{unif}(n) F_{xc}(n_\uparrow, n_\downarrow, \nabla n_\uparrow, \nabla n_\downarrow, \nabla^2 n_\uparrow, \nabla^2 n_\downarrow, \tau_\uparrow, \tau_\downarrow, \epsilon_{xc}^{exact}) . \tag{2.113}$$

2.6.3.6   Hybrid functionals

There are also the class of hybrid functionals, which combine DFT and exact Hartree-Fock exchange[43]. Specifically, remember when we defined the coupling constant integration in equation (2.99); then at $\lambda = 0$ is the exact exchange hole. This fact suggested that a fraction of exact exchange should be mixed with GGA exchange and correlation[20]. The simplest hybrid can be written as[20]:

$$E_{xc}^{hyb} = aE_x^{exact} + (1 - a)E_x^{GGA} + E_c^{GGA} , \tag{2.114}$$

where a is a constant (also known as the mixing parameter) that can be obtained theoretically or fitted empirically[20].

As mentioned by Perdew and Kurth[20] "hybrid functionals are in a sense hyper-GGA's, but hyper-GGA's can also make use of full exact exchange and a fully nonlocal correlation functional which incorporates the exact exchange energy density...". In general, we can affirm that hyper-GGAs and hybrids are sophistications of the LSDA and GGAs and provide more accurate results. There are even more approximations that have considerable improvements in the accuracy of the calculations such as the RPA or the GW approaches[33].

All these approximations for E_{xc} can be summarized on a *Jacob's ladder*, which starts from the bottom with the LSDA, till hybrids and other approximations. The *heaven* in this analogy is the exact form of E_{xc}. Here I present a Table 2.2 adapted from the work by Sun et al.[33]

Table 2.2: Jacob's ladder of DFT functionals adapted from Sun et al.[33]. The authors clearly state that: The approximations in the lowest three rungs are semilocal since their ingredients, n, ∇n, $\nabla^2 n$, and τ only require the information at local point r or infinitesimally around r. The highest two rungs are nonlocal due to the explicit appearance of the occupied ψ_{occ} or unoccupied ψ_{unocc} orbitals in the functionals. Climbing from a lower rung to a higher rung usually results in the increase of accuracy. However, from semilocal rungs to nonlocal ones, the computational cost increases dramatically.[33]

Ingredients	Altitude	Functionals' name
	Heaven(Chemical Accuracy)	
n, ∇n, $\nabla^2 n$, τ, ψ_{occ}, ψ_{unocc}	Rung 5	RPA, GW
n, ∇n, $\nabla^2 n$, τ, ψ_{occ}	Rung 4	Hybrid functionals, e.g., HSE06
n, ∇n, $\nabla^2 n$, τ	Rung 3	Meta-GGA's, e.g., SCAN
n, ∇n	Rung 2	GGA's, e.g., PBE
n	Rung 1	LSDA

2.6.3.7 Hybrid functional example: Heyd-Scuseria-Ernzerhof (HSE)

It is know that semi-local functionals such as meta-GGAs underestimate the true values of band gaps, or fail at describing materials with elements presenting d and/or f orbitals[44]. To partially overcome these difficulties hybrid functionals (which include part of Hartree-Fock (HF) exchange[44], play an important role. One important hybrid functional is the Heyd-Scuseria-Ernzerhof (HSE) screened hybrid functional. In the HSE scheme we consider the split of the Coulumb potential $1/r$ for exchange into short-range (SR), i.e., $[1-\mathrm{erf}(\omega r)]/r$ and long-range (LR) components , i.e., $\mathrm{erf}(\omega r)/r$[44]. This can be expressed as:

$$\frac{1}{r} = \frac{1 - \mathrm{erf}(\omega r)}{r} + \frac{\mathrm{erf}(\omega r)}{r} \, , \tag{2.115}$$

so that we are constructing a screened potential, which enables to reduce the computational cost in extended systems[44]. In equation (2.115) ω is known as the screening parameter and defines the separation range. The

exchange-correlation energy for HSE is then:

$$E_{xc}^{HSE} = aE_x^{HF,SR}(\omega) + (1-a)E_x^{PBE,SR}(\omega) + E_x^{PBE,LR}(\omega) + E_c^{PBE} , \qquad (2.116)$$

where $E_x^{PBE,SR}$ is the short range component of the GGA functional PBE, $E_x^{PBE,LR}$ represents the long-range component of PBE. Both terms are obtained via integration of the PBE exchange hole. $E_x^{HF,SR}$ is the short-range HF exchange; and E_c^{PBE} is the PBE correlation energy. If $\omega = 0$, HSE reduces to another hybrid named PBEh. For $\omega \to \infty$ HSE becomes PBE. Usually, the mixing constant a is fixed as $a = 1/4$, this result is obtained from perturbation theory[44]. When we set $\omega = 0.2$ (considering $a = 1/4$), we name the functional as HSE06. However, a study in 2012 by Moussa et al.[45] showed a way to make a better selection of the parameters a and ω. Hence, I summarize the results in Table (2.3) .

ω (Å^{-1})	a	HSE name
0.2	0.25	HSE06
0.185	0.313	HSE12
0.408	0.425	HSE12s

Table 2.3: Various HSE functionals as given by the screening parameter ω and the mixing parameter a. HSE12 and HSE12s were proposed by Moussa et al.[45] in 2012, whereas HSE06 comes from the considerations of the study by Scuseria et al. in 2006[44].

2.7 Computational implementation of DFT: the Vienna *ab initio* Simulation Package (VASP)

My thesis work has been developed entirely through the VASP code implementations. I will provide the specific computational details of this thesis in the next sections, but for now I will present some important concepts that are the basis to understand the VASP code.

2.7.1 Translational Invariance and Periodic Boundary Conditions

When developing DFT calculations we assume periodicity of the system in 3D. This means that we choose a unit cell (either a primitive cell or a supercell) and make periodic extensions of it. Technically, we are working on a Bravais lattice **, and in real space we usually consider a Wigner-Seitz cell, whose analogous is the first Brillouin Zone in

---

In the Solid State Physics book by Aschroft and Mermin[46], the Bravais lattice is defined as an infinite array of discrete points with an arrangement and orientation that appears exactly the same, from whichever of the points the array is viewed. A 3D Bravais lattice is formed by the position vectors **R of the form:

$$\mathbf{R} = n_1\mathbf{a}_1 + n_2\mathbf{a}_2 + n_3\mathbf{a}_3 ,$$

where the $\mathbf{a}_1,\mathbf{a}_2$, and $\mathbf{a}_3$ are any vectors (also called primitive vectors) not laying in the same plane, and n_1, n_2, and n_3 are integers.

the reciprocal space [46]. As we repeat periodically a unit cell (ensuring the distances between cells are large enough), the band energies will be the same as the electron energy levels of a single cell [24].

If we consider a perfect periodic crystal, the ions will be arranged periodically. Hence, we can consider the case when an electron goes through a periodic potential $U(\mathbf{r})$ that is part of a Bravais lattice. We can write [46]:

$$U(\mathbf{r} + \mathbf{R}) = U(\mathbf{r}) \tag{2.117}$$

for all Bravais lattice vectors $\mathbf{R}$.

One fundamental fact about crystallographic systems is the Bloch's theorem. According to Aschroft and Mermin [46], the theorem is stated as: *The eigenstates ψ of the one-electron Hamiltonian $\hat{H} = -\frac{\nabla^2}{2} + U(\mathbf{r})$, where $U(\mathbf{r} + \mathbf{R}) = U(\mathbf{r})$ for all $\mathbf{R}$ in a Bravais lattice, can be chosen to have the form of a plane wave times a function with the periodicity of the Bravais lattice*, this is:

$$\psi_{n\mathbf{k}}(\mathbf{r}) = e^{i\mathbf{k}\cdot\mathbf{r}} u_{n\mathbf{k}}(\mathbf{r}), \tag{2.118}$$

where n the band index, and the $\mathbf{k}$ point within the Brillouin zone (BZ). For every n, the energies $\epsilon_n(\mathbf{k})$ and the wave functions $\psi_{n\mathbf{k}}(\mathbf{r})$ are some continuous functions of $\mathbf{k}$. Then, usually we state that $\epsilon_n(\mathbf{k})$ forms a band that is characterized by the quantum number n [24]. In addition,

$$u_{n\mathbf{k}}(\mathbf{r} + \mathbf{R}) = u_{n\mathbf{k}}(\mathbf{r}), \tag{2.119}$$

for all Bravais lattice vectors $\mathbf{R}$.

The implications and meaning of Bloch's theorem is nicely explained by Kantorovich [††] (Chapter 5) [24] stating that "the wave function of an electron is not periodic", nevertheless, "the density $|\psi_{n\mathbf{k}}(\mathbf{r})|^2$ associated with the state $n\mathbf{k}$ is " [24]. Then, "it is possible to try and solve the Schrödinger equation for each value of $\mathbf{k}$ independently" [47].

Furthermore: "For every given n there will be N different solutions of the Schrödinger equation corresponding to N different values of the vector $\mathbf{q}$ in the first BZ. Each of the solutions can accommodate up to two electrons with opposite spins [24]." This idea will also become important when dealing with surface systems (either pristine or with defects) [24]. Therefore, considering the Bravais framework and a parallelepiped with sides $N_1\mathbf{a}_1$, $N_2\mathbf{a}_2$, and $N_3\mathbf{a}_3$ the periodic boundary conditions are given as [24]

$$\psi_{n\mathbf{k}}(\mathbf{r} + N_1\mathbf{a}_1) = \psi_{n\mathbf{k}}(\mathbf{r} + N_2\mathbf{a}_2) = \psi_{n\mathbf{k}}(\mathbf{r} + N_3\mathbf{a}_3) \equiv \psi_{n\mathbf{k}}(\mathbf{r}). \tag{2.120}$$

Periodicity is important when dealing with surface systems. A common procedure for computing them is the so called *slab model*. This is based on the idea of considering a certain number of surface layers that will be inside a slab with a determined vacuum space. This arrangement is repeated periodically, and with an appropriate vacuum we can avoid artificial interactions. Also, the thickness of the slab should be enough so that the internal surface layers simulate the bulk of the crystal. Sometimes in the slabs, the atoms of the bottom are fixed and the remaining atoms are allowed to relax, so there is a continuous transition from the surface to the bulk region in the slab [24]. This procedure is also an important part of this work and will be better understood when working with a real example.

[††]I strongly recommend to read Chapter 5 by Kantorovich [24], see the citation number for the exact reference. This reading is very illuminating. What I cited mostly in this section from Kantorovich's work was from section 5.2.1.1

2.7.2 k-point sampling

When performing DFT calculations, we will need to evaluate integrals in the reciprocal space (or **k** space). Computationally, this can be solved by sampling and re-formulating all the DFT physics over a grid of **k** points. For instance, let us consider the electronic density [24]

$$n(\mathbf{r}) = 2 \sum_{n\mathbf{k}}^{occ} |\psi_{n\mathbf{k}}(\mathbf{r})|^2 \,, \tag{2.121}$$

where the summation is performed with respect to the lowest occupied (*occ*) states $n\mathbf{k}$ described by the Kohn-Sham orbitals $\psi_{n\mathbf{k}}(\mathbf{r})$. Here, one-electron energies ε_λ, and wave functions ψ_λ in periodic systems are labeled with the band index n and the **k** point within the Brillouin zone (BZ), then: $\varepsilon_\lambda = \varepsilon_{n\mathbf{k}}$ and $\psi_\lambda = \psi_{n\mathbf{k}}$.

The choice of the set of **k** points for representing $n(\mathbf{r})$ is known as **k**-point sampling. This choice is made as a function of the size of the unit cell and on the system point symmetry. In general, the bigger the cell, the smaller the set of **k** points that are needed. The BZ becomes smaller in the reciprocal space when the unit cell is bigger (i.e. the **k** points are closer among them and therefore we need less points).

If we have defined in real space the lattice vectors $\mathbf{a}_1$, $\mathbf{a}_2$, and $\mathbf{a}_3$, we can also define the set of vectors in reciprocal space $\mathbf{b}_1$, $\mathbf{b}_2$, and $\mathbf{b}_3$. The relation between $\mathbf{a}_i$ and $\mathbf{b}_j$ is written as

$$\mathbf{b}_1 = 2\pi \frac{\mathbf{a}_2 \times \mathbf{a}_3}{\mathbf{a}_1 \cdot (\mathbf{a}_2 \times \mathbf{a}_3)}, \quad \mathbf{b}_2 = 2\pi \frac{\mathbf{a}_3 \times \mathbf{a}_1}{\mathbf{a}_2 \cdot (\mathbf{a}_3 \times \mathbf{a}_1)}, \quad \mathbf{b}_3 = 2\pi \frac{\mathbf{a}_1 \times \mathbf{a}_2}{\mathbf{a}_3 \cdot (\mathbf{a}_1 \times \mathbf{a}_2)} \,. \tag{2.122}$$

Also, we have that $b_i = 2\pi/a$ for all i. The volume of the BZ, V_{BZ} (in reciprocal space) and the volume of the primitive cell in real space V_{cell} are related by

$$V_{BZ} = \frac{(2\pi)^3}{V_{cell}} \,. \tag{2.123}$$

Going further in the way of choosing **k**-points, VASP allows to specify the set of **k**-points as [48]:

1. An automatically generated (shifted) regular mesh of points.

2. The beginning and end-points of line segments.

3. An explicit list of points and weights.

Regarding to the equation of the density 2.121, and following the available lectures by Martijn Marsman in the VASP documentation [49,50], the sampling of the Brillouin Zone is given as

$$n(\mathbf{r}) = \sum_{n\mathbf{k}} w_\mathbf{k} f_{n\mathbf{k}} |\psi_{n\mathbf{k}}(\mathbf{r})|^2 d\mathbf{k} \,, \tag{2.124}$$

where $w_\mathbf{k}$ are the weights for each **k** point in the first BZ and $f_{n\mathbf{k}}$ is the occupation number for our system of study. This equation is the one that will be used in a DFT code and is the basic idea behind VASP's implementations.

Considering the previous framework, now we have to face a problem: we can infer that if we consider more **k** points to sample the BZ, we obtain more accuracy [51]. However, the complexity of performing an approximation for

the integral scales linearly with the number of symmetrically irreducible **k** points [‡‡]. Hence, the idea is to have a framework (or method) that allows to choose properly the **k** points so that we have a reasonable computational cost, and a good accuracy of the sampling in order to perform the integrations.

The most used framework to perform this task is the Monkhorst-Pack (MP) method[52], published on 1976. In VASP we can choose among various methods: the Monkhorst-Pack, R_k length, or the generalized regular grids[53]. The idea behind the MP method is this: "a regular grid of k-points is generated, and the Brillouin zone integral of a function is approximated by calculating the average value of the function over the k-points. The speed and accuracy [$\cdots$] may be improved by shifting the grid so that no point falls on the high-symmetry Γ point at the center of the Brillouin zone"[51].

In addition, it is remarkable to mention very recent works that have shown a considerable improvement over the MP method. For instance, there is the so-called Moreno-Soler (MS) approach. MS consists in a "search through all possible superlattices in which lattice points are separated by a distance of at least r_{min} to identify the one that results in the fewest number of irreducible k-points"[51]. At first sight, this method is computationally expensive as it is a problem of searching through various possibilities, nevertheless there are interesting works that overcome the *search* problem and hence it is possible to overcome the MP method. See for instance, the works by Wisesa et al.[51] in 2016 and the most advanced from 2020 by Morgan et al.[54].

Notice that VASP cannot "automatically construct optimal generalized regular **k**-points grids with a certain target sampling density (in the spirit of the aforementioned publications)"[53]. Further details about the k-points mesh will be discussed later. As an important fact, keep in mind that we usually specify how many **k**-points are in each direction. Hence if a certain number of **k**-points are used in each direction we can label them as

$$M \times N \times K \tag{2.125}$$

k-points. Usually, a procedure to choose a reasonable set of $M \times N \times K$ **k**-points is to perform calculations with the previous fixed cut-off energy and various separation lengths of **k**-points till observe convergence. In this way we assure to have reliable calculations and a reasonable use of computational resources.

2.7.3 Plane waves

VASP was created by Georg Kresse and various colaborators[55–58]. This code has been proved to yield reliable results[59] and is widely used to study various atomic systems. As pointed out by Hafner[43], modern DFT calculations for solids are based on technical choices such as[43]:

1. Basis set for expanding the Kohn-Sham eigenfunctions.

2. Full-potential or pseudopotential approaches of the interactions between the ionic core and the valence electrons.

3. Method for determining the eigenstates of the Kohn-Sham Hamiltonian.

[‡‡]"the largest subset of k-points for which no two k-points in the subset are symmetrically equivalent"[51]

4. Choice of the exchange-correlation functional.

In DFT codes implementations, the spin-orbitals have to be expanded as a set of basis functions. There are various choices, however for periodic systems (e.g. crystals) and especially for VASP, the appropriate choice is the plane waves. Then, let us consider a wave function:

$$\psi_{n\mathbf{k}}(\mathbf{r}) = u_{n\mathbf{k}}(\mathbf{r})e^{i\mathbf{k}\cdot\mathbf{r}}, \tag{2.126}$$

where $u_{n\mathbf{k}}(\mathbf{r})$ is periodic, following Bloch's theorem. Hence, a generic plane wave can be written as[24]

$$\phi_{\mathbf{k}+\mathbf{G}}(\mathbf{r}) = \frac{e^{i(\mathbf{k}+\mathbf{G})\cdot\mathbf{r}}}{\sqrt{\Omega}}, \tag{2.127}$$

where $\mathbf{k}$ is a vector in the Brillouin zone, $\mathbf{G}$ is a reciprocal lattice vector, Ω is the volume of the Wigner-Seitz cell. Taking into account equation (2.126) and considering periodicity we can write[60]:

$$u_{n\mathbf{k}}(\mathbf{r}) = \frac{1}{\sqrt{\Omega}} \sum_{\mathbf{G}} C_{\mathbf{G}n\mathbf{k}} e^{i\mathbf{G}\cdot\mathbf{r}} \tag{2.128}$$

and

$$\psi_{n\mathbf{k}}(\mathbf{r}) = \frac{1}{\sqrt{\Omega}} \sum_{\mathbf{G}} C_{\mathbf{G}n\mathbf{k}} e^{i(\mathbf{k}+\mathbf{G})\cdot\mathbf{r}}. \tag{2.129}$$

In the same way, the density and the potential can be written as

$$n(\mathbf{r}) = \sum_{\mathbf{G}} n_{\mathbf{G}} e^{i\mathbf{G}\cdot\mathbf{r}} \tag{2.130}$$

and

$$V(\mathbf{r}) = \sum_{\mathbf{G}} V_{\mathbf{G}} e^{i\mathbf{G}\cdot\mathbf{r}} \tag{2.131}$$

respectively.

Kantorovich[24], and Hafner[43] mention in their respective works various advantages of using plane waves:

1. The calculation of matrix elements can be performed either in reciprocal or direct spaces. It is possible to change from certain space to another via very efficient Fast Fourier Transforms algorithms, reducing the complexity of computations with respect to the amount of plane waves that are used. For instance, the potential energy has a diagonal representation in real-space, whereas the kinetic energy has a diagonal representation in momentum-space. Working with a diagonal representation is computationally better.

2. It is easy to control the convergence of the calculation with respect to the size of the basis set using a single parameter. Specifically, we can check the eigenvalues and total energies as a function of the cut-off energy, i.e., the highest kinetic energy of a plane-wave within the chosen basis set.

3. Plane waves do not depend on positions of atoms, hence the Hellmann-Feynman forces acting on the atoms and the stresses on the unit cell may be easily calculated.

4. Basis-set superposition errors are avoided.

2.7.4 Pseudopotentials

First, remember when we considered the idea of fixing the nuclei of the atoms. In solids this idea is clever and is a very good approximation, as the nuclei are almost not moving. Now, let us think about the electrons that are very near to the nucleus (core electrons), and those which are far apart from the nucleus (valence electrons). In the case of the first, they are going to have a considerable influence of a Coulomb potential of the nucleus, and will occupy a small volume around it. Hence the one-electron energies ε are large and negative. On the other hand, the valence electrons will *feel* a weaker Coulomb potential from the nucleus. They are partially screened by the core electrons and therefore their wave functions are diffuse [24].

Then, we can perform another approximation known as the frozen-core approximation. This is based on considering only the valence electrons wave functions variationally, whereas the wave functions of the core electrons are considered identical to the clamped atoms. One condition that has to be fulfilled is the orthogonality between the wave functions of the valence electrons ψ_v with respect to the core ones. This yields the nodal structure of ψ_v, and describes the oscillation of the spin-orbitals in the core regions changing their sign [24].

The previous nodal structure of the valence spin-orbitals ψ_v is problematic for we have to use more basis functions in order to expand ψ_v so that we reproduce the oscillations within the small core regions [24]. This means we should use large values of $\mathbf{G}$ for describing oscillations on a small scale. Therefore, a solution for this problem is to use a pseudo-wave function $\widetilde{\psi}_v$ for describing the valence electrons. Further, $\widetilde{\psi}_v$ does not oscillate inside the atomic core regions, whereas outside the core regions $\widetilde{\psi}_v$ is identical to ψ_v. These considerations of the form of the wave function can be expressed as [24]

$$\psi_v = \widetilde{\psi}_v - \sum_c \langle \psi_c | \widetilde{\psi}_v \rangle \psi_c \,, \tag{2.132}$$

where outside the core regions $\psi_c \simeq 0$, then $\psi_v \simeq \widetilde{\psi}_v$. On the other hand, orthogonality of ψ_v to any of the core wave functions $\psi_{c'}$ is given as

$$\langle \psi_{c'} | \psi_v \rangle = \langle \psi_{c'} | \widetilde{\psi}_v \rangle - \sum_c \langle \psi_c | \widetilde{\psi}_v \rangle \langle \psi_{c'} | \psi_c \rangle = \langle \psi_{c'} | \widetilde{\psi}_v \rangle - \sum_c \langle \psi_c | \widetilde{\psi}_v \rangle \delta_{cc'} = 0 \,, \tag{2.133}$$

where $\widetilde{\psi}_v$ will be smooth inside the core regions. Notice that the sum subindex c is indicating that the sum is performed over all the core states. Hence, using these pseudo-wave functions we will need less plane waves. However, by using this trick another complication arises. This is that if we consider the Kohn-Sham equations for either the core and the valence electrons we will have an expression of the form [24]:

$$\left(\hat{F} + \hat{V}_{ps}(\epsilon_v) \right) \widetilde{\psi}_v = \epsilon_v \widetilde{\psi}_v \,, \tag{2.134}$$

where

$$\hat{V}_{ps}(\epsilon) = \sum_c (\epsilon - \epsilon_c) |\psi_c\rangle \langle \psi_c| \tag{2.135}$$

is a non-local energy dependent pseudo-potential.

From the previous result, various methods have emerged to build energy independent pseudo-potentials. Actually, there have been various studies to produce the so-called *hard norm-conserving* and *ultrasoft* pseudo-potentials which

work well in certain cases but present some drawbacks. For instance, one disadvantage is that in this framework we cannot restore the exact wave function [24]. Also, the exchange interaction between valence and core electron presents non linearity, and hence non linear core corrections are needed in certain cases [43]. Therefore, the Projector Augmented-Wave (PAW) method can be used to overcome these difficulties.

2.7.5   The Projector Augmented-Wave (PAW) Method

The PAW method was proposed by Blöchl [61] in 1994. This method is based on the "exact partitioning" of the wave functions and allows to perform all-electron (AE) calculations instead of only considering the valence electrons pseudo wave functions as we studied in the pseudo-potentials. Particularly, in the PAW scheme the hole wave function corresponding to every electron is calculated. Besides, the PAW method resembles the computational capabilities of the ultrasoft pseudo-potentials, i.e. just a few of plane waves will be needed to expand the smooth part of the whole wave function of valence electrons [24].

Also, it is worth mentioning that the PAW method resembles the accuracy of the full-potential linearized augmented-plane-wave (FLAPW) method. Actually, FLAPW is a benchmark of DFT calculations of solids [43]. Now, to describe the PAW approach, let us consider the all-electron (AE) valence wave functions ψ_n^{AE}, they are formed from pseudo (PS) wave functions through a linear transformation [43] given by

$$|\psi_{n\mathbf{k}}^{AE}\rangle = |\psi_{n\mathbf{k}}^{PS}\rangle + \sum_i (|\phi_i^{AE}\rangle - |\phi_i^{PS}\rangle)\langle p_i^{PS}|\psi_{n\mathbf{k}}^{PS}\rangle \,. \tag{2.136}$$

To follow the notation we used for the pseudo-potentials, we can re-write the previous equation using tildes. This notation is used in the original work by Blöchl [61] and in the VASP documentation [62], so that

$$|\psi_{n\mathbf{k}}\rangle = |\widetilde{\psi}_{n\mathbf{k}}\rangle + \sum_i (|\phi_i\rangle - |\widetilde{\phi}_i\rangle)\langle \widetilde{p}_i|\widetilde{\psi}_{n\mathbf{k}}\rangle \,. \tag{2.137}$$

Specifically:

- The pseudo-orbitals $\widetilde{\psi}_{n\mathbf{k}}$ are the variational quantities and are expanded in plane waves as

$$\widetilde{\psi}_{n\mathbf{k}}(\mathbf{r}) = \langle\mathbf{r}|\widetilde{\psi}_{n\mathbf{k}}\rangle = \frac{1}{\sqrt{\Omega}} \sum_{\mathbf{G}} C_{n\mathbf{k}\mathbf{G}} e^{i(\mathbf{G}+\mathbf{k})\cdot\mathbf{r}} \,. \tag{2.138}$$

  Notice that: "An AE wave function is a full one-electron Kohn-Sham wave function and is not to be confused with a many-electron wave function" [61]. In the regions among the PAW spheres (or also known as the augmentation regions) around the atoms we have that

$$\widetilde{\psi}_{n\mathbf{k}} = \psi_{n\mathbf{k}} \,. \tag{2.139}$$

  Inside the spheres, $\widetilde{\psi}_{n\mathbf{k}}$ are an inaccurate approximation to the true wave functions $\psi_{n\mathbf{k}}$, and are used as a computational tool. Also, the PAW method implemented in VASP uses the frozen core (FC) approximation [62].

- The AE partial waves $\phi_i^{AE} = \phi_i$ are are solutions of the spherical scalar-relativistic Schrödinger equation for a nonspinpolarized atom at a reference energy ε_i in the valence regime and for an angular momentum l_i, hence

$$\left(\frac{-\nabla^2}{2} + v_{eff}^{AE}\right)|\phi_i\rangle = \varepsilon_i|\phi_i\rangle\,, \tag{2.140}$$

where v_{eff}^{AE} is the spherical component of the AE potential.

- The pseudo partial waves $\phi_i^{PS} = \widetilde{\phi}_i$ are node-less. Outside a core radius r_c, we have that $\widetilde{\phi}_i = \phi_i$.

- $p_i^{PS} = \widetilde{p}_i$ are the projector functions. These functions are dual to the partial waves, i.e.,

$$\langle\widetilde{p}_i|\widetilde{\phi}_j\rangle = \delta_{ij}\,. \tag{2.141}$$

Furthermore, in the PAW method the total charge density related to two AE orbitals $\psi_{n\mathbf{k}}$ and $\psi_{n\mathbf{k}}$,

$$n(\mathbf{r}) = \psi_{n\mathbf{k}}^*(\mathbf{r})\psi_{m\mathbf{k}}(\mathbf{r}) = \langle\psi_{n\mathbf{k}}|\mathbf{r}\rangle\langle\mathbf{r}|\psi_{m\mathbf{k}}\rangle\,, \tag{2.142}$$

can be re-written as:

$$n(\mathbf{r}) = \widetilde{n}(\mathbf{r}) - \widetilde{n}^1(\mathbf{r}) + n^1(\mathbf{r})\,, \tag{2.143}$$

where:

$$\widetilde{n}(\mathbf{r}) = \langle\widetilde{\psi}_{n\mathbf{k}}|\mathbf{r}\rangle\langle\mathbf{r}|\widetilde{\psi}_{m\mathbf{k}}\rangle\,, \tag{2.144}$$

$$\widetilde{n}^1(\mathbf{r}) = \sum_{i,j}\widetilde{\phi}_i^*(\mathbf{r})\widetilde{\phi}_j(\mathbf{r})\langle\widetilde{\psi}_{n\mathbf{k}}|\widetilde{p}_i\rangle\langle\widetilde{p}_j|\widetilde{\psi}_{m\mathbf{k}}\rangle\,, \tag{2.145}$$

and

$$n^1(\mathbf{r}) = \sum_{ij}\phi_i^*(\mathbf{r})\phi_j(\mathbf{r})\langle\psi_{n\mathbf{k}}|p_i\rangle\langle p_j|\psi_{m\mathbf{k}}\rangle\,. \tag{2.146}$$

As remarked by Hafner[43] regarding the PAW method: "A node-less pseudo wave function and the corresponding pseudo charge density are determined by solving a generalized Kohn-Sham equation in a plane wave basis."

For clarifications about the bra-ket notation used here, I strongly recommend to review the original work by Blöchl[61]. Also, the review of Hafner[43] and the VASP documentation including some tutorials may be illuminating[62]. Furthermore, in the same way we can establish similar expressions for the total energy E[43]:

$$E = \widetilde{E} - \widetilde{E}^1 + E^1\,, \tag{2.147}$$

where each term is composed of kinetic, Hartree, and exchange-correlation contributions.

Finally, in VASP "the forces on the atoms and stresses on the unit cell are calculated as derivatives of the free energy with respect to the ionic positions and the shape of the unit cell. The derivatives of the free-energy contain both Hellmann-Feynman as well as Pulay contributions"[43].

There are more mathematical details that I have not considered as it is not the scope of this thesis. The main idea with the previous mathematical background of the PAW method is to note the technical basis that VASP codes are based on. In VASP, the PAW potentials are available for the users, nevertheless they are generated and provided only by the authors, and the pseudo-potential generation package is not available[63].

2.7.6 Cut-off energy E_{cut}

One important parameter in the DFT calculations is the cut-off energy. This parameter works as a point of reference that we have to satisfy [60] in order to avoid using an excess of plane waves. We have that

$$\frac{1}{2}|\mathbf{G} + \mathbf{k}|^2 < E_{cut} . \tag{2.148}$$

One of the first steps of any DFT calculation is to determine the cut-off energy for the system of interest. This is performed by means of various computations with a fixed E_{cut}. Therefore, if we graph the total energy of the system E with respect to E_{cut}, we will find a range of energies in which E is converging, i.e. E vary in less than 1 meV/atom. Notice this follows the same procedure mentioned for the **k** points. What is customary to do at the beginning of any DFT calculation is to compute:

1. Cut-off energy convergence.

2. k-points convergence.

3. Equation of state.

With all these ingredients in mind, we can continue to any complex calculations. The previous steps are necessary for reliable results and for consistency in all the next steps after the previous three ones.

2.7.7 Birch-Murnaghan equation of state

In this thesis is employed the Birch-Murnaghan (MB) equation of state. This approach is very useful to relate the total energy of a system with the volume of its unit cell. We start considering a function of the pressure as a function of the volume [§§]:

$$P(V) = \frac{3}{2}B_0 \left[\left(\frac{V_0}{V}\right)^{7/3} - \left(\frac{V_0}{V}\right)^{5/3} \right] \left\{ 1 - \frac{3}{4}(B_0' - 4)\left[\left(\frac{V_0}{V}\right)^{2/3} - 1 \right] \right\} , \tag{2.149}$$

where V_0 is the ground state volume, B_0 is the bulk modulus [¶¶], and B_0' is the bulk modulus derivative. Here we consider V as the volume of the unit cell.

We have that at zero temperature [68]:

$$P(V) = -\frac{dE(V)}{dV} . \tag{2.150}$$

therefore

$$E(V) = -\int P(V) \, dV . \tag{2.151}$$

[§§] For a formal derivation of the equation of state considered in this thesis I recommend to review section 5.2 of ref. [64]. Also, the original work by Birch [65] can be useful. As a curiosity, notice that these two references I mentioned are related to the field of geophysics. The work by Birch [65] published in 1947 was the Paper No. 100 published under the auspices of the Committee of Experimental Geology and Geophysics, and the Division of Geological Sciences at Harvard University. Actually, DFT calculations are useful for studying materials at very high pressures present inside the Earth, or other planets. See for instance the work by Salazar J., ref. [66]

[¶¶] The bulk modulus is "a measure of the ability of a substance to withstand changes in volume when under compression on all sides" [67]

If we integrate equation (2.149) and group the terms in factors of V we obtain an expression of the form:

$$E(V) = E_0 + aV^{-2} + bV^{-2/3} + cV^{-4/3} \,, \tag{2.152}$$

where E_0, a, b, and c are constants. Notice E_0 comes from the integration, whereas the other constants are generated when re-arranging the terms.

If we know the expression $E(V)$ and its minimum $E_0(V_0)$, given by $dE(V)/dV = 0$, we can then obtain the equation for the bulk modulus B_0 [68,69] written as

$$B_0 = V_0 \frac{\partial^2 E(V)}{\partial V^2} = -V_0 \frac{\partial P(V)}{\partial V} \,. \tag{2.153}$$

In the calculations in this thesis, we will perform a fitting of the function $E(V)$ with the polynomial (2.152), then the bulk modulus will be obtained with equation (2.153).

2.8 Scanning Tunneling Microscopy (STM)

One method to study the structure of surfaces is the STM technique. It consists in approximating a sharp tip into a sample, e.g., a surface, and then measuring various properties with spacial resolution at the atomic scale [70]. Then, the experimental realization of an STM probe, as indicated by Hofer et al. [71] consists of instrumentation into an ultra-high vacuum (UHV) chamber of less than 10^{-9} Torr ($\sim 1.310^{-7}$ Pa). Furthermore, the frame of this scheme is damped, so that the external vibrations to the system of study are minimized. We can see a general arrangement of the STM experiment in figure (2.2) [71]. The main components for performing STM are a sample holder; a piezotube that holds the STM tip; an electronic feedback loop; and a computer for recording and monitor the experiment [71].

The tip for performing STM can be made of a pure metal such as tungsten or iridium, a metal alloy as PtIr, or a metal base coated with 10-20 layers of a material as Fe or Gd *** on tungsten. This tip will be at around less than 0.1 Å from the sample (which should be metallic †††), then a bias voltage is applied and the electrons from the tip can tunnel into the surface (or vice-versa). Therefore, the tip can be moved in the x, y, and z directions very precisely, based on a feedback mechanism that adjusts the tip height by approaching or not the tip to the sample in a way that the tunneling current remains constant [70].

Notice that the tunneling current is sensitive to the tip-sample distance, therefore to measure the current yields information about the surface topography. Usually, the tunneling currents are between 10 pA and 10nA [21]. Now, to model the current via first principles, Bardeen proposed a theory in 1961. It establishes a relation among the current, local Fermi levels, the density of electronic states, and the spacial overlap between the wave functions [21]. Then, in Hartree atomic units we can write [21]

$$I = 2\pi \sum_i \sum_j f(E_{T,i} - E_{T,F})[1 - f(E_{S,j} - E_{S,F})]|M_{ij}|^2 \delta(E_{T,i} - E_{S,j}) \,, \tag{2.154}$$

*** Gd holds for Gadolinium

††† A noticeable drawback of the STM technique is that the sample has to be conducting. In the case of insulator samples, a few monolayers of the insulator on a metal base are grown.

where $E_{T,i}$ and $E_{S,j}$ are the single-particle eigenvalue of the tip (T) and the sample (S) respectively. $E_{T,F}$ and $E_{S,F}$ are the local Fermi levels in the tip and the sample respectively. $E_{T,F}$ and $E_{S,F}$ are balanced via a voltage V, so that

$$E_{S,F} - E_{T,F} = V,$$ (2.155)

where we have assumed that the source of voltage has the positive end on the tip. Hence, if a negative bias is applied, electrons can tunnel from the tip to the sample.

Furthermore, f is a function known as the Fermi-Dirac thermal occupation probability function. It is written as

$$f(E) = \frac{1}{\exp(E/k_B T) + 1},$$ (2.156)

where k_B is the Boltzmann constant and T is the temperature. $f(E)$ is the probability that on average an electronic state with energy E is occupied at a temperature T. Besides, as we are dealing with electrons in a crystalline system when using $f(E)$ we are assuming that particles are indistinguishable and non-interacting; and one particle is allowed in each quantum state[21,72].

In equation (2.154) the sum

$$\sum_i f(E_{T,i} - E_{T,F}),$$ (2.157)

holds for the number of electrons that tunnel across the vacuum gap, which are proportional to the number of occupied electron states in the tip. On the other hand, the tunneling of the electrons is permitted only if the states on the other side are unoccupied, then the current is proportional to the number of unoccupied states in the sample given as[21]

$$\sum_j [1 - f(E_{S,j} - E_{S,F})].$$ (2.158)

The term M_{ij} represents the matrix elements of the *current operator*, it is expressed as[21]

$$M_{ij} = \frac{1}{2} \int d\mathbf{S} \cdot (\psi_{T,i}^* \nabla \psi_{S,j} - \psi_{S,j} \nabla \psi_{T,i}^*),$$ (2.159)

where $\psi_{T,i}$ and $\psi_{S,j}$ are the single-particle wave functions of electrons in the tip and the sample respectively. The integral run over the surface that separates the sample from the tip[21].

Finally, the function $\delta(E_{T,i} - E_{S,j})$ is only non-zero if $E_{T,i} \approx E_{S,j}$ so that the energy of the electron is conserved in the tunneling process[21]. A really nice resource regarding STM images is available at[70] http://www.fz-juelich. de/pgi/pgi-3/microscope.

2.8.1   Tersoff-Hamann Approximation of the Bardeen Model

Tersoff and Hamann in 1985 assumed that the tip is spherical, therefore the matrix element M_{ij} is proportional to the magnitude of the sample's wave function at the center of a sphere $\mathbf{r}_T$[21], then we have

$$M_{ij} = C \cdot \psi_{S,j}(\mathbf{r}_T),$$ (2.160)

where C is a constant. The tunneling current can be simplified as [21]

$$I = C \cdot \sum_j |\psi_{S,j}(\mathbf{r}_T)|^2 \delta(E_{S,j} - E_{S,F}) . \tag{2.161}$$

The previous equation implies that the current decreases exponentially when the tip is taken apart from the sample.

Then, considering the DFT theory, we can perform STM calculations based on the Kohn-Sham eigenstates ϕ_j, and its eigenvalues ε_j, so that [21]

$$\psi_{S,j}(\mathbf{r}) = \phi_j(\mathbf{r}), \qquad E_{S,j} = \varepsilon_j . \tag{2.162}$$

One important remark at this point is that the Kohn-Sham eigenstates are just auxiliary functions and do not have physical meaning. However, these KS work and are widely used [21].

2.9 Vibrations of periodic crystals: phonons

2.9.1 Initial considerations

To understand this section I follow the heuristic approach presented by Giustino [21]. This implies that first I will explain some important concepts and then write some generalizations. Good knowledge about solid state physics is expected.

As a starting point let us consider that the vibrations at the atomic level imply small variations in the positions of the nuclei. Hence, we can write the time-dependent position of each nucleus $\mathbf{R}_I(t)$:

$$\mathbf{R}_I(t) = \mathbf{R}_I^0 + \mathbf{u}_I(t) , \tag{2.163}$$

where $\mathbf{R}_I^0$ is the equilibrium position, and $\mathbf{u}_I(t)$ is the displacement. We can use the The Born-Oppenheimer (or adiabatic) approximation explained in section (2.2). Then, we are allowed to write the Newton's equations:

$$M_I \ddot{u}_I = -\frac{\partial U}{\partial u_I} , \tag{2.164}$$

where M_I are the atomic masses, U is the total energy, and

$$\ddot{u}_I = \frac{d^2 \mathbf{u}_I}{dt^2} . \tag{2.165}$$

Regarding the total energy, we can make a Taylor expansion in the atomic displacements $\mathbf{u}_I$ till second order:

$$U(\mathbf{R}_1, \ldots, \mathbf{R}_M) = U_0 + u_{I\alpha} \frac{\partial U}{\partial R_{I\alpha}} + \frac{1}{2} \frac{\partial^2 U}{\partial R_{I\alpha} \partial R_{J\beta}} u_{I\alpha} u_{J\beta} , \tag{2.166}$$

where $R_{I\alpha}$ denotes the I-th nucleus along the Cartesian direction α. U_0 is the total energy of the nuclei at their equilibrium positions. Notice that,

$$-\frac{\partial U}{\partial R_{I\alpha}} = M_I \frac{d^2 \mathbf{R}_I}{dt^2} = \mathbf{F}_I , \tag{2.167}$$

is the force acting on the I-th nucleus.

A really important term is the second partial derivatives of the total energies with respect to the coordinates of the nuclei, evaluated at the equilibrium positions[21]. These expressions are known as the Born-von Karman force constants K, and are defined as

$$K_{I\alpha,J\beta} = \frac{\partial^2 U}{\partial R_{I\alpha} \partial R_{J\beta}} \,. \tag{2.168}$$

Computationally, these types of expressions involving derivatives can be solved by finite-difference methods. Besides, note that U can be determined through DFT calculations.

Then, if we consider the equilibrium configuration of the system, the force for each nucleus will be zero, i.e., $\mathbf{F}_1 = \cdots = \mathbf{F}_M = 0$. Therefore, equation (2.166) becomes

$$U = U_0 + \frac{1}{2} K_{I\alpha,J\beta} u_{I\alpha} u_{J\beta} \,, \tag{2.169}$$

which is known as the **harmonic approximation**.

After some mathematics we can obtain the Newton's equations for the nuclei in the harmonic approximation[21]:

$$M_I \ddot{u}_{I\alpha} = -K_{I\alpha,J\beta} u_{J\beta} \,. \tag{2.170}$$

We can define the *mass-weighted displacements* $\upsilon_{I\alpha}$ as

$$\upsilon_{I\alpha} = M_I^{1/2} u_{I\alpha} \,. \tag{2.171}$$

Then, if we divide both sides of equation (2.170), then multiply the right hand side by $M_J^{1/2} M_J^{-1/2}$, and replace the definition (2.171) we obtain the equation of motion for the mass-weighted displacements:

$$\ddot{\upsilon}_{I\alpha} = -\frac{K_{I\alpha,J\alpha}}{(M_I M_J)^{1/2}} \upsilon_{J\beta} \,. \tag{2.172}$$

From here, we can define another important term know as the **dynamical matrix** $D_{I\alpha,J\beta}$:

$$D_{I\alpha,J\beta} = \frac{K_{I\alpha,J\beta}}{(M_I M_J)^{1/2}} \,. \tag{2.173}$$

Then, eqn. (2.172) becomes

$$\ddot{\upsilon}_{I\alpha} = -D_{I\alpha,J\beta} \upsilon_{J\beta} \,. \tag{2.174}$$

It is usual to use the symbol ν instead of $I\alpha$. This means that the labels for $I\alpha$ ($M1;M2;M3$) now will be represented by ν ($3M - 2; 3M - 1; 3M$) correspondingly. Notice that M holds for the number of nuclei and α for the Cartesian coordinates, then α can run till 3. In consequence, the dynamical matrix $D_{I\alpha,J\beta}$ has $3M \times 3M$ entries.

Equation (2.174) represents a coupled linear system of second-order differential equations, we can re-write them as

$$\frac{d^2 \mathbf{v}}{dt^2} = -\mathbb{D}\mathbf{v} \,, \tag{2.175}$$

where $\mathbf{v}$ is a three dimensional vector with components $\upsilon_{I\alpha}$. Then, we can proceed to diagonalize the dynamical matrix by means of

$$\det(\mathbb{D} - \omega^2 \mathbb{I}) = 0 \,. \tag{2.176}$$

By definition, $\mathbb{D}$ is a real and symmetric matrix[21]. As a consequence:

- $\mathbb{D}$ can be diagonalized by an orthogonal matrix $\mathbb{E}$. This means that $\mathbb{E}$ holds the condition $\mathbb{E}\mathbb{E}^T = \mathbb{I}$.

- The eigenvalues of $\mathbb{D}$ are real numbers.

From all these definitions, we note that the columns of $\mathbb{E}$ are named **mass-weighted normal modes of vibration**, or just vibrational eigenmodes. Usually, the corresponding eigenvalues are denoted as ω_ν^2, and their square roots ω_ν are known as **normal frequencies of vibration**[21]. Now, let us consider the matrix $\mathbb{Q}$ containing all the eigenvalues ω_ν. In this manner, we have an eigenvalue problem, this is

$$\mathbb{D}\mathbb{E} = \mathbb{E}\mathbb{Q}^2 . \tag{2.177}$$

If we replace this expression into eqn. (2.175), and multiply by $\mathbb{E}^T$ at both sides, we get

$$\frac{d^2}{dt^2}(\mathbb{E}^T \mathbf{v}) = -\mathbb{Q}^2(\mathbb{E}^T \mathbf{v}) . \tag{2.178}$$

Defining $\mathbf{w} = \mathbb{E}^T \mathbf{v}$, we can write

$$\ddot{w} = -\mathbb{Q}\mathbf{w} \tag{2.179}$$

or

$$\ddot{w}_\nu = -(\omega_\nu^2)w_\nu , \tag{2.180}$$

where $\nu = 1, \ldots, 3M$.

From here, the solution $u_{I\alpha}(t)$ to each differential equation can be written as the sum of sines and cosines:

$$u_{I\alpha}(t) = M_I^{-1/2} \sum_\nu E_\nu [A_\nu \cos(\omega_\nu t) + B_\nu \sin(\omega_\nu t)] , \tag{2.181}$$

where A_ν and B_ν are constants to be determined by initial conditions, and E_ν represents the matrix elements of $\mathbb{E}$. Till here, all these considerations will give a good insight about more general results in crystalline systems.

2.9.2 Generalizations

To obtain more general results, we have to apply the previous framework to a system that is periodic. Then, the nuclear positions $\mathbf{R}_I$ are written as[21]:

$$\mathbf{R}_I = \mathbf{R}_l + \tau_s , \tag{2.182}$$

where $\mathbf{R}_l$ represents a unit cell of the crystal [‡‡‡]. τ_s is the position of the nucleus within the unit cell. Now, we can re-label I by means of $I = (l, s)$ and $J = (l', s')$. Then, the Born-von Karman force constants can be written as

$$K_{ls\alpha,l's'\beta} = \frac{\partial^2 U}{\partial(R_{l\alpha} + \tau_{s\alpha})\partial(R_{l'\beta} + \tau_{s'\beta})} . \tag{2.183}$$

Then, the equation of motion is

$$M_s \ddot{u}_{ls\alpha} = -K_{ls\alpha,l's'\beta} u_{l's'\beta} , \tag{2.184}$$

[‡‡‡]Notice that $\mathbf{R}_l$ is a Bravais lattice vector described in section 2.7.1

where $u_{l's'\beta}(t)$ is the instantaneous displacement of an atoms s in unit cell l along the Cartesian direction α[21]. A general expression for propagating waves is given by

$$u_{ls\alpha}(t) = u_{s\alpha}^0 e^{i[\mathbf{q}\cdot(\mathbf{R}_l+\tau_s)-\omega t]}\,,\tag{2.185}$$

where $u_{s\alpha}^0$ is a constant.

If we use the previous equation, replace it into the equation of motion (2.184), and as done exactly in the previous section, i.e., defining

$$\upsilon_{s\alpha}^0 = M_s^{1/2} u_{s\alpha}^0\tag{2.186}$$

and the **dynamical matrix for lattice vibrations**

$$D_{s\alpha,s'\beta}(\mathbf{q}) = \frac{1}{(M_s M_{s'})^{1/2}} \sum_l e^{i\mathbf{q}\cdot\mathbf{R}_l} e^{i\mathbf{q}\cdot(\tau_{s'}-\tau_s)} K_{0s\alpha,ls'\beta}\,,\tag{2.187}$$

we get:

$$\sum_{s',\beta} D_{s\alpha,s'\beta}(\mathbf{q})\upsilon_{s'\beta}^0 = \omega^2 \upsilon_{s\alpha}^0\,,\tag{2.188}$$

where ω represents the phonon frequency, and $\upsilon_{s\alpha}^0$ is known as the polarization vector of the phonon mode.

Notice that in relation to the initial approach in the previous section (2.9.1) we have the dependence of the dynamical matrix on the wave vector $\mathbf{q}$ and the presence of an exponential factor. However, we have to deal again with an eigenvalue problem. Remember that the dynamical matrix is a $3n \times 3n$ (n being the number of atoms in the unit cell) Hermitian matrix and hence its eigenvalues ω^2 are real[73].

Therefore, when performing DFT calculations and aiming to study vibrations we have to evaluate the dynamical matrix. This can be done by density functional perturbation theory; or the other way (which we consider in this thesis) is by computing the matrix of force constants (2.183), then via a Fourier transform according to eqn. (2.187) obtain the dynamical matrix. Hence, the box considered for simulating the system must be large so that we accommodate the wavelength $\lambda = 2\pi/|\mathbf{q}|$, so we use a supercell with various unit cells[21].

Furthermore, the general solution $u_{ls\alpha}$ is given by

$$u_{ls\alpha} = M_s^{-1/2} \sum_\nu \int_{BZ} d\mathbf{q}\, E_{s\alpha,\nu}(\mathbf{q}) e^{i\mathbf{q}\cdot(\mathbf{R}_l+\tau_s)} [A_{s\alpha}(\mathbf{q}) e^{-i\omega_{\mathbf{q}\nu}t} + B_{s\alpha}(\mathbf{q}) e^{i\omega_{\mathbf{q}\nu}t}]\,.\tag{2.189}$$

Notice this equation has the same structure as eqn. (2.181), then the constants $A_{s\alpha}$ and $B_{s\alpha}$ may be determined by initial conditions, and $E_{s\alpha,\nu}$ represents the matrix elements of $\mathbb{E}$ defined previously.

With the previous results we are able to compute the phonon band structure which yields results that can be compared with experiments such as neutron or X-ray scattering[73]. Furthermore, we can compute the phonon density of states, defined as[73]

$$g(\omega) = \frac{1}{N} \sum_{n\mathbf{q}} \delta(\omega - \omega_{n\mathbf{q}})\,,\tag{2.190}$$

where N is the number of unit cells in the crystal and n is the band index.

Besides, we can determine the specific phonon DOS projected along a unit direction vector $\hat{\mathbf{n}}$ [73]. This is written as

$$g_k(\omega, \hat{\mathbf{n}}) = \frac{1}{N} \sum_{n\mathbf{q}} \delta(\omega - \omega_{n\mathbf{q}}) |\hat{\mathbf{n}} \cdot \upsilon_{n\mathbf{q}}^{s\alpha}|^2 \, . \tag{2.191}$$
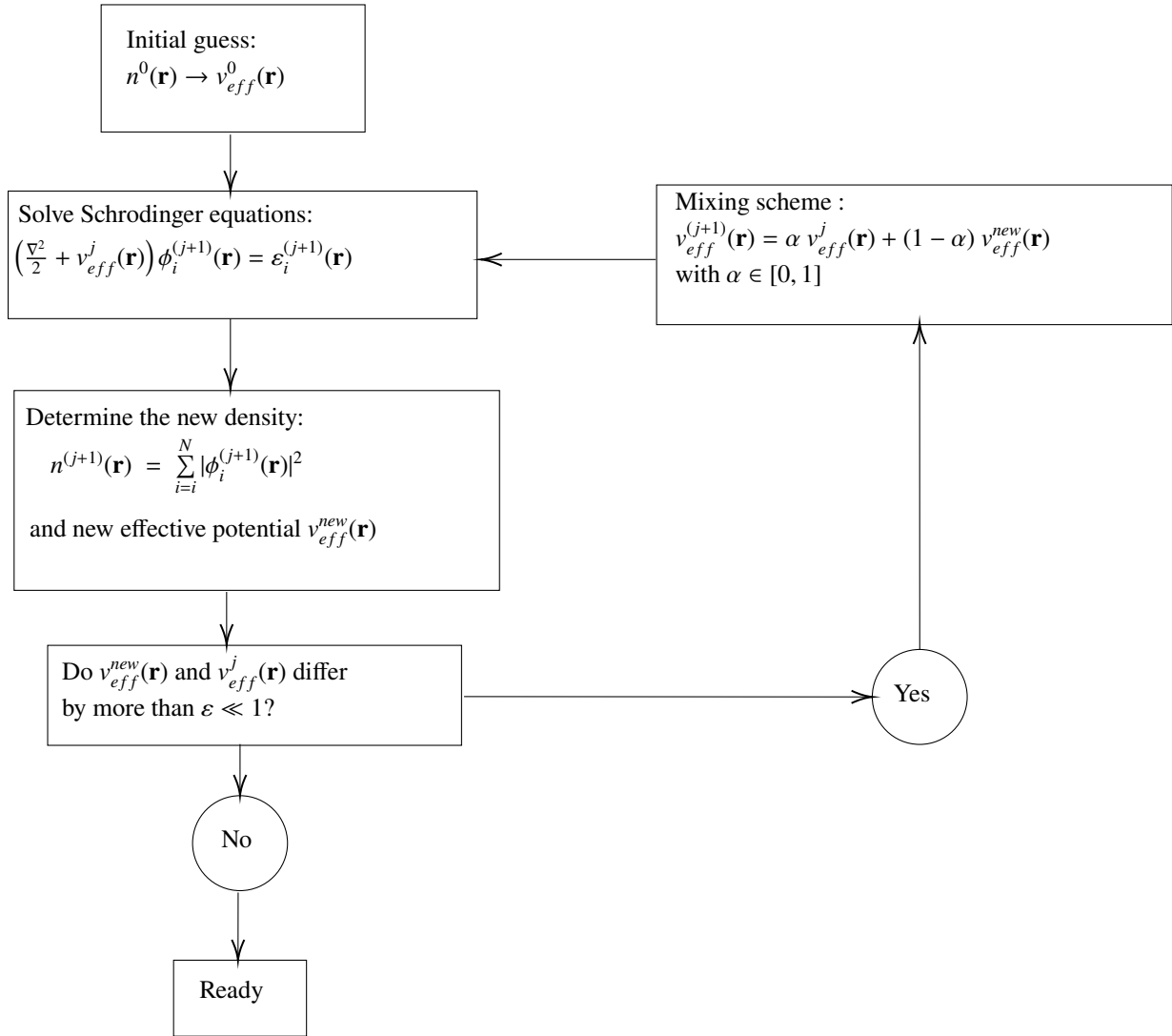
Figure 2.1: Flow chart diagram (adapted from ref.[23]) of a self-consistent cycle to solve the Kohn-Sham equations. We defined $v_{eff}(\mathbf{r}) = V_{ext}(\mathbf{r}) + V_H(\mathbf{r}) + V_{XC}(\mathbf{r})$. This diagram can also be used for solving the Hartree and Hartree-Fock equations. In general, we use an initial guess of the solution, and make various iterations that yield a new density and a new effective potential. This is performed till the difference of the new result and the previous one is in terms of a certain reasonable tolerance ε. Remember that it is equivalent to consider the convergence either of the potential $v_{eff}(\mathbf{r})$ or the density $n(\mathbf{r})$[28].

Notice that the step involving the mixing scheme is really important for achieving convergence in complex DFT calculations. This scheme is aimed to damp oscillations of $v_{eff}(\mathbf{r})$ when performing various iterations. The formula presented here shows the most simple mixing scheme in which we assume a linear combination of the initial $v_{eff}^j(\mathbf{r})$ plus the new $v_{eff}^{new}(\mathbf{r})$ to yield $v_{eff}^{j+1}(\mathbf{r})$, so that it can enters in a new cycle.

When dealing with meta-GGAs, e.g. SCAN, we have to take into account the kinetic energy density and hence a mixing scheme is necessary so that our calculations are able to converge. There are two main types of mixing schemes: the Broyden[29] and the Pulay[30] approaches. If we work with VASP, it has already implemented both schemes[28,31]. Actually, in VASP there is even the possibility for performing a *preconditioning* process before entering into the main self-consistency cycle, so that the computations converge without difficulty[32].
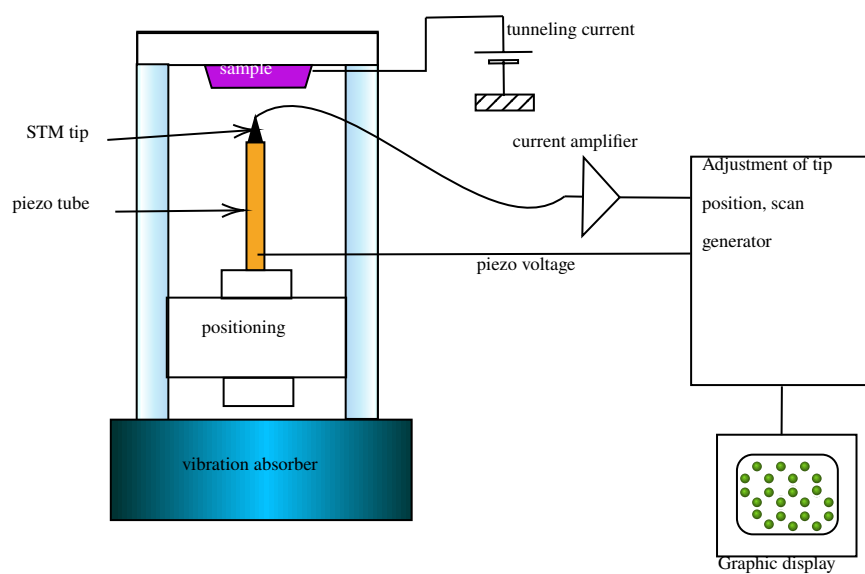
Figure 2.2: Adapted from Ref. [71]. Setup of a scanning tunneling microscope (STM). The tip is mounted on a piezotube, which is deformed by applied electric fields. This deformation translates into lateral and vertical manipulation of the tip. Via an electronic feedback loop, the position of the tip is adjusted according to the tunneling current (constant-current mode), and a two-dimensional current contour is recorded. This contour encodes all the information about the measurement. Courtesy of M. Schmid (Schmid, 1998).

Chapter 3

Methodology

The calculations were performed using the plane wave Vienna *ab initio* simulation package (VASP)[74]. Core electrons were described with projector augmented wave (PAW) potentials, where the potential for the Nb atoms was generated in the electron configuration $[Kr]4d^45s^1$, Li in $[He]2s^1$ and S in $[Ne]3s^23p^4$, where square brackets denote the core electron configurations. Then, following the systematic procedure provided at the end of section (2.7.6): A kinetic cutoff energy of 600 eV was adopted to expand the wave functions in a basis set of plane waves in combination with a **k**-point mesh with separation of 0.025 Å^{-1} to converge the total energy to < 1 meV/f.u. (f.u.=formula unit). Next, all the structures were fully relaxed until the forces in each atom is < 0.01 eV Å^{-1}.

In addition, as the NbS_2 and $LiNbS_2$ compounds are layered materials then van der Waals interactions have to be considered properly; for this reason, the SCAN+rVV10 functional of Peng et al.[42] that included the vdW dispersions was considered. Furthermore, computations with the hybrids Heyd-Scuseria-Ernzerhof (HSE) were performed. Various *flavors* of HSE were considered: HSE06, HSE12, and HSE12s. Refer to section (2.6.3.7) for specific details about the hybrids, and to section (2.6.3.4) for more about SCAN and SCAN+rVV10. It is important to stress here that we did not use HSE06+GW due to the size of the systems considered here as the computational requirements surpassed our available computational power.

After the convergence of the cut-off energy and **k**-points, we fitted the energies to Birch-Murnaghan equation (see section (2.7.7)) and found the minimum of the function $E(V)$. With this information we were able to compute the bulk modulus and the lattice parameters. Then, we were able to compute various surface systems according to the slab model. The STM images were computed using Tersoff-Hamann approximation as implemented in the bSKAN software[75,76].

Furthermore, for computing the phonon band structure we setup a calculation as implemented in Phonopy software. We set a supercell of $2 \times 2 \times 1$ and calculated the forces with the SCAN+rVV10 functional. The path of the wave vectors was determined with the Materials Studio software. For plotting the band structure we used the software *sumo*, created by Ganose, Jackson, and Scanlon[77].

3.1   VASP details

Following what was explained in section 2.7, here we describe the files needed for running VASP, and its respective
outputs.

3.1.1   VASP inputs

To run VASP we need to prepare carefully the next input files: INCAR, POSCAR, KPOINTS, POTCAR.

3.1.1.1   INCAR

The INCAR file provides the information about several parameters that indicate the program "what to do and how
to do it"[78]. INCAR can have as an input a myriad of parameters which describe the routines that are going to be
used such as the cutoff energy, the tag of the exchange-correlation energy functional, some tags of corrections, and
so on. Sometimes when we do not set a certain tag (e.g., the cutoff energy), VASP has the *missing* information in
the POTCAR file, however one has to be very careful with every tag that is left as default by VASP. See an example
in Fig. (3.1).

```
SYSTEM = linbs2 !this is the name of the system we study
#%%%%%%%%%% ELECTRONIC RX %%%%%%%%%%%%%%%%%%%%%%%%%%%%%%%
ISMEAR = 0 ; SIGMA = 0.01 ! -5 insulators & final energy 1 rx in metals
LREAL = auto
PREC = Accurate
ENCUT = 600
LORBIT = 11 ! use this for PDOS
NEDOS = 3001
EMIN=-20
EMAX=12
#%%%%%%%%%% FUNCTIONAL %%%%%%%%%%%%%%%%%%%%%%%%%%%%%%%%%%%
METAGGA = SCAN
LMIXTAU = T
LASPH = T !use for LDA+U, hybrid or meta-GGA in f- and 3d-elements
#%%%%%%%%%% DIPOLE CORRECTIONS %%%%%%%%%%%%%%%%%%%%%%%%%%
#IDIPOL=3 ! 3 is for surfaces
#LDIPOL= T
```

Figure 3.1: INCAR example file. The tags are always in capital, the comments are followed by the symbols # and !.
For the meaning of each tag it is advisable to see the VASP documentation in `https://www.vasp.at/wiki/`
`index.php/The_VASP_Manual`.

3.1.1.2   POSCAR

POSCAR contains the lattice geometry and the ionic positions[79]. In Figure (3.2) I present an example.

3.1.1.3   KPOINTS

In all the calculations of this thesis, we only use the Monkhorst-Pack method, which is implemented in VASP and is the most used in calculations[48]. Hence, we supply the number of **k**-points subdivisions N_1, N_2, and N_3. The file for **k**-points has to be stated as in Fig. (3.3).

3.1.1.4   POTCAR

The POTCAR file contains the pseudopotential for each atomic species used in the calculation[80], number of valence electrons, atomic mass, and so on. If there are several atoms, we have to concatenate all the POTCARs corresponding to each element into one POTCAR. VASP owners have the ability to provide, modify, and create the POTCAR files, therefore it is not possible to show one example of this type of files. In the case of $LiNbS_2$ we can make the POTCAR file in this form[80]:

```
username:~$ cat ~/pot/Nb/POTCAR ~/pot/S/POTCAR ~/pot/Li/POTCAR >POTCAR
```

where *pot* is the name of the folder containing all the POTCAR files, and *cat* is the command for concatenate in a Unix system. A very important remark is that **the order that we concatenate the files must remain in the POSCAR file too**.

When dealing with the **SCAN** functional, **it is very important that the POTCAR files we choose include information about the kinetic energy density of the core-electrons**. To check this condition, we must do this[81]:

```
username:~$ grep kinetic POTCAR
```

The result of the previous command have to yield the following lines:

```
kinetic energy-density
mkinetic energy-density pseudized
```

and for PAW datasets with partial core corrections, another line appears too:

```
kinetic energy density (partial)
```

These lines appear for every atom, this means that for $LiNbS_2$ POTCAR we should have the previous lines repeated three times.

```
1  Nb S Li :  sym194
2    0.991893950738816
3       3.3841795743891363   -0.0000000000000009   -0.0000000000000000
4      -1.6920897871945662    2.9307854823893997    0.0000000000000000
5      -0.0000000000000000    0.0000000000000000   12.9422483576345666
6      Nb    S    Li
7       2     4     2
8  Selective dynamics
9  Direct
10  -0.0000000000000000 -0.0000000000000000  0.2500000000000000   T   T   T
11   0.0000000000000000  0.0000000000000000  0.7500000000000000   T   T   T
12   0.3333330000000032  0.6666669999999968  0.1275256213968238   T   T   T
13   0.3333330000000032  0.6666669999999968  0.3724743786031759   T   T   T
14   0.6666669999999968  0.3333330000000032  0.6275256213968240   T   T   T
15   0.6666669999999968  0.3333330000000032  0.8724743786031760   T   T   T
16  -0.0000000000000000 -0.0000000000000000  0.0000000000000000   T   T   T
17  -0.0000000000000000 -0.0000000000000000  0.5000000000000000   T   T   T
```

Figure 3.2: POSCAR example file for the bulk $LiNbS_2$ system. For more details it is advisable to see the VASP documentation in `https://www.vasp.at/wiki/index.php/The_VASP_Manual`. Exactly as stated in the VASP documentation[79]: The first line is treated as a comment line (you should write down the name of the system). The second line provides a universal scaling factor (lattice constant), which is used to scale all lattice vectors and all atomic coordinates. On the following three lines the three lattice vectors defining the unit cell of the system are given (first line corresponding to the first lattice vector, second to the second, and third to the third). The sixth line specifies the constituting elements (**in the order how they appear in the POTCAR file**). The seventh line supplies the number of atoms per atomic species. The eighth line switches to selective dynamics (only the first character is relevant and must be S or s). The ninth line is the type of coordinates we are working with: either Cartesian or Direct. Furthermore, we can provide extra flags for each atom signaling whether the respective coordinate(s) of this atom will be allowed to change during the ionic relaxation. This setting is useful if only certain shells around a defect or layers near a surface should relax. Hence for each coordinate we can set either T (holding for True) or F (holding for False). True means that we allow the coordinate to move, whereas False means the coordinate is fixed or constrained.

```
1  kpoints LiNbS2, dk=0.025 1/Ang
2  0                      ! number of k-points = 0 -> automatic generation
      scheme
3  Gamma            ! generate a Gamma centered grid
4   14 14 3          ! subdivisions N_1, N_2 and N_3 along recipr. latt. vectors
5   0 0 0            ! optional shift of the mesh (s_1, s_2, s_3)
```

Figure 3.3: KPOINTS example file for the bulk LiNbS$_2$ system. For more details it is advisable to see the VASP documentation in `https://www.vasp.at/wiki/index.php/The_VASP_Manual`. The first line is just a comment.

3.1.2 VASP outputs

There is a myriad of outputs that VASP yields, nevertheless the most important are:

3.1.2.1 CONTCAR

This file has the same structure as the POSCAR file. The difference is that CONTCAR provides the updated geometry of a calculation.

3.1.2.2 OUTCAR

The OUTCAR file yields detailed information about the performed calculations such as: a summary of the input parameters, forces on the atoms, local charges and magnetic moments, timing of computations, etc.

3.1.2.3 OSZICAR

This file provides a summary of all the results such as the convergence of the total energy, free energies, etc.[82].

3.1.2.4 DOSCAR

DOSCAR contains the total and integrated density of states (DOS) and optionally the local partial DOS (PDOS)[82].

3.1.2.5 WAVECAR

This file stores the wave function coefficients in binary form. This is a very heavy file, it could represent a few gigabytes of storing.

3.2   Computational implementation of Bardeen theory: bSKAN 3.6 software

To computationally produce STM images it is possible to use VASP itself, it is just a matter of modifying the INCAR file with the accurate parameters, nevertheless, bSKAN * (created by W. A. Hofer[76]) is a software that allows to perform STM calculations with input files that follow the VASP format. It is implemented to work in parallel with big computational architectures. Besides, bSKAN considers the Bardeen theory and we can modify the inputs so that we use for instance the Tersoff-Hamann approach.

3.2.1   bSKAN inputs

bSKAN works in accordance with VASP, hence we need the following files:

- WAVECAR, an output of VASP.

- ASAMPLE, the same file as the CONTCAR. We just have to copy the CONTCAR file into ASAMPLE.

- INCAR, the one we used for the VASP calculations but adding the following line of figure (3.4):

```
1          #%%%%%%%%%% For STM   %%%%%%%%%%%%%%%%%%%%%%%%%%%%%%%%%%%%
2          STM = \$zval \$zval2 0.052918 -60 \$evalmin \$evalmax \$Fermi level
3
```

Figure 3.4: Line to be added to the original INCAR file.

- INSCAN, which gives technical details about the STM simulations such as the number of grid points and the bias voltage. An example is shown in Fig. (3.5).

- STM file, which possesses the information of the unit cell we are studying, such as the **k**-points and **G** vectors. This file is generated automatically after invoking bSAKAN in a program with all the inputs.

3.2.2   bSKAN outputs

bSKAN software yields various output files regarding the information of the calculation just performed. The most important output files are:

- OUTSCAN, following the purpose of OUTCAR with important information about the STM simulation.

---

*To understand well the program bSKAN it is recommended to read the documentation[76] and Ref.[75]

```
 1  #STM simulation for linbs2 (001) 2x2
 2  TERSOFF
 3  # NUMERICAL
 4  LIMITS = -0.05  0.05
 5  GRIDPOINTS = 70
 6  BIAS VOLTAGE = 1.5
 7  # CELL = 1.0 1.0
 8  NKELDYSH = 1
 9  PIVOT = 0.0000  0.0000    ! pivot (lower left corner) point
10  TOP = 0.0000  0.0000
11  ZVACUUM = 45.456099999999999
12  CURRENT = 0.0
```

Figure 3.5: INSCAN file example.

- CURRENT. This file is a set of a 3D grid mesh resulting from the simulation. There are points that simulate the actual STM tomography in the x, y, and z direction. To plot this grid of points is a challenge, one should aim to interpolate a function in 3D that will allow to plot the STM simulation.

3.3 Implementation for computing phonons: Phonopy

Phonopy is an open source program created by Atsushi Togo[73] that is suited to compute vibrations, and also allows to work along with the outputs of various DFT programs, i.e., it is possible to work in accordance with VASP. A part of Phonopy implementation follows the theory just described in the previous section. It is recommended to review its theoretical documentation at https://phonopy.github.io/phonopy/formulation.html#second-order-force-constants.

Then, in this thesis we follow what is described in the Phonopy documentation as VASP & phonopy calculation, available at https://phonopy.github.io/phonopy/vasp.html#vasp-interface.

The first requirement for the program to work is a POSCAR file. Nevertheless, we have to consider a file that provides the updated geometry of a calculation, i.e, we have to work with the CONTCAR file. This means that we have to copy a CONTCAR into a POSCAR so that Phonopy can read the file:

```
username:~$ cp CONTCAR POSCAR
```

Then, we need to create supercells of our system (following what was explained at the end of sec. (2.9)). For instance, we can create $(2 \times 2 \times 1)$ supercells with the next command:

```
username:~$ phonopy -d --dim="2 2 1"
```

After the execution of the previous command we obtain as output the next files:

- POSCAR-00i, where i runs from 1 to 4, i.e., we have 4 POSCARs now. These files are different with slight changes in the coordinates.

- SPOSCAR, which has the same structure as a standard POSCAR.

- 'phonopy_disp.yaml' file, which indicates detailed information about the supercells just created.

More specifically, as stated in Phonpy documentation: SPOSCAR is the perfect supercell structure, 'phonopy_disp.yaml' contains the information on displacements, and 'POSCAR-{number}' are the supercells with atomic displacements. 'POSCAR-{number}' corresponds to the different atomic displacements written in 'phonopy_disp.yaml'.

Then, we have to calculate the sets of forces with VASP, hence we need to prepare a special INCAR as shown in fig. (3.6). The main objective is to generate the files named 'vasprun.xml'. Notice that in the local directory we are working on, we need to create a different folder for each 'POSCAR-{number}' that will produce a particular 'vasprun.xml'. Following the notation on Phonopy documentation, the folders containing the 'vasprun.xml' files are named 'disp-{number}'.

Till this part we have completed the so-called pre-process in Phonopy calculations. Then, in the post-process:

1. Force constants are calculated from the sets of forces.

2. A part of dynamical matrix is built from the force constants.

3. Phonon frequencies and eigenvectors are calculated from the dynamical matrices with the specified q-points.

Once we have have the folders 'disp-{number}' with their respective 'vasprun.xml', we can type the command shown in fig. (3.7).

Then, we need to create the appropriate files according to the calculation we need Phonopy to perform. For isntance, by setting a file named 'mesh.conf' we can then obtain the density of states (DOS) and thermal properties. By setting the file 'band.conf' (Fig.(3.8)) we can then obtain the band structure of our system (this is the frequency vs. the wave vectors of the BZ). Also, by creating the file 'pdos.conf' (Fig.(3.9)) we can obtain the projected density of states.

Once created the needed files, we can then proceed to execute the calculations and obtain the plots. If we want to compute the band structure, then we type the command of fig. (3.10).

Notice that Phonopy yields the plot in Python format by default. If we want to make our own plot of the band structure, the file 'band.yaml' is produced (after the execution of the command of fig. (3.10)) so that we can handle it.

We can also compute the projected density of states with the command shown in fig. (3.11). Again, Phonopy will produce a plot, but if we want to deal with the graph by ourselves we can see that the file 'projected_dos.dat' is yielded after executing the command aforementioned.

```
 1  SYSTEM = linbs2
 2  ISMEAR=0 ; SIGMA=0.01 ! use this for accurate DOS insulators
 3  LREAL = F
 4  PREC = Accurate
 5  ENCUT = 600
 6  EDIFF = 1E-08
 7  NGX= 82 !multiple 1.5*standard
 8  NGY= 82 !multiple 1.5*standard
 9  NGZ= 108
10  ALGO = N !N more accurate
11  LMAXMIX=4
12  LCHARG= F
13  #%%%%%%%%%%% FUNCTIONAL %%%%%%%%%%%%%%%%%%%%%%%%%%%%%%%%%%
14  METAGGA  = SCAN
15  LUSE_VDW = .TRUE.
16  BPARAM = 15.7
17  LMIXTAU = T
18  LASPH = T !use for LDA+U, hybrid or meta-GGA in f- and 3d-elements
19  #%%%%%%%%%%% PARALLELISATION STAMPEDE %%%%%%%%%%%%%%%%%%%%%%%%
20  NCORE=24 ! this is total cores per node
21  NSIM=4 ! use 1 in supercomputers
22  KPAR=4
```

Figure 3.6: INCAR file working with Phonopy. Here is also shown the tags that invoke the functional SCAN+rVV10.

```
username:~$
    phonopy -f disp-001/vasprun.xml disp-002/vasprun.xml disp-003/vasprun.xml
```

Figure 3.7: Phonopy command for calculating the sets of forces. This is written in the file 'FORCE_SETS'.

```
1  ATOM_NAME = Nb S Li
2  DIM = 2 2 1
3  BAND= 0 0 0 0 0 1/2 -1/3 2/3 1/2 -1/3 2/3 0 0 0 0 0 1/2 0 0 1/2 1/2 -1/3 2/3
       1/2
4  BAND_LABELS =  $\Gamma$ A H K $\Gamma$ M L H
5  FC_SYMMETRY = .TRUE.
6  #FORCE_CONSTANTS = READ
```

Figure 3.8: 'band.conf' file for LiNbS$_2$.

```
1  ATOM_NAME = Nb S Li
2  DIM = 2 2 1
3  MP = 15 15 15
4  PDOS = 1 2, 3 4 5 6, 7 8
5  #PDOS = AUTO
6  GAMMA_CENTER = .TRUE.
7  FC_SYMMETRY = .TRUE.
8  #FORCE_CONSTANTS = READ
```

Figure 3.9: 'pdos.conf' file for LiNbS$_2$.

```
username:~$ phonopy -p band.conf
```

Figure 3.10: Phonopy command for calculating the band structure.

```
username:~$ phonopy -p pdos.conf
```

Figure 3.11: Phonopy command for calculating the projected density of states (PDOS).

Chapter 4

Results & Discussion

4.1 Bulk Niobium Sulfide NbS$_2$

The first system we studied is the NbS$_2$ as shown in fig. (4.1); in the following section we present the DFT simulations of this crystal. The NbS$_2$ has a S-Nb-S layered structure with an hexagonal arrangement along the plane.
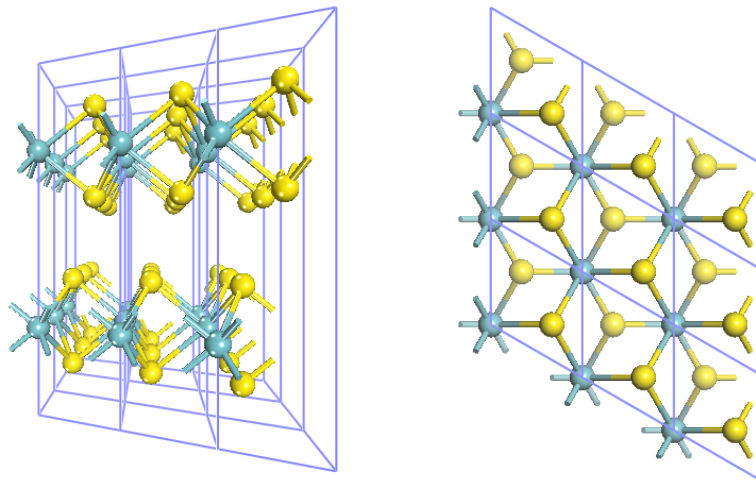
Figure 4.1: Atomic structure of NbS$_2$. The atoms in yellow (blue) are sulfur (niobium) atoms. On the left, side perspective view of NbS$_2$. On the right, top view of NbS$_2$, it has a honeycomb-like shape; the faded atoms are lower than the clear ones. The blue line delimits the unit cell.

We started the calculations computing the convergence of the cut-off energy (fig. (4.2)) and the **k**-points (fig. (4.3)). After that we obtained the fit for NbS$_2$ data using the Birch-Murnaghan equation of state (fig. (4.4)).
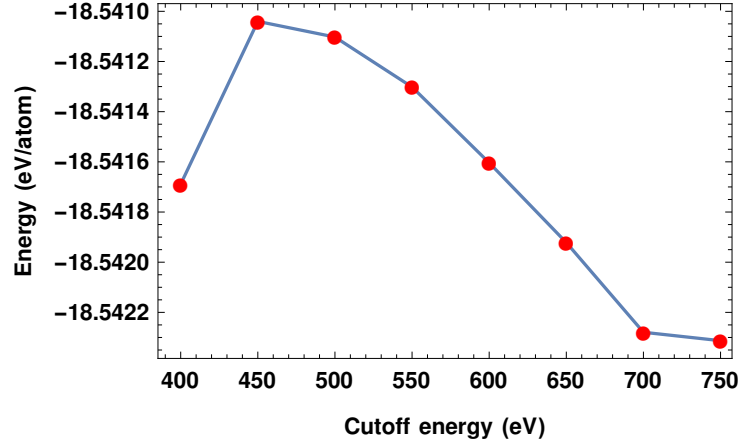
Figure 4.2: Cut-off energy convergence for bulk NbS$_2$. Here the energies start to converge to less than 1 meV/f.u. from 500 eV, hence I choose 600 eV for the calculations.
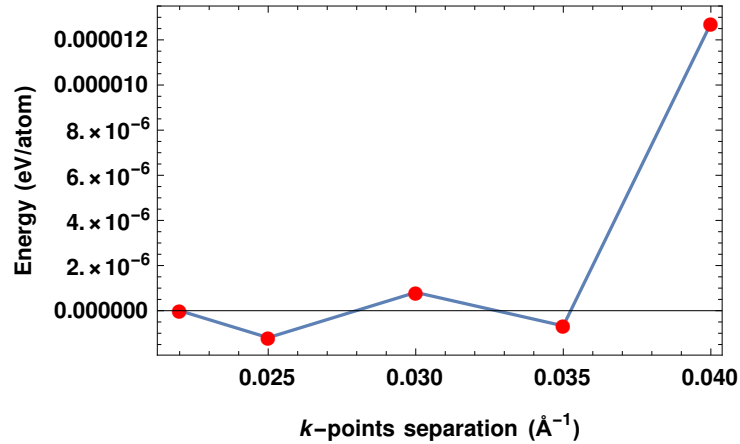
Figure 4.3: **k**-points separation length convergence for bulk NbS$_2$. Notice the en energy E is inside a range much less than 1 meV/atom. Therefore, we chose 0.025 Å^{-1} of separation length, which corresponds to the set of **k**-points $14 \times 14 \times 3$.

The SCAN + rVV10 computed optimal crystallographic parameters are listed in Table 4.1 and compared with experimental values.

Considering the previously SCAN+rVV10 structure, we computed the Partial Density of States (PDOS) showing that NbS$_2$ is metallic. The results given by the SCAN+rVV10 functional are similar to the ones yielded by HSE06. It can be seen in Fig. (4.5) and Fig. (4.6) the obtained PDOS performed by the SCAN+rVV10 and the HSE06 functionals, respectively. It is possible to notice that the lower valence band for the HSE06 is shifted lower in energy

Table 4.1: Computed SCAN+rVV10 crystallographic data for NbS$_2$, u, v, w are the fractional coordinates. Within parenthesis are the experimental values; in addition, the system is observed to be metallic in agreement with our calculations.

property		Calculated (SCAN+rVV10)	
Space group		$P6_3/mmc$	
$a = b$(Å)		3.334 (3.310)	
c(Å)		12.058 (11.890)	
$\alpha = \beta$(°)		90	
γ(°)		120	
Volume ($\overset{\circ}{A}^3$)		116.050 (112.815)	
B_0(GPa)		34.72	
sites	u	v	w
Nb(1)	0.0000	0.0000	0.7500
Nb(2)	0.0000	0.0000	0.2500
S(1)	0.6667	0.3333	0.6212
S(2)	0.3333	0.6667	0.3788
S(3)	0.3333	0.6667	0.1212
S(4)	0.6667	0.3333	0.8788
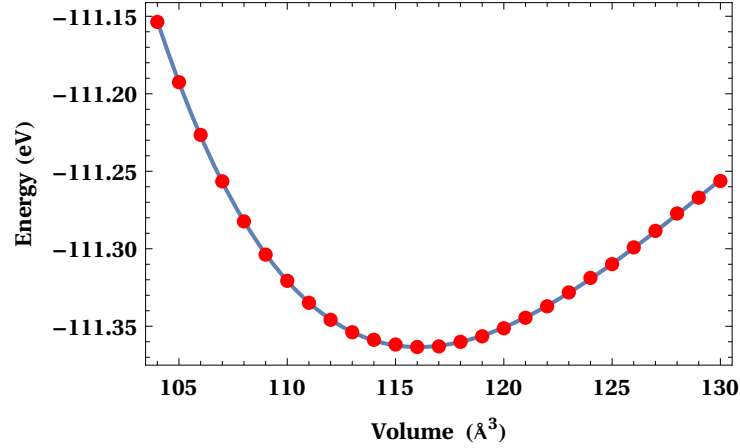
Figure 4.4: Fit of the Birch-Murnaghan equation of state for NbS$_2$.

in comparison to the SCAN+rVV10 calculation; nonetheless both electronic structures show basically the same features.

In the following lines we describe the electronic structure of NbS$_2$ as computed by HSE06. The lower valence band (LVB) located within the energy range -15.6 to -13.2 eV is basically composed by S-3s states with a minor contribution of Nb-4d states, this band shows a main peak at -13.2 eV. The band ranging from -6.8 eV to +1.9 eV has a mixture of S-3p and Nb-4d+5s states. The Fermi level cut this band where we observe a nearby peak at -0.2 eV; this has mainly a character of Nb-4d with minor contribution of S-3p states. Finally, the upper conduction band (UCB) ranging from 2.8 eV to 4.6 eV is formed by a mixture of Nb-4d and S-3p with two main peaks at 3.5 eV and 4.2 eV. All these results are in agreement with what has been observed experimentally and in other calculations [8,11,83–87]. For detailed information about the PDOS see the Appendix A, Fig. (A.1). In addition, the band structure of NbS$_2$ was also computed using the HSE06 functional as displayed in Fig. (4.7).

4.2 Bulk LiNbS$_2$

LiNbS$_2$ is the main study of this thesis, in the following sections I will describe the main results obtained for this material. The atomic structure of LiNbS$_2$ is presented in figure (4.8). Taking into account the previous structure of NbS$_2$, we can think about the idea of intercalated atoms in between the S-Nb-S layers. Then, if we intercalate lithium atoms, we can obtain LiNbS$_2$. First we computed the convergence of the cut-off energy (as in shown in figure (4.9)), the convergence of the **k**-points length separation (see figure (4.10)). Then we fitted the data to the Birch-Murnaghan equation of state for LiNbS$_2$, shown in fig (4.11). These calculations were performed with the SCAN+rVV10 functional.
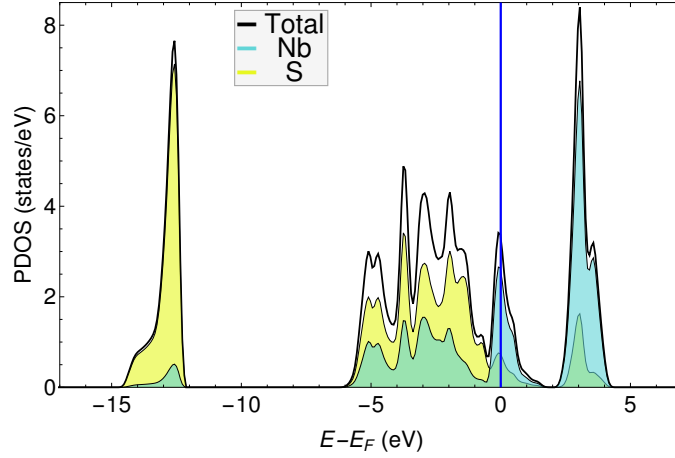
Figure 4.5: Partial density of states of bulk NbS_2 computed with SCAN+rVV10. The Fermi level is centered at 0 and represented with the blue line. Consider that the superposition of yellow and cyan colors produces an effect of light green color; this color effect is also in the PDOS figures in this thesis.
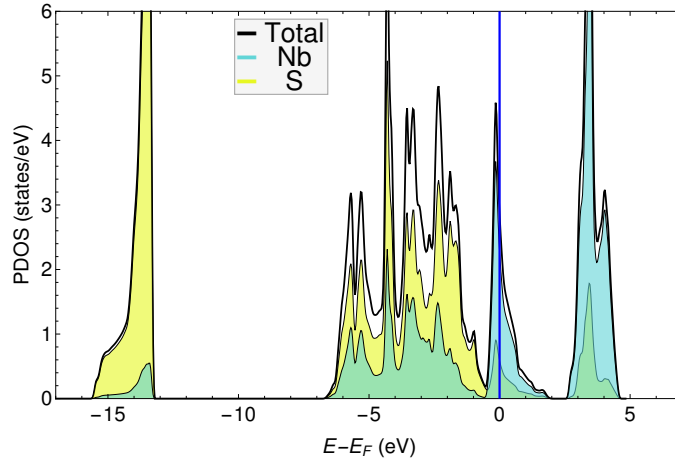

Figure 4.6: Partial density of states of bulk NbS_2 computed with HSE06. The Fermi level is centered at 0 and represented with the blue line.

4.2.1 Stability of various LiNbS$_2$ symmetries

There are various symmetries in which bulk LiNbS$_2$ could be arranged. We present the results of the calculations performed with SCAN + rVV10 for the symmetry groups $P6_3/mmc$ IT No. 194, $C2/m$ IT No. 12, $R\bar{3}m$ IT No. 166, and $Cmcm$ IT No. 63. This can be seen in Table (4.2) and it is noteworthy that the most stable configuration is $P6_3/mmc$ IT No. 194. Evidently, the $P6_3/mmc$ symmetry group is the most stable. Although the band gaps are not
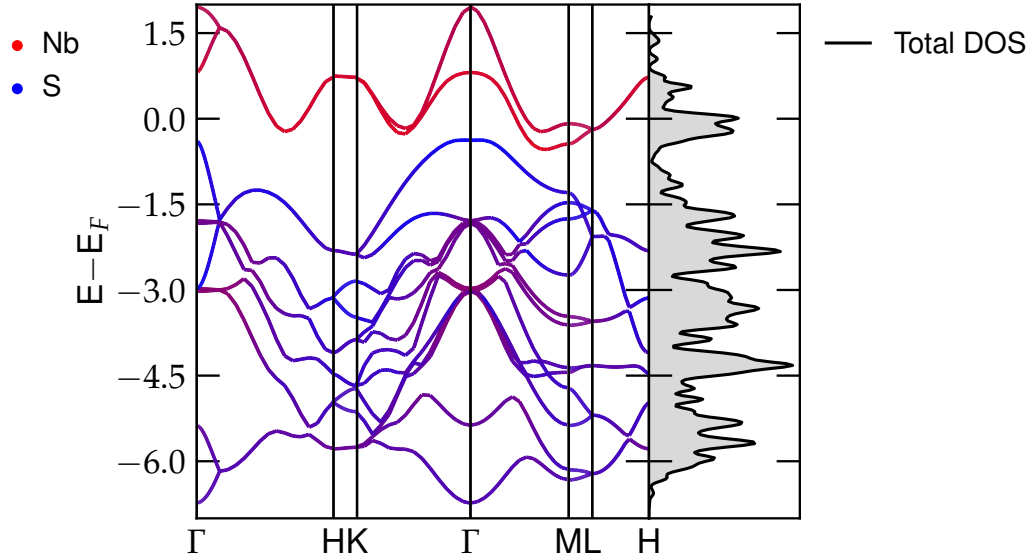
Figure 4.7: HSE06 computed band structure for the NbS$_2$ along the high symmetry points. Nb bands are plotted in red, whereas S bands are in blue. The system is metallic, i.e., there is no bandgap. The metallic character is due to the Nb-4d orbitals which produce a band that crosses several times the Fermi level within the BZ.
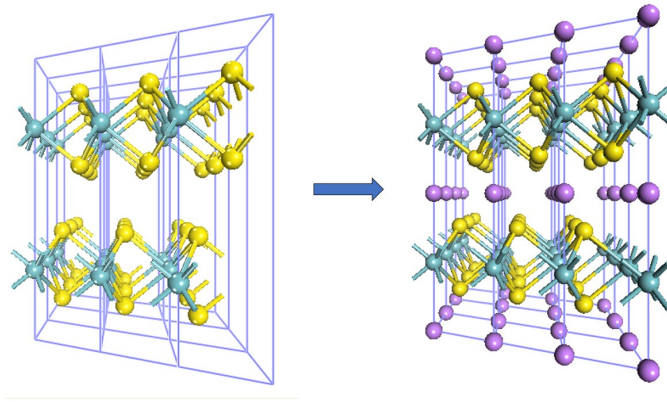
Figure 4.8: Bulk NbS$_2$ (on the left) goes through intercalation of Li atoms, producing the bulk LiNbS$_2$ atomic structure (on the right). The atoms in yellow (blue) are sulfur (niobium), and the ones in purple are lithium.

accurate, this analysis provide a clear understanding about stability.

In Table (4.2) is the detailed information about the lattice parameters for various symmetries of LiNbS$_2$. Also a figure of the unit cell with the angle γ is showed in Figure (4.12). Notice the subtle energetic change of the
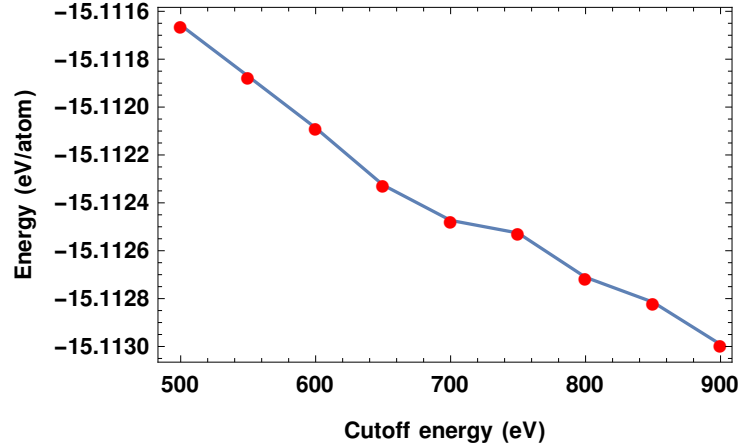
Figure 4.9: Cut-off energy convergence for bulk $LiNbS_2$. Here the energies start to converge at 600 eV, hence I choose 600 eV. Notice the energy E is inside a range less than 1 meV/f.u.
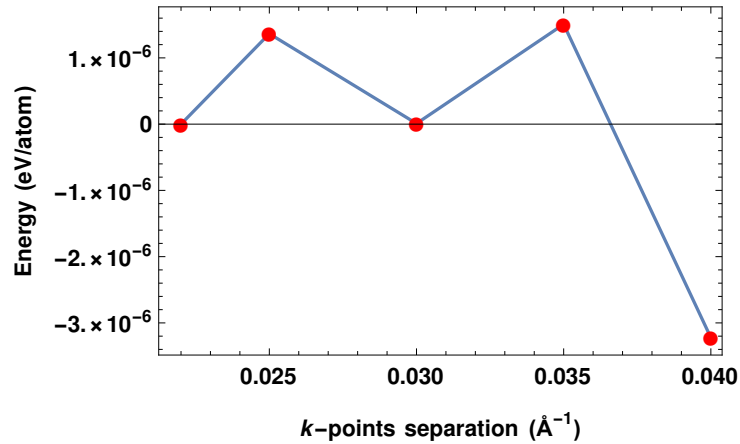
Figure 4.10: **k**-points separation length convergence for bulk $LiNbS_2$. Notice the energy E is inside a range much less than 1 meV/f.u. Therefore, we chose 0.025 Å^{-1} of separation length, which corresponds to the set of **k**-points $14 \times 14 \times 3$.

angle γ: the most stable structure is when $\gamma = 90°$, if $\gamma < 90°$ we obtain symmetry 63a, whereas if $\gamma > 90°$ we obtain symmetry 63b, which shows high energy. It is remarkable and interesting that just by a change of $\sim 0.001°$ in γ we obtain different symmetries. Changes in the angles α, β, and γ * are also reflected in changes on the internal coordinates of some atoms; what we found is that the most suitable parameter to understand these changes in symmetry for No. 194 and No. 63 are the angles.

*It is defined as: α, the angle between b and c; β the angle between a and c; and γ, the angle between a and b.
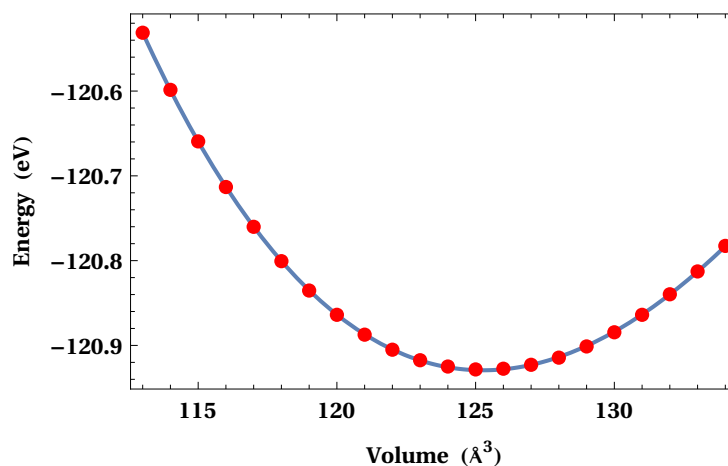
Figure 4.11: SCAN+*r*VV10 computed EOS using the Birch-Murnaghan for LiNbS$_2$ with symmetry *P*6$_3$/*mmc*.
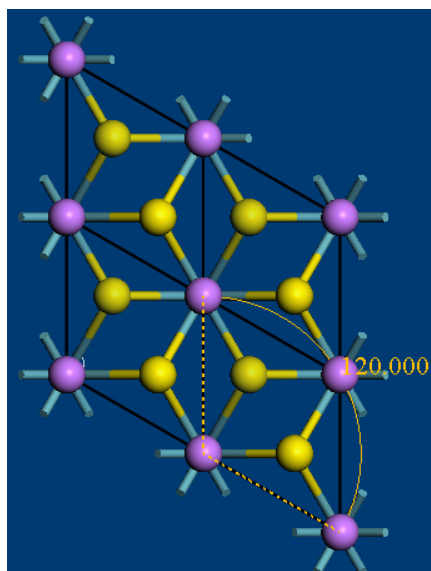
Figure 4.12: γ angle of the LiNbS$_2$ unit cell for the *P*6$_3$/*mmc* (194) symmetry, it is marked with dashed yellow lines (*a* and *b*), and with a continuous yellow line passing through 3 lithiums. A subtle change in this angle and we get a symmetry No. 63 as described in Table(4.2). The picture is an upper view of a 2x2 cell of LiNbS$_2$ where the black lines denotes the unit cell.

In Table (4.3) it is displayed the SCAN+*r*VV10 predicted crystallographic properties of the most stable system with symmetry *P*6$_3$/*mmc*.

Table 4.2: SCAN + rVV10 computed lattice parameters and energies of bulk $LiNbS_2$.

Symmetry Group	ΔE (meV/f.u.)	$\alpha = \beta(°)$	$\gamma(°)$	$a = b$(Å)	c(Å)	V_0 (Å^3)	B_0 (GPa)	E_g(eV)
$P6_3/mmc$ (194)	0.0	90	120	3.357	12.837	125.27	87.46	0.80
$Cmcm$ (63a)	0.1	90	119.998	3.7575	12.830	125.26	87.29	0.80
$C2/m$ (12)	137.0	104.514	59.988	3.357	13.431	125.45	86.73	0.82
$R\bar{3}m$ (166)	136.8	14.823	14.823	13.010	13.010	125.51	86.07	0.82
$Cmcm$ (63b)	278.0	90	120.008	3.357	12.880	125.70	85.60	0.89

4.2.2 PDOS calculations with SCAN+rVV10 and HSE

We also performed simulations using the SCAN+rVV10 and the HSE functionals to study the PDOS of $LiNbS_2$. We used the framework of HSE06[44], but also tried two variations of the HSE functional known as HSE12 and HSE12s[45]. Interestingly, the $LiNbS_2$ system has a band gap which has been observed experimentally to be 1.3 eV[16]. The most accurate value of band gap was provided by HSE12. We can see the summary of the results in table 4.4, the PDOS by SCAN + rVV10 (Fig. 4.13), HSE06 (Fig. 4.14) and HSE12 (Fig. 4.15).

The computed electronic structure of $LiNbS_2$ using the above mentioned functionals shows similar features except by the value of the band gap. In the following lines, we describe the electronic structure computed by HSE12 since it provides the best prediction of the band gap.

The lower valence band (LVB) located within the energy range -17.5 to -14.98 eV is mainly composed by S-3s states with a minor contribution of Nb-4d states, this band shows a main peak at -15.44 eV. The band ranging from -8.62 eV to -2.55 eV has a mixture of S-3p and Nb-4d states with a tiny contribution of Li-2s. Then, there is a band from -2.17 eV till the Fermi level that is formed principally by Nb. Notice there is a band gap of around 1.27 eV until the upper conduction band (UCB) which appears ranging from 1.27 to 3.4 eV that consists of Nb-4d, S-3p and a tiny contribution of Li-2s. Three peaks appear at around 2.16 eV, 2.56 eV, and 2.93 eV. The band gap that has been obtained is in accordance to experiment. Finally, the band structure for $LiNbS_2$ is shown in Fig. (4.16).

It is remarkable the presence of one peak around 2 eV. Niobium contributes with states due to the d orbitals ($d_{xy}, d_{yz}, d_{xz}, d_{x^2-y^2}, e_g, t_{2g}$), Sulfur add to the peak with the p orbitals (p_y, p_x), and Lithium with the p orbitals (p_y, p_z). For detailed information about the PDOS see the Appendix A, Fig. (A.2).

4.2.3 The $LiNbS_2$(001) surfaces

To study the $LiNbS_2$(001) surfaces we used the slab model. There are several possibilities of arrangements as the material could be ending either with lithium or sulfur. Furthermore, the positions of the superficial atoms could be in different positions and there could even be defects. First, we present the results of the $LiNbS_2$ (001), specifically we made the calculations with 5 layers and a vacuum of 15 Å. We fixed the positions of the 2 bottom layers and allowed to relax the three remaining ones. We chose 5 layers as we have performed various calculations for various numbers of layers (such as 4, 6, and 7) and consequently from 5 layers it is possible to obtain reasonable and reliable

Table 4.3: Computed SCAN+rVV10 crystallographic data for LiNbS$_2$ with symmetry $P6_3/mmc$; the u, v, w are the fractional coordinates.

property		Calculated (SCAN+rVV10)	
Space group		$P6_3/mmc$	
$a = b$(Å)		3.357	
c(Å)		12.837	
$\alpha = \beta(°)$		90	
$\gamma(°)$		120	
Volume (Å^3)		125.27	
B_0(GPa)		87.46	
sites	u	v	w
Nb(1)	0.0000	0.0000	0.7500
Nb(2)	0.0000	0.0000	0.2500
S(1)	0.6667	0.3333	0.1275
S(2)	0.3333	0.6667	0.3725
S(3)	0.3333	0.6667	0.12755
S(4)	0.6667	0.3333	0.8725
Li(1)	0.0000	0.0000	0.0000
Li(2)	0.0000	0.0000	0.5000

Table 4.4: Calculations for LiNbS$_2$ using SCAN + rVV10 and HSE. We calculated the partial density of states and consequently the band gap E_g

| Functional	Band gap (eV)
SCAN+rVV10	0.88
HSE06	1.21
HSE12s	1.02
HSE12	1.27
Experimental	1.3
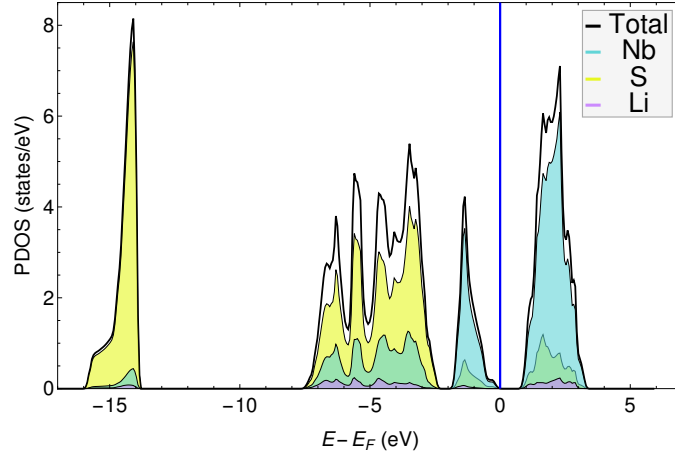
Figure 4.13: Partial density of states of bulk LiNbS$_2$ computed with SCAN+rVV10. The Fermi level is centered at 0 and represented with the blue line.
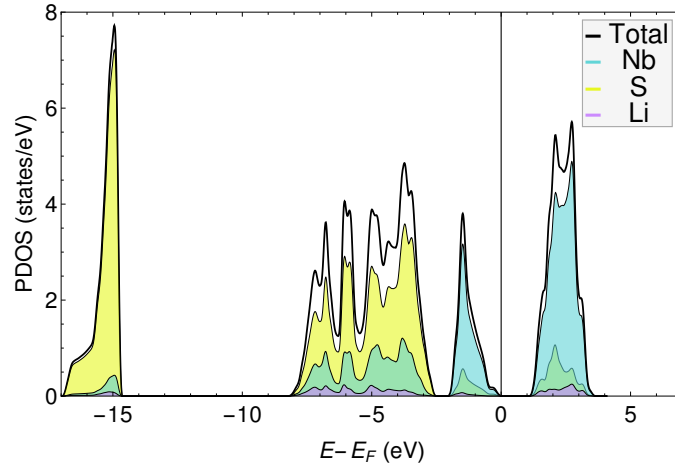
Figure 4.14: Partial density of states of bulk LiNbS$_2$ computed with HSE06. The Fermi level is centered at 0. The peaks provided by HSE06 are very similar to the spectrum provided by SCAN + rVV10.

results of the surfaces [†]. Besides, we chose the mesh of **k**-points $14 \times 14 \times 1$ and make calculations of slabs 1x1 and 2x2 [‡].

[†]Some plots for several layers are presented in the appendix A, figs. (A.3) and (A.4)

[‡]1x1 and 2x2 refers to the periodic extension of the slab in the *a* and *b* direction. Then, if we have for instance a 2x2 extension, this means that we have repeated the cell twice in *a* and twice in *b*. The figures of every structure are presented so that it is very clear how the the system was arranged.
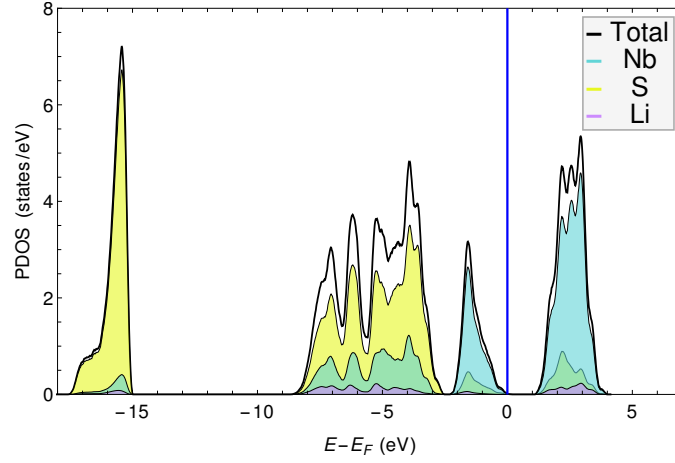
Figure 4.15: Partial density of states of bulk LiNbS$_2$ computed with HSE12. The Fermi level is centered at 0 and represented with the blue line. This is the most accurate description of the band gap.
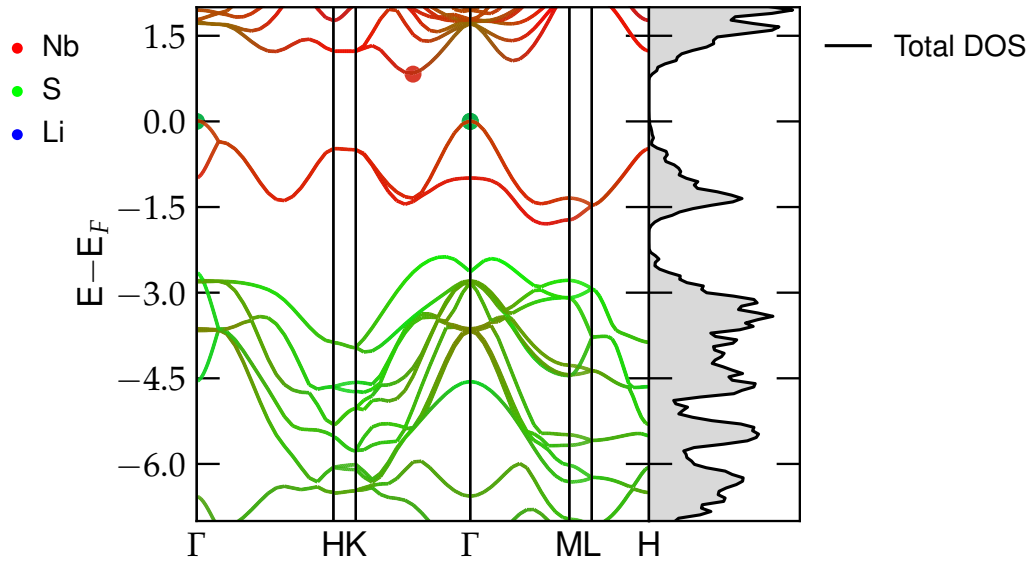
Figure 4.16: SCAN + rVV10 computed band structure for LiNbS$_2$ along the high symmetry points. Nb bands are plotted in red, S bands are in green, and Li bands are in blue. The valence band maximum (VBM) lies in Γ and is represented by a dark green circle. The conduction band minimum (CBM) is between K and Γ and is represented by a dark red circle. As we used the SCAN + rVV10 functional, the band gap is around 0.88 eV. Also, as the VBM and CBM are not in the same high symmetry **k** point, the bandgap is indirect.

4.2.4 The LiNbS$_2$(001)-1×1 surfaces with lithium on top

We present the results for one slab of 5 layers with the top filled with lithium. Notice we considered a vacuum of 15 Å in all the slabs. Also, there is the possibility for changing the position of the lithium along the surface, therefore we present the results for several cases. In general, the top most layer of all these systems will have an arrangement of S-Nb-S-Li, going from within to the external part of the slab.

4.2.4.1 The LiNbS$_2$(001)-1×1 Li-terminated pristine

The arrangement of this system is the original expansion of the bulk for a surface system. The PDOS of the top most layer and the atomic structure for this system are shown in fig. (4.17). This surface has a metallic character. Near E_F we observe a peak at -0.22 eV that is composed by Nb-4d with a contribution of S-3p and Li-2s. We also observe an occupied subband ranging from -2.6 to -1.1 eV that is mainly composed of Nb-4d. Finally, the unoccupied band has a main peak at 1.7 eV composed mainly of Nb-4d and minor contributions of S-3p and Li-2p.
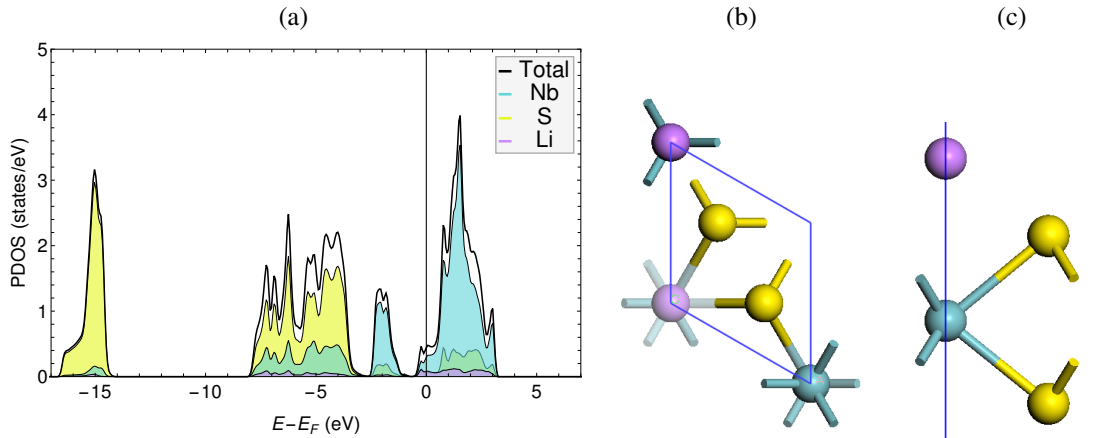
Figure 4.17: The LiNbS$_2$(001)-1×1 Li-terminated pristine surface. a) PDOS of the system, the Fermi level is centered at zero. b) Top view of the slab, c) Side view of the first layer of the slab. The atoms in: purple are Li, yellow are S, and light blue are Nb; the uppermost atoms are in full color, otherwise they are faded. The blue solid lines represent the limits of the unit cell.

4.2.4.2 The LiNbS$_2$(001)-1×1 Li-terminated bridge

The arrangement of lithium bridge consists in moving the Li atom just in the middle of a niobium and a sulfur. The PDOS and the atomic structure for this system are shown in fig. (4.18). The surface shows a metallic character and is very similar to the previous case Li-terminated pristine. However, subtle differences exist: near E_F we observe a smooth decaying curve (instead of a peak) from 0 eV to -0.22 eV, this region is composed mainly by Nb-4d with a contribution of S-3p and Li-2s. We also observe an occupied subband ranging from -2.6 to -0.9 eV that is composed

principally of Nb-4d and S-3p . Finally, the unoccupied band has two peaks at 0.93 eV and 1.45 eV respectively, composed of Nb-4d and minor contributions of S-3p and Li-2p.
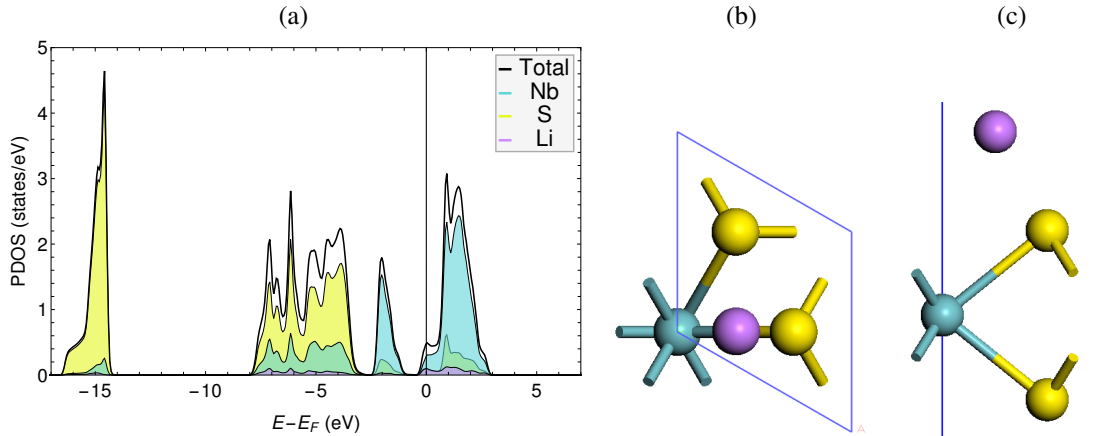

Figure 4.18: The LiNbS$_2$(001)-1×1 Li-terminated bridge surface. a) PDOS of the system, the Fermi level is centered at zero. b) Top view of the slab, c) Side view of the first layer of the slab. The atoms in: purple are Li, yellow are S, and light blue are Nb. The blue solid lines represent the limits of the unit cell.

4.2.4.3 The LiNbS$_2$(001)-1×1 Li-terminated above surface S site

This arrangement consists in moving the Li atom just above the nearest S atom. The PDOS of the topmost layer and the atomic structure for this system is shown in fig. (4.19). This surface shows a metallic character. What is interesting about this system is that around E_F, from -1.58 eV to +3.46 eV there is an almost constant contribution of Li-2p states. In this context, we have an occupied band ranging from -1.58 eV to E_F with one peak at -0.80 eV and another at -0.30 eV composed principally of Nb-4d and a tiny contribution of S-3p. On the other hand, we have an unoccupied band from E_F to +3.46 eV (continuous to the previous one) with a mean peak around 2.4 eV and a main composition of Nb-4d and S-3p.

4.2.4.4 The LiNbS$_2$(001)-1×1 Li-terminated above subsurface S site

This system is constructed by moving the Li atom just above a S atom that is in the sub-surface, i.e., a sulfur in a lower layer than the topmost one. The PDOS of the topmost layer and the atomic structure for this system is shown in fig. (4.20). This surface shows a metallic character. Interestingly, all the occupied bands resemble almost the same peaks shown in the surface LiNbS$_2$(001)-1×1 Li-terminated pristine, fig. (4.17). The mean features in this present case are that around E_F there is a small peak at -0.22 eV that is composed by Nb-4d with a contribution of S-3p and Li-2s. Again, there is a subband ranging from -2.53 to -0.87 eV that is mainly composed of Nb-4d and presents just
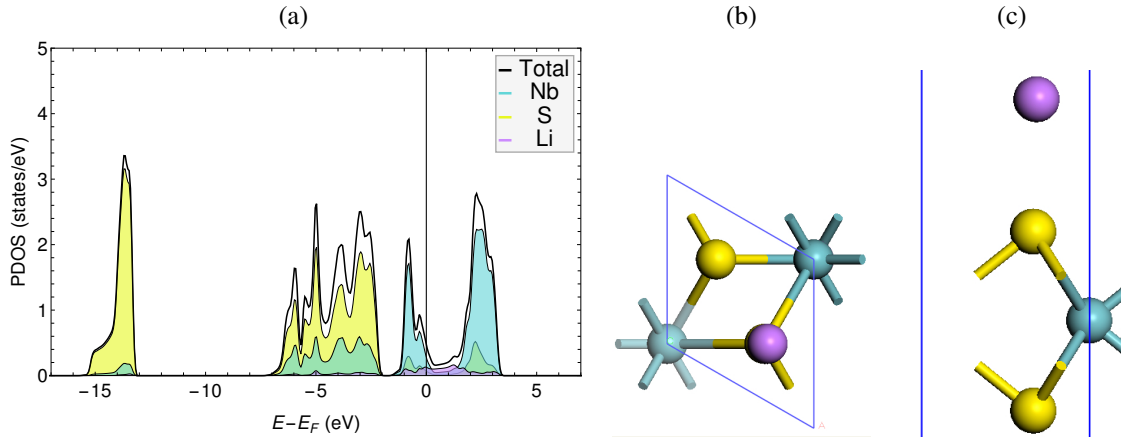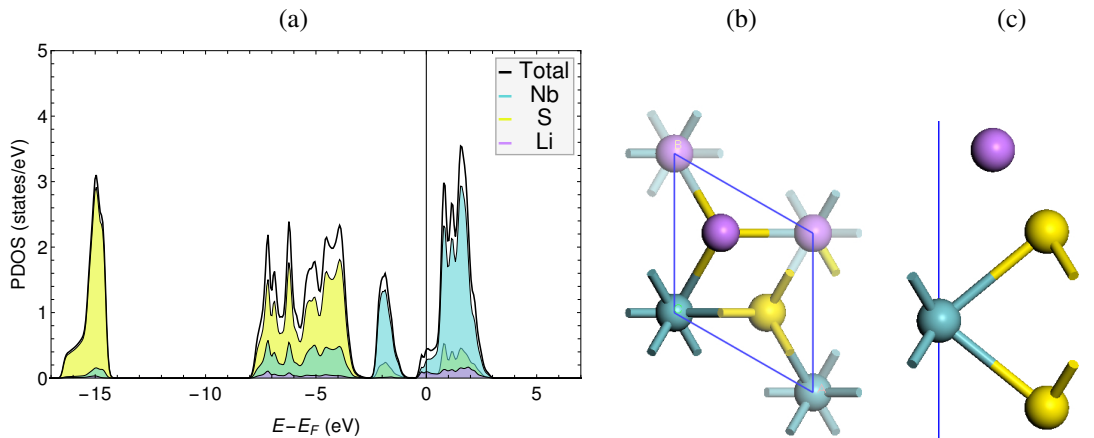
Figure 4.19: The LiNbS$_2$(001)-1 × 1 Li-terminated above surface S site. a) PDOS of the system, the Fermi level is centered at zero. b) Top view of the slab, c) Side view of the first layer of the slab. The atoms in: purple are Li, yellow are S, and light blue are Nb. The blue solid lines represent the limits of the unit cell.

one peak at around -1.91 eV. Furthermore, the unoccupied band has three main peaks at 0.8 eV, 1.15 eV, and 1.57 eV formed principally by Nb-4d and minor contributions of S-3p and Li-2p.

Figure 4.20: The LiNbS$_2$(001)-1x1 Li-terminated above subsurface S site. a) PDOS of the system, the Fermi level is centered at zero. b) Top view of the slab, c) Side view of the first layer of the slab. The atoms in: purple are Li, yellow are S, and light blue are Nb. The uppermost atoms are in full color, otherwise they are faded. The blue solid lines represent the limits of the unit cell. In addition, notice the side view c) looks very similar to the *bridge* arrangement in fig. (4.18). The difference is that the Li is further than it appears just above a S atom that is in the second layer (not shown in the figure)

4.2.4.5   Energy of the LiNbS$_2$(001)-1×1 surfaces with lithium on top

In our calculations we also determined the value of the energies of all the systems described previously. The summary is presented in the Table (4.5). The most stable structure is *Li-terminated pristine*, this means that to move the lithium from the original *lithium pristine* position is not energetically favorable.

Table 4.5: Total energy for every LiNbS$_2$(001)-1x1 surface Li on top as described in section (4.2.4).

System	ΔE (eV)
pristine	0.000
bridge	0.012
above subsurface S	0.118
above surface S	0.522

4.2.5   LiNbS$_2$ (001)-2×2 surface reconstruction Li-terminated

After the calculations in LiNbS$_2$ (001)-1×1 surfaces, we explored the slabs with 2×2 reconstruction. This is done to take into account defects in the surfaces. Here I describe various cases of arrangements for 2×2 surfaces with Li atoms filling the top of the slab with an arrangement of the form S-Nb-S-Li, going from within to the top of the slab.

4.2.5.1   LiNbS$_2$ (001)-2×2 Li-terminated pristine

This system is a 2×2 extension of the the structure analyzed in section (4.2.4.1), so both systems are equivalent. The PDOS of the topmost layer and the atomic structure for this system is shown in fig. (4.21). This surface presents a metallic character and is very similar to the 1×1 extension, nevertheless some differences appear. Just almost centered in E_F we observe a peak that is composed by Nb-4d with a contribution of S-3p and Li-2s. We also observe an occupied subband ranging from -2.6 to -0.86 eV that is mainly composed of Nb-4d. Finally, the unoccupied band has several peaks at 0.9, 1.27, 1.55, and 1.97 eV composed mainly of Nb-4d and minor contributions of S-3p and Li-2p.

4.2.5.2   LiNbS$_2$ (001)-2×2 Li-terminated pristine with one Li-vacancy

The arrangement of this structure consists of a surface taking out one Li from the LiNbS$_2$ (001)-2×2 Li-terminated pristine surface. The PDOS of the topmost layer and the atomic structure for this system is shown in fig. (4.22). The surface shows a metallic character. One interesting feature is one peak, composed mainly of Nb-4d and Li-2s, that is exactly at E_F. We also observe one subband ranging from -2.44 eV to -0.6 eV formed mainly by Nb-4d and a few states of S-3p. Finally, there is an unoccupied band consisting of two peaks at 1.1 eV and 1.66 eV composed principally of Nb-4d and tiny contributions of S-3p and Li-2s.
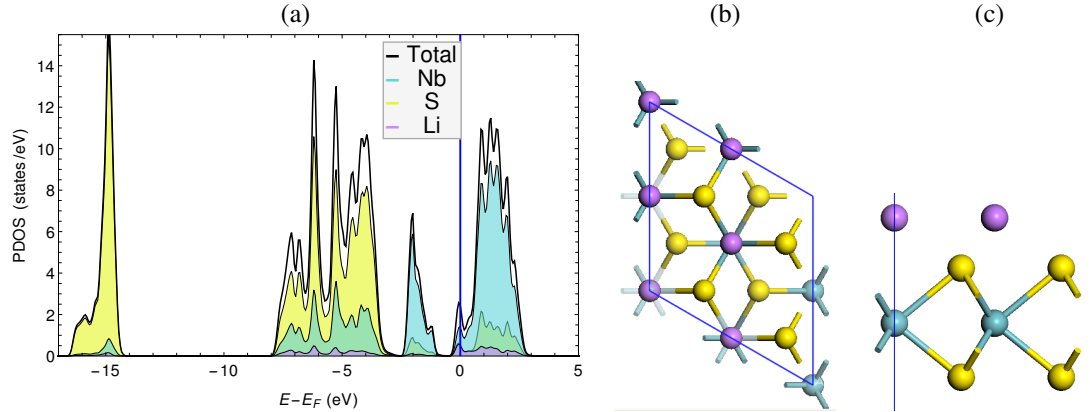
Figure 4.21: LiNbS$_2$ (001)-2 × 2 Li-terminated pristine surface. a) PDOS of the system, the Fermi level is centered at zero and is represented with the blue line. b) Top view of the slab, c) Side view of the first layer of the slab. The atoms in: purple are Li, yellow are S, and light blue are Nb. The uppermost atoms are in full color, otherwise they are faded. The blue solid lines represent the limits of the unit cell.
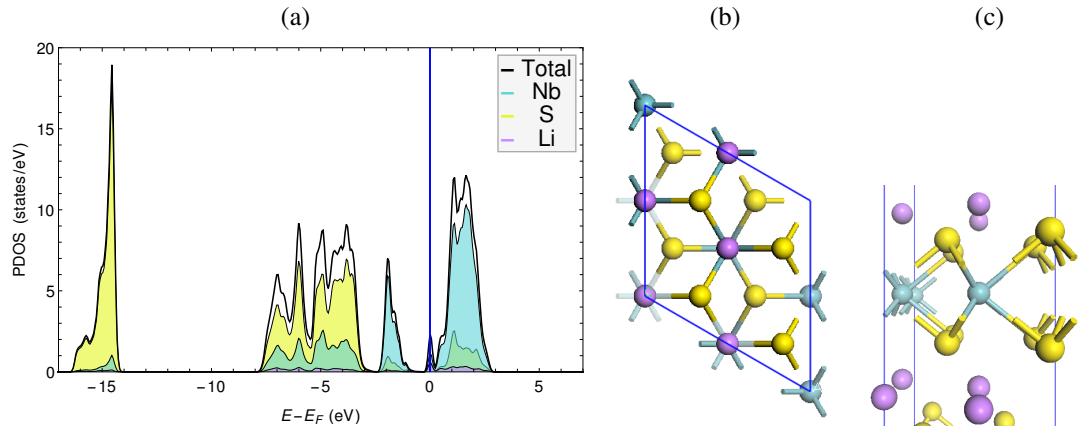

Figure 4.22: LiNbS$_2$ (001)-2 × 2 Li-terminated pristine with one Li-vacancy surface. a) PDOS of the system, the Fermi level is centered at zero and is represented with the blue line. b) Top view of the slab, c) Side perspective view of the first layer of the slab, notice that now we have just three Li atoms on the topmost part of the surface. The atoms in: purple are Li, yellow are S, and light blue are Nb. The uppermost atoms are in full color, otherwise they are faded. The blue solid lines represent the limits of the unit cell.

4.2.5.3   LiNbS$_2$ (001)-2×2 Li-terminated pristine with three Li-vacancy

The arrangement of this structure consists of a surface taking out two Li from the arrangement of Li pristine. The PDOS of the topmost layer and the atomic structure for this system is shown in fig. (4.23). This surface displays a metallic character. Notice that as we have less Li atoms, there is no presence of Li-2s states; remember that in the system of just one vacancy of Li shown in fig. (4.22), there was one peak exactly at E_F with a considerable amount of states of Li, this peak now disappears. Also, there was one occupied subband, and one unoccupied subband. It turns out that these two bands now are shifted to the right, so that there is one subband formed by Nb-4d and S-3p states ranging from -1.45 eV to E_F with a peak exactly at E_F and another one at -0.64 eV. On the other hand, the occupied band ranges from 1.16 to 3.26 eV and presents two peaks at 2.42 eV and 2.72 eV. This band is composed mainly of Nb-4d and S-3p states.
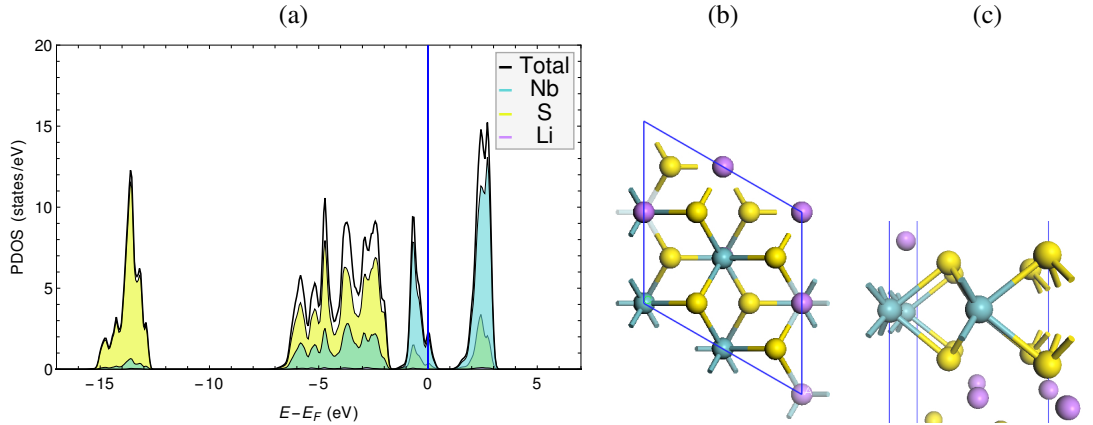

Figure 4.23: LiNbS$_2$ (001)-2×2 Li-terminated pristine with three Li-vacancy surface. a) PDOS of the system, the Fermi level is centered at zero and is represented with the blue line. b) Top view of the slab, c) Side perspective view of the first layer of the slab, notice that now we have just one Li atom on the topmost part of the surface. The atoms in: purple are Li, yellow are S, and light blue are Nb. The uppermost atoms are in full color, otherwise they are faded. The blue solid lines represent the limits of the unit cell.

4.2.6   LiNbS$_2$ (001)-2×2 S-terminated

Here I describe various cases of arrangements for 2×2 surfaces with S atoms filling the top of the slab. This means that we took out all the Li atoms that were on the top. Hence, the arrangement of atoms from within to the top are S-Nb-S.

4.2.6.1 LiNbS$_2$ (001)-2×2 S-terminated pristine

The arrangement of LiNbS$_2$ (001)-2×2 S-terminated is a slab without lithium on the surface. The PDOS of the topmost layer and the atomic structure for this system are shown in fig. (4.24). This surface shows metallic character. Around E_F there is an occupied subband composed principally of Nb-4d and S-3p, there is one peak at -0.73 eV. Also, there is an occupied band states with a peak at -0.42 eV. Also, there is an unoccupied band formed by Nb-4d and a minor contribution of S-3p states, this band ranges from 1.22 to 3.6 eV and has 3 peaks at 2.12, 2.50, and 3.00 eV.

Furthermore, if we compare this system with the one that had three vacancies of Li, fig. (4.23), both PDOS are very similar. For instance, one similarity is the peak at -0.42 eV, though now it has around twice the states of Nb-4d. What is observed is that if we take out completely the Li atoms, Nb-4d states will predominate around E_F in the occupied band. On the other hand, the unoccupied band will have less density of states composed mainly of Nb-4d.
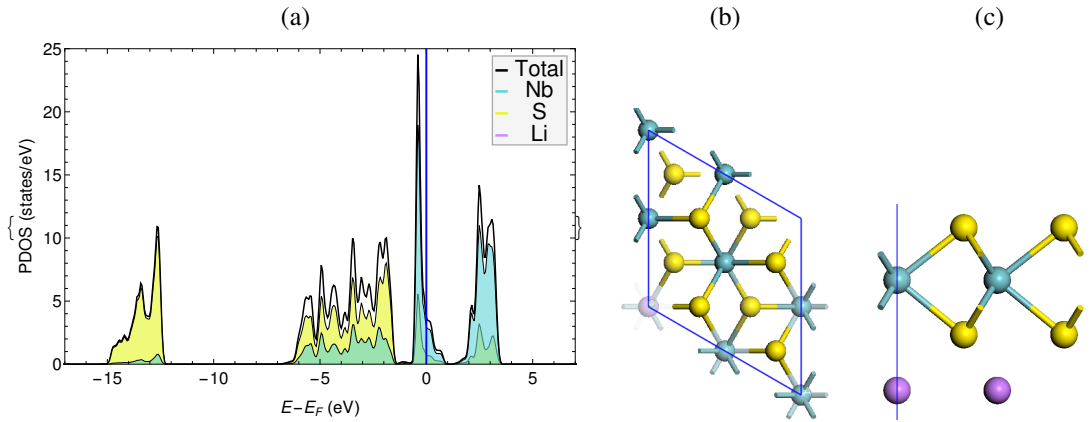

Figure 4.24: LiNbS$_2$ (001)-2×2 S-terminated pristine. a) PDOS of the system, the Fermi level is centered at zero and is represented with the blue line. b) Top view of the slab, c) Side view of the first layer of the slab, notice that now we have no Li atoms on the topmost part of the surface; the Li atoms in the bottom correspond to the second layer of the slab. The atoms in: purple are Li, yellow are S, and light blue are Nb. The uppermost atoms are in full color, otherwise they are faded. The blue solid lines represent the limits of the unit cell.

4.2.6.2 LiNbS$_2$ (001)-2×2 S-terminated with one S-vacancy

The basis of this system is the previous one in section (4.2.6.1) with the surface terminated in sulfur, nevertheless, we now take out one atom of sulfur. The PDOS of the topmost layer and the atomic structure for this system are shown in fig. (4.25). This surface shows a metallic character. Around E_F, there is an occupied subband mainly with states of Nb-4d and a tiny contribution of S-3p, there is one peak at -0.73 eV. Also, there are two occupied subbands mainly composed of Nb-4d states. The first one ranges from E_F to 0.79 eV and one peak at 0.1eV. The other one ranges from 0.8 to 3.5 eV with two peaks at 1.12 and 2.35 eV.
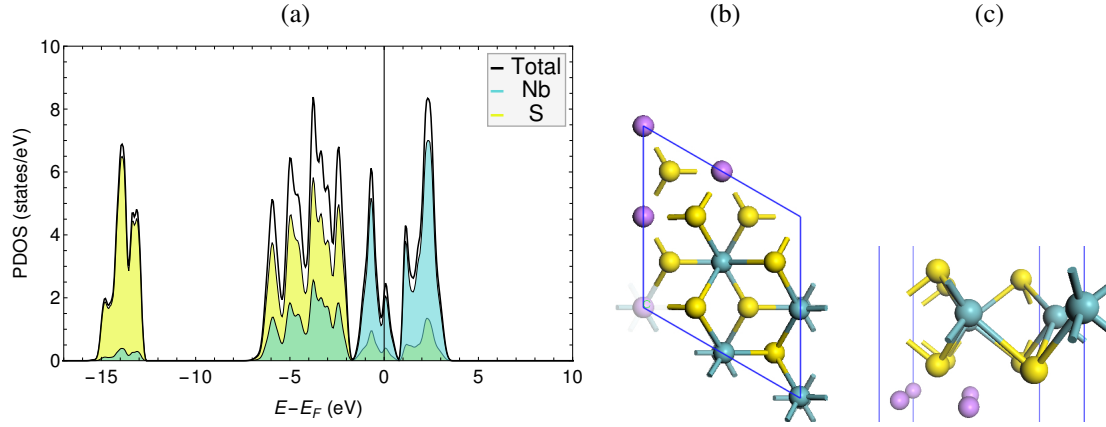
Figure 4.25: LiNbS$_2$ (001)-2 × 2 S-terminated with one S-vacancy. a) PDOS of the system, the Fermi level is centered at zero. b) Top view of the slab. c) Perspective side view of the first layer of the slab, notice that now we have no Li atoms on the topmost part of the surface and one sulfur less than in the pristine case; the Li atoms in the bottom correspond to the second layer of the slab. The atoms in: purple are Li, yellow are S, and light blue are Nb. The uppermost atoms are in full color, otherwise they are faded. The blue solid lines represent the limits of the unit cell.

4.2.7   Simulated constant current STM images

We simulated the constant current STM images (topography mode) for surfaces LiNbS$_2$(001) − 2 × 2 Li-terminated [fig. (4.21)] and LiNbS$_2$(001) − 2 × 2 S-terminated [fig. (4.24)] using the Tersoff-Hamann approximation.

In fig. (4.26) is displayed the computed STM image for LiNbS$_2$(001) − 2 × 2 Li-terminated surface with V$_{bias}$ = −2.54 V (occupied states) and +1.1 V (unoccupied states). The topography for both voltages show similar topology, the bright spots are located on the position of the topmost Li atoms and the darker spots locate the position of the superficial S atoms. In fig. (4.27) is shown the computed partial charge density integrated from -2.54 eV to E_F, this shows that 2s states from the surface Li atoms protrude into the vacuum resulting in the bright spots in the STM image, though the Li 2s-orbitals contribution is not very significant. Furthermore, it is noticeable the 3p_z S orbitals' contribution, though they do not protrude very significantly. Despite the main contribution of Nb-4d_{z^2} states in the PDOS within the sub-band 2.54 eV below E_F, these states are not probed by the STM due to geometric position of these atoms that are beneath the surface S atoms.

In fig. (4.28) is displayed the computed STM image for LiNbS$_2$(001) − 2 × 2 S-terminated surface with V$_{bias}$ = −0.56 V (occupied states) and +1.1 V (unoccupied states). The topography for both voltages show similar topology, the bright spots are located on the position of the topmost S atoms and the dark spots locate the position of the subsurface Nb atoms. In fig. (4.29) is shown the computed partial charge density integrated from -0.56 eV to E_F, this shows that 3p_z states from the surface S atoms protrude into the vacuum resulting in the bright spots in the STM image. It is important to stress that despite the main contribution of Nb-4d_{z^2} states in the PDOS within the
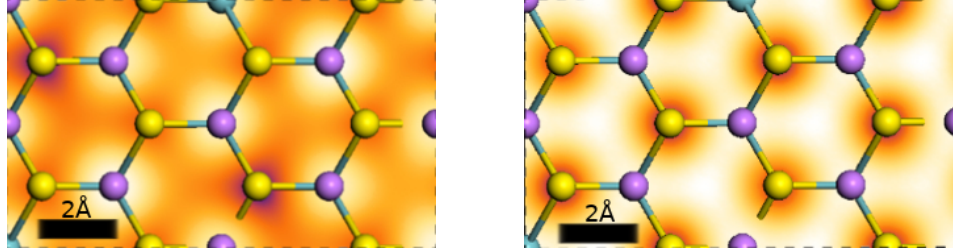
Figure 4.26: DFT-SCAN+rVV10 computed filled states STM image of LiNbS$_2$ (considering Li on top) with $V_{bias} = -2.54$V (left), and computed empty states STM image $V_{bias} = 1.1$V(right). The atoms in yellow (purple) are sulfur (lithium). Niobium atoms are not visible as they are under Li.
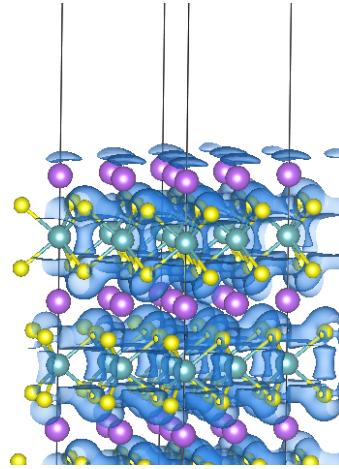

Figure 4.27: Computed partial charge density of occupied states within the range -2.54 eV to E_F. The blue surface corresponds to an iso-density of $2.45 \times 10^{-3} e/\mathring{A}^3$. The Nb, S and Li atoms are represented by spheres cyan, yellow and violet, respectively. The dark lines denotes the slab supercell.

sub-band 0.56 eV below E_F, these states are not probed by the STM due to geometric position of these atoms that are beneath the surface S atoms.

4.2.8 Bulk LiNbS$_2$ phonon band structure

The SCAN+rVV10 computed phonon band structure and the phonon density of states (DOS) of LiNbS$_2$ is shown in fig. (4.30). Notice that the phonon band structure are very similar in both systems. There are some bands in which the frequency approaches to zero linearly as they approach to Γ, these bands are named *acoustic* for they are responsible of the propagation of the sound in the material. On the other hand the remaining bands are known as *optical* as their vibrations can exchange energy with an electromagnetic field[21]. We decided to compute phonons
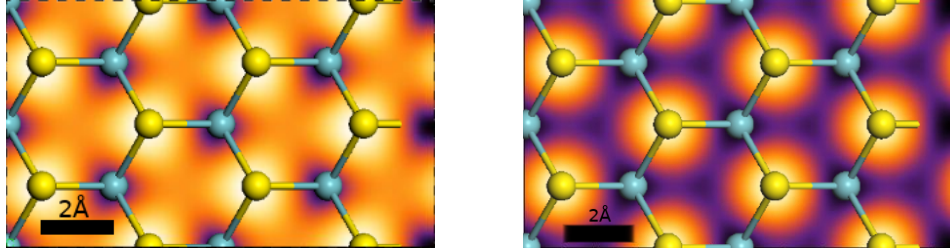
Figure 4.28: DFT-SCAN+rVV10 computed filled states STM image of LiNbS$_2$ (considering S on top) with V_{bias} = −0.56V (left), and computed empty states STM image V_{bias} = 1.1V(right). The atoms in yellow (light blue) are sulfur (niobium). In this case, lithium atoms are not visible.
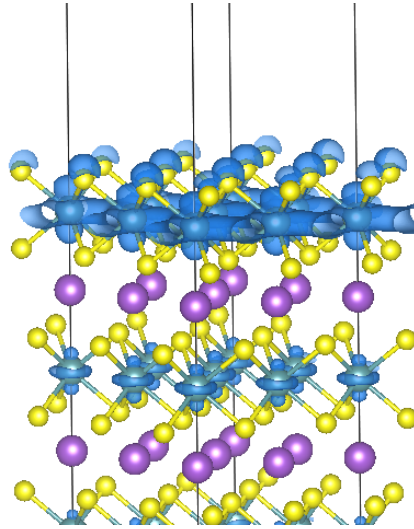

Figure 4.29: Computed partial charge density of occupied states within the range -0.56 eV to E_F. The light-blue surface corresponds to an iso-density of $7 \times 10^{-3} e/\text{Å}^3$. The Nb, S and Li atoms are represented by spheres cyan, yellow and violet, respectively. The dark lines denotes the slab supercell.

for structures as they are energetically very close. The calculations show no negative frequencies suggesting this computed phase is stable.
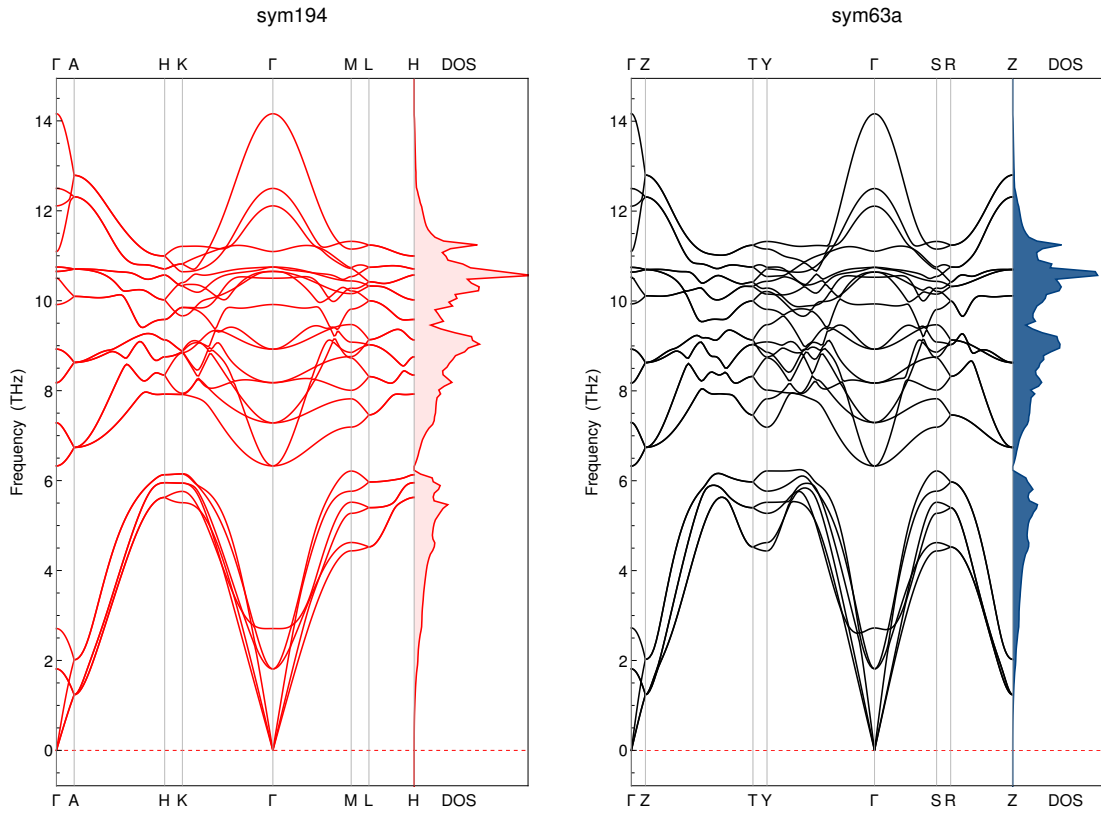
Figure 4.30: Phonon band structure and DOS (in units of states/(THz-atom)) of bulk LiNbS$_2$. Following Table (4.2), in the left we present the bands for the most stable system *P*6$_3$/*mmc* (194). In the right, the results for *Cmcm* (63a) system are shown.

Chapter 5

Conclusions & Outlook

In this thesis we have described the electronic structure of NbS_2, proving that this system is metallic. To analyze NbS_2 we have used the SCAN+rVV10 and HSE06 functionals, both yielding similar results. Hence, SCAN is proven to work well with NbS_2 at lower computational cost than HSE06. This fact suggests that working with SCAN for studying other TMDs as MoS_2 would be an interesting testing ground for the capabilities of this state-of-the-art functional.

Furthermore, it is possible to add Li atoms among the layers of NbS_2 obtaining $LiNbS_2$. We studied thoroughly the electronic structure and the stability of $LiNbS_2$, specifically the symmetry $P6_3/mmc$ (194). In the case of the bulk system, there is a bandgap of around 1.3 eV, obtained experimentally. In our work, we computed the best description of the bulk $LiNbS_2$ bandgap by means of the hybrid HSE12, getting 1.27 eV and therefore overcoming HSE06, HSE12s, and even SCAN. This is a highlight which suggests that HSE12 can be used for obtaining very accurate results in relation to HSE06. Also, we computed the band structure of $LiNbS_2$ with the SCAN+rVV10 functional, identifying an indirect bandgap.

In addition, we discovered that one should be very careful with the possible symmetries of $LiNbS_2$: a slightly perturbation in the unit cell angle γ produces that the symmetry changes abruptly. Then, a very meticulous specification of the atomic positions in the initial unit cell before starting all the calculations is highly recommended. Also, notice that SCAN can present problems of convergence when dealing with cells that are large. In this case, one can try to make modifications of the internal routines implemented in VASP to overcome the problem, and/or make a tiny perturbation in one of the positions that have been specified. Again, a double-check for changes in the symmetry is recommended. One remarkable result was obtained via phonon band structure calculations of the bulk systems $P6_3/mmc$ (194) and *Cmcm* (63a). It turns out that no negative frequencies exist, suggesting that both systems are stable and can physically exist.

We also performed calculations of the $LiNbS_2$ (001) surface based on the most optimal structure obtained for the bulk $LiNbS_2$ system, i.e., we based the construction of our slabs on the $P6_3/mmc$ (194) structure. We calculated the PDOS of various possible arrangements of surfaces: changing the position of the topmost lithiums, without lithiums, and changing the position of the topmost sulfurs. Besides, we built some defects, taking out some topmost atoms.

What is remarkable is that in all the cases the surface behaviour is metallic. Furthermore, we were able to calculate the energies of the surfaces, nevertheless it is not possible to affirm which structure of all the considered ones is the most stable due to the fact that the surface is not stoichiometric. Further studies to understand the stability of the $LiNbS_2$ (001) surfaces are needed. In this context, the combination of theoretical studies along with experiments will allow to understand better the bulk and $LiNbS_2$ (001) surfaces stability.

We also were able to compute the constant current STM images (topography mode) for surfaces $LiNbS_2(001) - 2 \times 2$ Li-terminated and $LiNbS_2(001) - 2 \times 2$ S-terminated using the Tersoff-Hamann approximation, obtaining several images for occupied and unoccupied states. Besides, we calculated the partial charge density for each surface, so that we were able to understand the STM results. It turns out that the topology of both the occupied and unoccupied states for all the analyzed surfaces is very similar. Nevertheless, when we have Li as the topmost atom, its $2p_z$ orbitals contribution is the one that protrudes the most along with $3p_z$ S orbitals. On the other hand, when we consider S as the topmost atom, its $3p_z$ orbitals provide the main contribution for the observed image. In general, we can affirm that we are working in the limit of the possible resolution for STM, therefore an analysis with other techniques such as AFM is needed in order to truly understand the $LiNbS_2(001)$ surfaces. Via this type of techniques it could even be possible to discover which of the two surfaces analyzed here is the most stable.

One remarkable aspect regarding the electronic structure of bulk NbS_2 is a bandgap opening of around 1.3 eV when we intercalate Li atoms in between the S-Nb-S layers. Since NbS_2 has a potential application in quantum computing due to effects of charge and spin fluctuations[15], then $LiNbS_2$ could be considered for future works and applications in this emerging field. Furthermore, the value of the bandgap in the bulk $LiNbS_2$ (1.3 eV) is in the range of infrared whereas the surface (001) is metallic, suggesting potential applications in optoelectronics.

Moreover, analysis of superconductivity in both NbS_2 and $LiNbS_2$ is needed. This could yield an entire field of more applications. Even more, an analysis of phase transitions should be considered in further studies. It can also be interesting to explore via DFT other intercalations of NbS_2 with elements such as Na, K, Rb, and Cs. Finally, it is important to remark that exploring new layered compounds similar to NbS_2 and $LiNbS_2$ is a promising field but also challenging from the experimental and theoretical point of view.
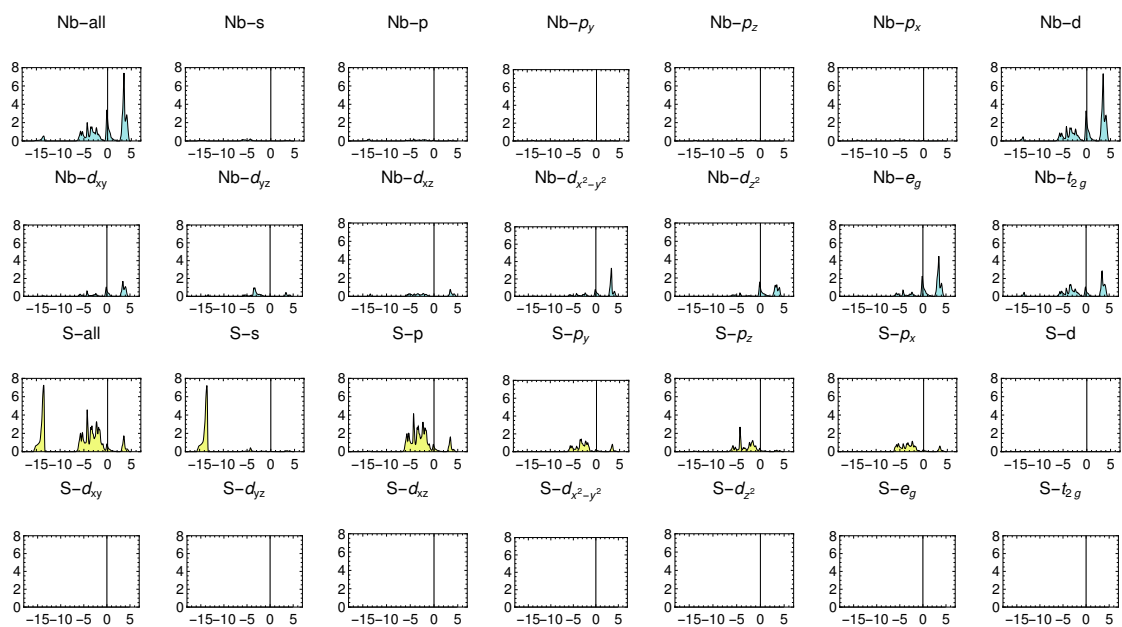
Appendix A

Figure A.1: Detailed density of states of NbS$_2$ computed with HSE06. The states of every orbital are shown. The horizontal axis is the $E - E_F$(eV) and the vertical axis are States/eV. In the electronic version is possible to zoom for high resolution.

Figure A.2: Detailed density of states of LiNbS$_2$ computed with HSE12. The states of every orbital are shown. The horizontal axis is the $E - E_F$(eV) and the vertical axis are States/eV. In the electronic version is possible to zoom for high resolution.
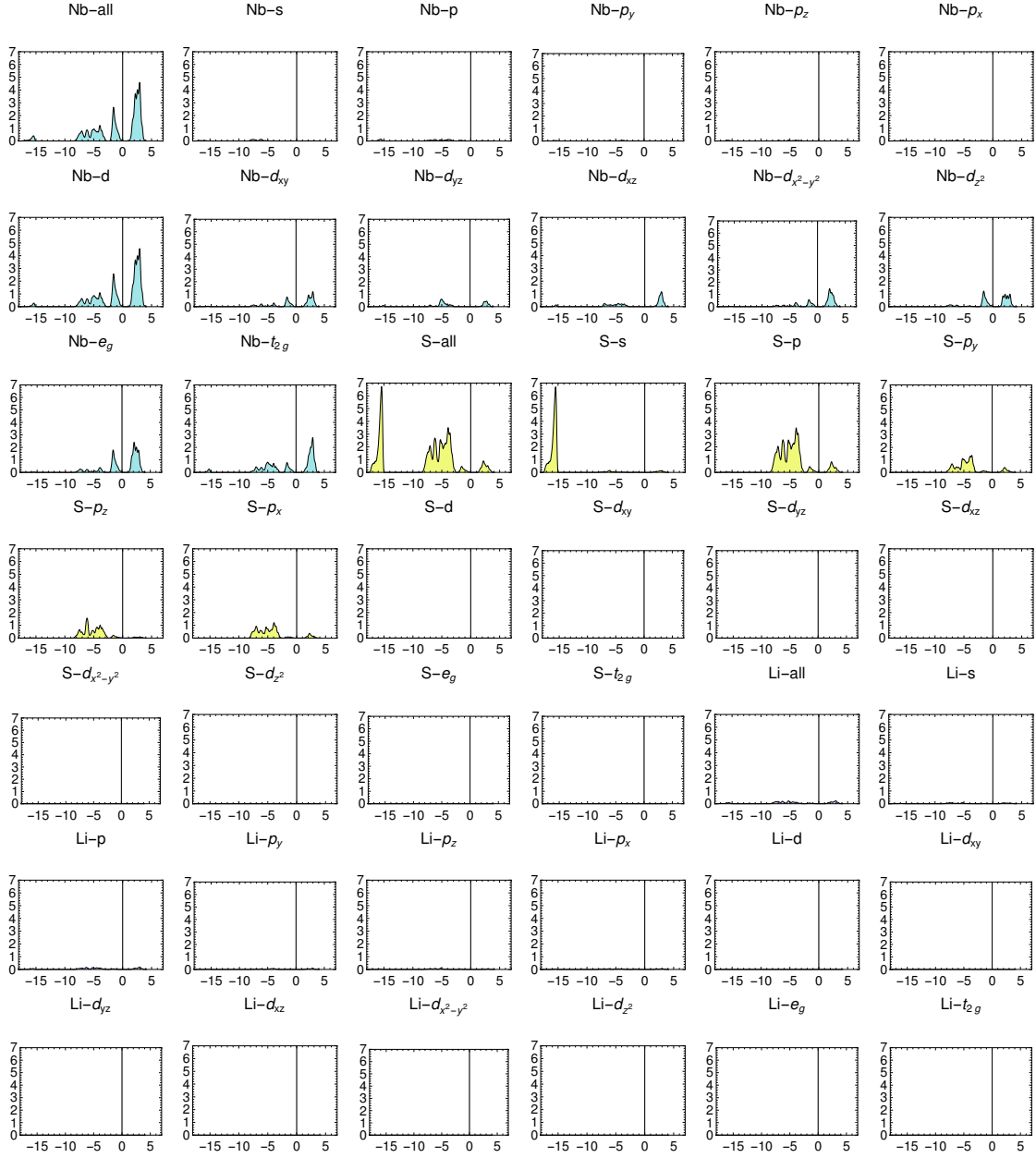
Figure A.3: LiNbS$_2$ 2x2 surface with Li on top, case Li pristine. PDOS for each layer of the slab; the Fermi level is centered at zero and is represented with the blue line. The top plot is the first layer, and as we go down, we good deep into the surface and consequently have a bulk behavior.
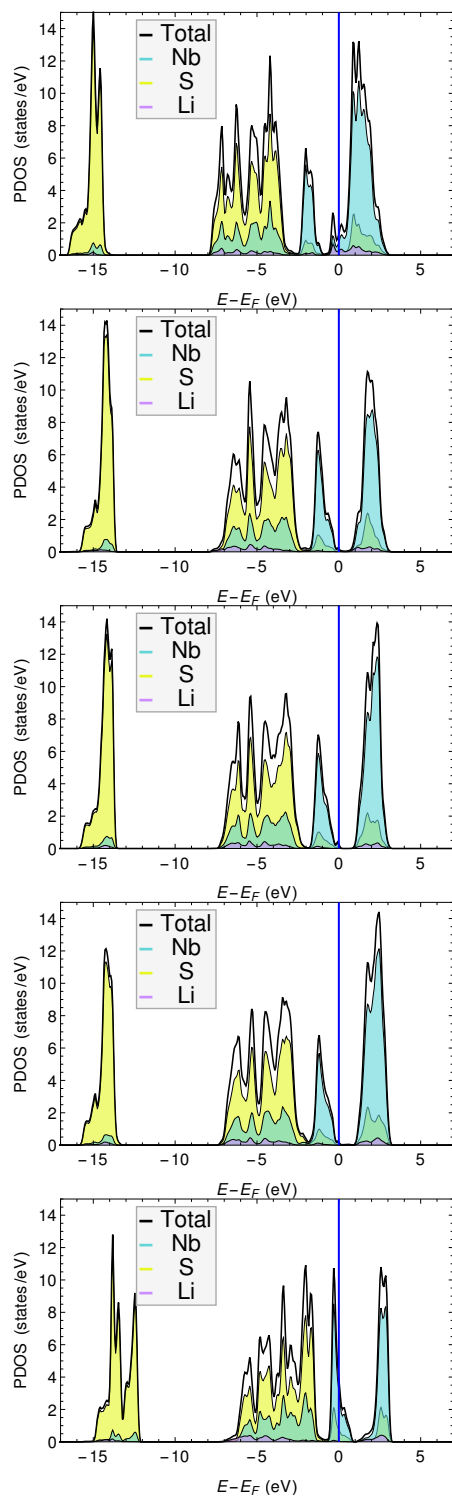
Figure A.4: LiNbS$_2$ 2x2 surface with S on top, case S pristine. PDOS for each layer of the slab; the Fermi level is centered at zero and is represented with the blue line. The top plot is the first layer, and as we go down, we good deep into the surface and consequently have a bulk behavior.
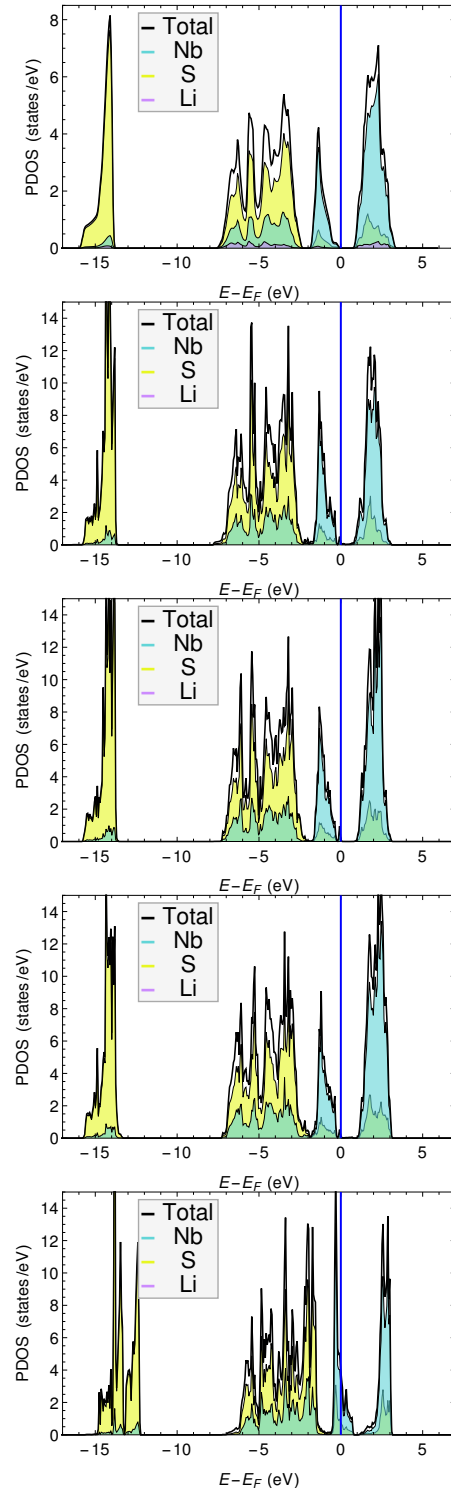
Bibliography

[1] Dines, M. B. Intercalation in layered compounds. *Journal of Chemical Education* **1974**, *51*, 221.

[2] Dines, M. B. Lithium intercalation via n-Butyllithium of the layered transition metal dichalcogenides. *Materials Research Bulletin* **1975**, *10*, 287 – 291.

[3] Dresselhaus, M. S. *Intercalation in layered materials*; Springer, 2013; Vol. 148.

[4] Payne, M. *The Industrial Impact of Materials Modelling*.

[5] Goldbeck, G. The economic impact of molecular modelling of chemicals and materials. *Goldbeck Consulting* **2012**,

[6] Li, W.; Walther, C. F.; Kuc, A.; Heine, T. Density functional theory and beyond for band-gap screening: performance for transition-metal oxides and dichalcogenides. *Journal of chemical theory and computation* **2013**, *9*, 2950–2958.

[7] Bernardi, M.; Grossman, J. *Photovoltaics: Advances in First Principles Modeling – Overview: Ultrathin Solar Cells*.

[8] Geim, A. K.; Grigorieva, I. V. Van der Waals heterostructures. *Nature* **2013**, *499*, 419–425.

[9] Rasmussen, F. A.; Thygesen, K. S. Computational 2D materials database: electronic structure of transition-metal dichalcogenides and oxides. *The Journal of Physical Chemistry C* **2015**, *119*, 13169–13183.

[10] Wan, J.; Lacey, S. D.; Dai, J.; Bao, W.; Fuhrer, M. S.; Hu, L. Tuning two-dimensional nanomaterials by intercalation: materials, properties and applications. *Chemical Society Reviews* **2016**, *45*, 6742–6765.

[11] Kuc, A.; Zibouche, N.; Heine, T. Influence of quantum confinement on the electronic structure of the transition metal sulfide T S 2. *Physical Review B* **2011**, *83*, 245213.

[12] Radisavljevic, B.; Radenovic, A.; Brivio, J.; Giacometti, V.; Kis, A. Single-layer MoS_2 transistors. *Nature nanotechnology* **2011**, *6*, 147–150.

[13] others,, *et al.* Electrically tunable excitonic light-emitting diodes based on monolayer WSe 2 p–n junctions. *Nature nanotechnology* **2014**, *9*, 268–272.

[14] Ugeda, M. M. *et al.* Characterization of collective ground states in single-layer NbSe2. *Nature Physics* **2015**, *12*, 92–97.

[15] van Loon, E. G.; Rösner, M.; Schönhoff, G.; Katsnelson, M. I.; Wehling, T. O. Competing Coulomb and electron–phonon interactions in NbS 2. *npj Quantum Materials* **2018**, *3*, 32.

[16] Voiry, D. Private Communication, 2018.

[17] Persson, K. Materials Data on LiNbS2 (SG:194) by Materials Project. 2014; An optional note.

[18] Choudhary, K.; Kalish, I.; Beams, R.; Tavazza, F. High-throughput Identification and Characterization of Two-dimensional Materials using Density functional theory. *Scientific Reports* **2017**, *7*.

[19] others,, *et al.* JARVIS: An Integrated Infrastructure for Data-driven Materials Design. *arXiv preprint arXiv:2007.01831* **2020**,

[20] Perdew, J. P.; Kurth, S. *A primer in density functional theory*; Springer, 2003; pp 1–55.

[21] Giustino, F. *Materials modelling using density functional theory: properties and predictions*; Oxford University Press, 2014.

[22] Patterson, J. D.; Bailey, B. C. *Solid-State Physics: introduction to the theory*; Springer International Publishing, 2018.

[23] Groß, A. Theoretical surface science. *A Microscopic Perspective. Originally published in the series: Advanced Texts in Physics,* **2003**, *132*.

[24] Kantorovich, L. *Quantum theory of the solid state: an introduction*; Springer Science & Business Media, 2004; Vol. 136.

[25] Kohn, W.; Vashishta, P. *General Density Functional Theory*.

[26] Hohenberg, P.; Kohn, W. Inhomogeneous Electron Gas. *Phys. Rev.* **1964**, *136*, B864–B871.

[27] Parr, R. G. W. Yang Density functional theory of atoms and molecules. *O xford University Press* **1989**, *1*, 989.

[28] Johnson, D. D. Modified Broyden's method for accelerating convergence in self-consistent calculations. *Physical Review B* **1988**, *38*, 12807.

[29] Broyden, C. G. A class of methods for solving nonlinear simultaneous equations. *Mathematics of computation* **1965**, *19*, 577–593.

[30] Pulay, P. Convergence acceleration of iterative sequences. The case of SCF iteration. *Chemical Physics Letters* **1980**, *73*, 393–398.

[31] Kresse, G.; Furthmüller, J. Efficiency of ab-initio total energy calculations for metals and semiconductors using a plane-wave basis set. *Computational materials science* **1996**, *6*, 15–50.

[32] VASP, Density Mixing. `https://www.vasp.at/wiki/index.php/Category:Density_Mixing`, [Online; accessed 26-September-2020].

[33] Sun, J.; Furness, J. W.; Zhang, Y. *Mathematical physics in theoretical chemistry*; Elsevier, 2018; pp 119–159.

[34] Van Noorden, R.; Maher, B.; Nuzzo, R. The top 100 papers. *Nature News* **2014**, *514*, 550–554.

[35] Sun, J.; Ruzsinszky, A.; Perdew, J. P. Strongly Constrained and Appropriately Normed Semilocal Density Functional. *Phys. Rev. Lett.* **2015**, *115*, 036402.

[36] Perdew, J. P.; Wang, Y. Accurate and simple analytic representation of the electron-gas correlation energy. *Phys. Rev. B* **1992**, *45*, 13244–13249.

[37] Perdew, J. P.; Burke, K.; Ernzerhof, M. Generalized Gradient Approximation Made Simple. *Phys. Rev. Lett.* **1996**, *77*, 3865–3868.

[38] Nazarov, V. U.; Vignale, G. Optics of Semiconductors from Meta-Generalized-Gradient-Approximation-Based Time-Dependent Density-Functional Theory. *Phys. Rev. Lett.* **2011**, *107*, 216402.

[39] Sun, J.; Remsing, R. C.; Zhang, Y.; Sun, Z.; Ruzsinszky, A.; Peng, H.; Yang, Z.; Paul, A.; Waghmare, U.; Wu, X.; Klein, M. L.; Perdew, J. P. Accurate first-principles structures and energies of diversely bonded systems from an efficient density functional. *Nature Chemistry* **2016**, *8*, 831–836.

[40] Zhang, Y.; Kitchaev, D. A.; Yang, J.; Chen, T.; Dacek, S. T.; Sarmiento-Pérez, R. A.; Marques, M. A. L.; Peng, H.; Ceder, G.; Perdew, J. P.; Sun, J. Efficient first-principles prediction of solid stability: Towards chemical accuracy. *npj Computational Materials* **2018**, *4*.

[41] Sabatini, R.; Gorni, T.; de Gironcoli, S. Nonlocal van der Waals density functional made simple and efficient. *Physical Review B* **2013**, *87*.

[42] Peng, H.; Yang, Z.-H.; Perdew, J. P.; Sun, J. Versatile van der Waals Density Functional Based on a Meta-Generalized Gradient Approximation. *Phys. Rev. X* **2016**, *6*, 041005.

[43] Hafner, J. Ab-initio simulations of materials using VASP: Density-functional theory and beyond. *Journal of computational chemistry* **2008**, *29*, 2044–2078.

[44] Krukau, A. V.; Vydrov, O. A.; Izmaylov, A. F.; Scuseria, G. E. Influence of the exchange screening parameter on the performance of screened hybrid functionals. *The Journal of Chemical Physics* **2006**, *125*, 224106.

[45] Moussa, J. E.; Schultz, P. A.; Chelikowsky, J. R. Analysis of the Heyd-Scuseria-Ernzerhof density functional parameter space. *The Journal of chemical physics* **2012**, *136*, 204117.

[46] Ashcroft, N.; Mermin, N. D. *Solid state physics*; Harcourt College Publishers, 1976.

[47] Sholl, D.; Steckel, J. A. *Density functional theory: a practical introduction*; John Wiley & Sons, 2011.

[48] VASP, KPOINTS. `https://www.vasp.at/wiki/index.php/KPOINTS`, [Online; accessed 06-August-2020].

[49] Marsman, M. VASP Workshop at NERSC: Basics: DFT, plane waves, PAW method, electronic minimization, Part 1. `https://www.youtube.com/watch?v=vJkNv095Aj8&t=3s`, [Online; accessed 10-August-2020].

[50] Marsman, M. VASP: Basics. `https://www.vasp.at/wiki/images/5/5d/VASP_lecture_Basics.pdf`, [Online; accessed 10-August-2020].

[51] Wisesa, P.; McGill, K. A.; Mueller, T. Efficient generation of generalized Monkhorst-Pack grids through the use of informatics. *Physical Review B* **2016**, *93*, 155109.

[52] Monkhorst, H. J.; Pack, J. D. Special points for Brillouin-zone integrations. *Physical review B* **1976**, *13*, 5188.

[53] VASP, KPOINTS. `https://www.vasp.at/wiki/index.php/KPOINTS`, [Online; accessed 10-August-2020].

[54] Morgan, W. S.; Christensen, J. E.; Hamilton, P. K.; Jorgensen, J. J.; Campbell, B. J.; Hart, G. L.; Forcade, R. W. Generalized regular k-point grid generation on the fly. *Computational Materials Science* **2020**, *173*, 109340.

[55] Kresse, G.; Hafner, J. Ab initio molecular dynamics for liquid metals. *Physical Review B* **1993**, *47*, 558.

[56] Kresse, G.; Furthmüller, J. Efficiency of ab-initio total energy calculations for metals and semiconductors using a plane-wave basis set. *Computational Materials Science* **1996**, *6*, 15 – 50.

[57] Kresse, G.; Furthmüller, J. Efficient iterative schemes for ab initio total-energy calculations using a plane-wave basis set. *Physical review B* **1996**, *54*, 11169.

[58] Kresse, G.; Joubert, D. From ultrasoft pseudopotentials to the projector augmented-wave method. *Physical review b* **1999**, *59*, 1758.

[59] others,, *et al.* Reproducibility in density functional theory calculations of solids. *Science* **2016**, *351*.

[60] Kresse, G. Pseudopotentials (Part I). `https://www.vasp.at/vasp-workshop/pseudopp1.pdf`, [Online; accessed 09-August-2020].

[61] Blöchl, P. E. Projector augmented-wave method. *Phys. Rev. B* **1994**, *50*, 17953–17979.

[62] VASP, PAW method. `https://www.vasp.at/wiki/index.php/PAW_method`, [Online; accessed 09-August-2020].

[63] Kresse, G. The PAW and US-PP database. `https://www.vasp.at/vasp-workshop/pseudoppdatabase.pdf`, [Online; accessed 09-August-2020].

[64] Jacobs, J. A. *The Earth's core*; Academic Press, 1987.

[65] Birch, F. Finite elastic strain of cubic crystals. *Physical review* **1947**, *71*, 809.

[66] Ramírez-Velásquez, J. M.; Salazar, J. M. SiO2 Electronic Structure in Gas Giants' Planetary Cores: A Density Functional Theory Approach. 2019.

[67] Hosch, W. L. Bulk modulus. `https://www.britannica.com/science/bulk-modulus`, [Online; accessed 17-August-2020].

[68] Tyuterev, V.; Vast, N. Murnaghan's equation of state for the electronic ground state energy. *Computational materials science* **2006**, *38*, 350–353.

[69] Pinto, H. P. Electronic Structure Calculations Using DFT: hands-on with VASP. **2019**,

[70] Voigtländer, B. *Scanning probe microscopy: Atomic force microscopy and scanning tunneling microscopy*; Springer, 2015.

[71] Hofer, W. A.; Foster, A. S.; Shluger, A. L. Theories of scanning probe microscopes at the atomic scale. *Reviews of Modern Physics* **2003**, *75*, 1287.

[72] Neamen, D. A. *Semiconductor physics and devices: basic principles*; New York, NY: McGraw-Hill,, 2012.

[73] Togo, A.; Tanaka, I. First principles phonon calculations in materials science. *Scr. Mater.* **2015**, *108*, 1–5.

[74] Kresse, G.; Furthmüller, J. Efficiency of ab-initio total energy calculations for metals and semiconductors using a plane-wave basis set. *Computational Materials Science* **1996**, *6*, 15 – 50.

[75] Palotás, K.; Hofer, W. A. Multiple scattering in a vacuum barrier obtained from real-space wavefunctions. *Journal of Physics: Condensed Matter* **2005**, *17*, 2705.

[76] Hofer, W. A. A Guide to simulation of STM images and spectra from first principles: bSKAN 3.6. **2005**,

[77] Ganose, A. M.; Jackson, A. J.; Scanlon, D. O. sumo: Command-line tools for plotting and analysis of periodic ab initio calculations. *Journal of Open Source Software* **2018**, *3*, 717.

[78] VASP, INCAR. `https://www.vasp.at/wiki/index.php/INCAR`, [Online; accessed 15-August-2020].

[79] VASP, POSCAR. `https://www.vasp.at/wiki/wiki/index.php/POSCAR`, [Online; accessed 15-August-2020].

[80] VASP, POTCAR. `https://www.vasp.at/wiki/wiki/index.php/POTCAR`, [Online; accessed 16-August-2020].

[81] VASP, METAGGA. `https://www.vasp.at/wiki/index.php/METAGGA#POTCAR_files:_required_information`, [Online; accessed 16-August-2020].

[82] VASP, Input and Output - a short Intro. `https://www.vasp.at/wiki/index.php/Input_and_Output_-_a_short_Intro`, [Online; accessed 16-August-2020].

[83] Ataca, C.; Sahin, H.; Ciraci, S. Stable, single-layer MX2 transition-metal oxides and dichalcogenides in a honeycomb-like structure. *The Journal of Physical Chemistry C* **2012**, *116*, 8983–8999.

[84] Gjerding, M. N.; Pandey, M.; Thygesen, K. S. Band structure engineered layered metals for low-loss plasmonics. *Nature communications* **2017**, *8*, 15133.

[85] Ding, Y.; Wang, Y.; Ni, J.; Shi, L.; Shi, S.; Tang, W. First principles study of structural, vibrational and electronic properties of graphene-like MX2 monolayers. *Physica B: Condensed Matter* **2011**, *406*, 2254–2260.

[86] Liu, Y.; Stradins, P.; Wei, S.-H. Van der Waals metal-semiconductor junction: Weak Fermi level pinning enables effective tuning of Schottky barrier. *Science advances* **2016**, *2*, e1600069.

[87] Novoselov, K.; Mishchenko, A.; Carvalho, A.; Neto, A. C. 2D materials and van der Waals heterostructures. *Science* **2016**, *353*, aac9439.

Abbreviations

AE all electron 30

BO Born-Oppenheimer 5
BZ Brillouin zone 25

DFT density functional theory ix
DOS density of states 47

GGA general gradient approximation ix

HF Hartree-Fock xi, 8, 10
HK Hohenberg-Kohn xi, 11
HSE Heyd-Scuseria-Ernzerhof hybrid functional ix

KS Kohn-Sham 14

PAW Projector Augmented-Wave xi, 30
PDOS partial density of states 47

SCAN strongly constrained and appropriately normed meta-generalized-gradient approximation (meta-GGA) ix
STM scanning tunneling microscopy 2

TMD transition metal dichalcogenides 1

VASP Vienna *ab initio* Simulation Package ix

xc exchange-correlation 15